Universität Hamburg
DER FORSCHUNG | DER LEHRE | DER BILDUNG

Creation of Novel Composites with Distinct Silver Nanoclusters

Dissertation
zur Erlangung des Doktorgrades
an der Fakultät für Mathematik, Informatik und Naturwissenschaften
Fachbereich Physik
der Universität Hamburg

Vorgelegt von

Charline Stahlhut

Hamburg

2023

Gutachter der Dissertation:	1. Prof. Dr. Wolfgang J. Parak 2. Prof. Dr. Alf Mews
Zusammensetzung der Prüfungskommission:	1. Prof. Dr. Dorota Koziej 2. Prof. Dr. Wolfgang J. Parak 3. Prof. Dr. Alf Mews 4. Prof. Dr. Carmen Herrmann 5. Dr. Florian Schulz
Vorsitzende/r der Prüfungskommission:	Prof. Dr. Dorota Koziej
Datum der Disputation:	05.03.2024
Vorsitzender des Fach-Promotionsausschusses Physik:	Prof. Dr. Markus Drescher
Leiter des Fachbereichs Physik:	Prof. Dr. Wolfgang J. Parak
Dekan der Fakultät MIN:	Prof. Dr.-Ing. Norbert Ritter

List of own contributions

Peer-reviewed publications as first author:

1. Joana Rodrigues, **Charline Becker**, Nabiha Ben Sedrine, Marius Kamp, Lorenz Kienle, Rainer Adelung, Yogendra Kumar Mishra, Wolfgang J. Parak, Indranath Chakraborty, Maria Rosário Correia and Teresa Monteiro, "Luminescent silver nanoclusters decorated on ZnO tetrapods: a detailed understanding of their role in photoluminescence features",*Journal of Materials Chemistry C*, 9, 22, 7014-7126, **2021**, DOI: 10.1039/D1TC00099C
2. **Charline Becker**, "Back cover", Artwork design by **Charline Becker**,*Journal of Materials Chemistry C*, 9, 22, 7230-7230, **2021**, DOI: 10.1039/D1TC90122B
3. **Charline Becker**, Sebastian Graf, Alf Mews, Wolfgang J. Parak, Indranath Chakraborty, "Nanohybrids of Silver Nanoclusters Exhibiting FRET", *submitted*

Peer-reviewed publications as co-author:

1. Lin Zhu, Mustafa Gharib, **Charline Becker**, Yuan Zeng, Anna R. Ziefuß, Lizhen Chen, Alaaldin M. Alkilany, Christoph Rehbock, Stephan Barcikowski, Wolfgang J. Parak, and Indranath Chakraborty, SSynthesis of Fluorescent Silver Nanoclusters: Introducing Bottom-Up and Top-Down Approaches to Nanochemistry in a Single Laboratory Class", *Journal of Chemical Education* 97, 1, 239-243, **2020**, DOI: 10.1021/acs.jchemed.9b00342
2. Abdullah Ahmed, Nuria Alegret, Bethany Almeida, Ramón Alvarez-Puebla, Laura Ballerini, **Charline Becker**, Robert H. Blick, Shahin Bonakdar, Indranath Chakraborty, Xiaodong Chen, Jinwoo Cheon, Gerwin Chilla, Andre Luiz Coelho Conceicao, James Delehanty, Martin Dulle, Alex S. T. Efros, Matthias Epple, Mark Fedyk, Neus Feliu, Rafael Fernández Chacón, Niels Fertig, Ste-

phan Förster, Jose A. Garrido, Michael George, Andreas H. Guse, Norbert Hampp, Jann Harberts, Ulrich G. Hofmann, Malte Holzapfel, Yalan Huang, Patrick Huber, Taeghwan Hyeon, Sven Ingebrandt, Marcello Ienca, Armin Iske, Yanan Kang, Gregor Kasieczka, Dae-Hyeong Kim, Kostas Kostarelos, Sijin Liu, Yang Liu, Christian Lohr, John L. Lyons, Volker Mailänder, Laura Maffongelli, Saad Megahed, Alf Mews, Marina Mutas, Leroy Nack, Thomas G. Oertner, Andreas Offenhäuser, Martin Oheim, Ferdinand Otto, Arnd Pralle, Maurizio Prato, Bing Qi, Pedro Ramos Cabrer, Ute Resch Genger, Marten Rittner, Sathi Roy, Francesca Santoro, Florian Schulz, Erkin Şeker, Holger Stephan, Ting Wang, David Wegner, Ming Xu, Yuan Zeng, Yaofeng Zhao, Dingcheng Zhu, Robert Zierold, Wolfgang J. Parak, "Towards interfacing the brain - what nanotechnology may contribute", *in preparation*

Conference contribution:

1. , **Charline Becker**, Indranath Chakraborty, Wolfgang J. Parak, NANAX 9 conference, https://www.chemie.uni-hamburg.de/fachbereich/veranstaltungen/-nanax9/welcome.html ,[**Poster**]
2. "Luminescent Silver Nanoclusters Decorated on ZnO Tetrapods: A Detailed Understanding of Their Role in Photoluminescence Features", Joana Rodrigues, **Charline Becker**, Nabiha Ben Sedrine, Marius Kamp, Lorenz Kienle, Rainer Adelung, Yogendra Kumar Mishra, Wolfgang J. Parak, Indranath Chakraborty, Maria Rosário Correia and Teresa Monteiro, EMRS Fall Meeting 2021, https://www.european-mrs.com/meetings/archives/2021/2021-fall-meeting, [**Oral, online**]

Acknowledgements

Support and contribution are the most important factors that carried me through the duration, struggles and final phase of this work.

My first thank is dedicated to Prof. Dr. Wolfgang J. Parak for having me in his group at the Universität Hamburg (UHH) and his advice and instructive guidance throughout my doctoral research study. I am especially grateful for the support that I could continue my laboratory work during pregnancy and the encouragement in the final phase of finishing doctoral thesis.

I would like to thank Dr. Indranath Chakraborty for his guidance throughout my doctoral thesis. Our discussions and his valuable suggestions were important for the development of my research projects and the improvement of my research skills.

I would also like to thank the mentors and participants of the Graduiertenkolleg Nanohybrid (GRK Nanohybrid), which I was offered to join. Not only was I able to connect with other great researchers and join at events like the conference, the GRK Nanohybrid gave me the possibility to continue my research during pregnancy by employing a student assistant.

This work would not have been possible without our collaborators.
Therefore, I would like to thank Dr. Joana Rodrigues, Prof Dr. Teresa Monteiro and the fellow researchers at the Universidade de Aveiro, who we collaborated with to investigate the photophysical properties under several physical conditions within the Ag NCs@ZnO Tps project. I thank Dr. Marius Kienle and Prof Dr. Rainer Adelung at the Christian-Albrechts-Universität zu Kiel and Prof. Dr. Yogendra K. Mishra at Syddansk Universitet for the support in the electron microscopic investigation of the Ag NCs@ZnO Tps hybrid structure.
In the context of the project 'FRET exhibiting Ag nanocluster hybrid structure', I want to thank Sebastian Graf and Dr. Christian Strelow, Prof. Dr. Alf Mews from the UHH for the support on the systems lifetime characterization and Andrea Köppen from the EM-Service of the Chemistry Department at UHH for the structural and elemental characterization.

A great support have been all group members of the Biophotonik group at UHH who I had the joy to meet throughout the years. Those people were able to fill the time spend in the lab with laughter and create memories, I do not want to miss.

I want to acknowledge the dynaMENT mentoring program for the workshops and thank my mentor Dr. Emmanuelle Quemin for the support during the program and afterwards and my peers for the personal exchange.

Following a great time at the University Hamburg, it has taken me to the Christian-Albrechts-Universität zu Kiel into the group of Prof. Dr. Friedrich Temps. I want to thank him for his support during the writing process of my thesis.

I thank my family and friends for their continuous support throughout the different phases of my doctorate.
I would like to express my special gratitude to my husband for his unconditional love and the courage to become parents during my doctorate.

Abstract

Nanoclusters are ultra-small and stand out through their atomic precision. They are made from a defined number of metal core atoms, which are protected by a certain number of ligands. The molecule-like properties give them a HOMO-LUMO energy-level structure and unique photoluminescence properties. Already minimal changes like an additional atom can drastically change the nanoclusters photoluminescence properties to the point of full vanish or degradation of the nanoclusters. As a result, a high sensitivity can be derived and nanoclusters can be imagined in a diverse range of sensing, anti-microbial and photocatalysis applications.

To understand how nanoclusters react to the presence of another species or changes of the environment, $Ag_{29}DHLA_{12}$ nanoclusters (Ag NCs) developed by Adhikari et al. were used as the research system due to the reliable reproducibility and long-term stability. [1] The first hybrid structure Si-Ag_{29} NCs was created by covalently connecting Si-based nanoclusters (Si NCs) to Ag NCs without additional length. These Si NCs were developed based on the syntheses from Ma et al. and Dou et al. with a size of ~ 2 nm. [2,3] The second hybrid structure AgNC@ZnO Tps is composed of Ag NCs fixed on zinc oxide tetrapods, which function as a micrometer-sized scaffold. This allows to separate the Ag NCs from the aqueous synthesis environment.

The optical and structural properties of the hybrid structures have been investigated via optical spectroscopy and microscopic methods. Photoluminescence analysis allows to follow the change of the signature emission unique to Ag NCs. At low temperatures, the optical centers have been deconvoluted and the interaction of the respective components and the resulting electronic structures were characterized. Structural composition was investigated through electron microscopy and optical laser scanning microscopy allowed to investigate the luminescence on the tetrapodal structures.

The Si-Ag_{29} NCs hybrid structure forms a FRET system, where the Si NCs act as donors and Ag_{29} NCs as acceptors. The energy transfer has an maximum efficiency of 63 %, which is comparable to other FRET systems of nanoclusters combined with organic dyes or quantum dots. Optical characterization shows an acceleration of the internal recombination processes in Ag NCs. This behaviour could be initiated in the same way in an analogue system with the organic dye Hoechst Blue as donor.
For the AgNC@ZnO Tps hybrid structure, three emitting optical centers have been

deconvoluted, which result in a green and near-band edge region emission at room temperature. The presence of Ag NCs enhances the emission from ZnO surface states and the nanoclusters emission shifts to lower energies, when excited with energy below the ZnO bandgap. With an energy above the ZnO bandgap the nanoclusters emission vanishes and ZnO recombination dominates the resulting spectra. Overtime a gradual loss of the emission was observed and could be a connecting factor for future research.

This work reviews the response of Ag nanoclusters to external factors or the change of the environment and the changes in the optical recombination structures.

Zusammenfassung

Nanocluster sind ultra-klein und stechen auf Grund ihrer atomaren Genauigkeit heraus. Diese bestehen aus einer definierten Anzahlen von metallischen Atomen im Kern, die von einer definierten Anzahl an Liganden stabilisiert werden. Die molekühl-artigen Eigenschaften erzeugen eine HOMO-LUMO Energielevelstruktur und einzigartige Photolumineszenz-Eigenschaften. Schon minimale Veränderung wie ein zusätzliches Atom im Kern kann einschneidende Veränderungen der Photolumineszenz-Eigenschaften bis zur vollständigen Auslöschung oder die Zersetzung der NCs hervorrufen.

Als Ergebnis kann daraus eine hohe Sensitivität abgeleitet werden und die Nanocluster können in vielfältigen Bereichen wie sensorischen, anti-microbiellen und photokatalytischen Anwendung einen Nutzen bringen. Um zu verstehen, wie Nanocluster auf die Anwesenheit anderer Partikel oder eine Veränderung der Umgebung reagiere, wurden $Ag_{29}DHLA_{12}$ Nanocluster (Ag NCs), die von Adhikari et al. entwickelt wurden, als Forschungsgegenstand gewählt, da sie eine verlässliche Reproduzierbarkeit und eine Langzeitstabilität aufweisen. [1] Die erste Hybridstruktur Si-Ag_{29} NCs wurde erzeugt durch die kovalente Verbindung von Si-basierten Nanoclustern (Si NCs) mit Ag NCs ohne zusätzlichen Abstand. Die Si NCs wurden auf Basis der Synthesen von Ma et al. und Dou et al. mit einer Größe von 2 nm entwickelt. [2, 3] Die zweite Hybridstruktur AgNC@ZnO Tps besteht aus Ag NCs fixiert auf Zinkoxid Tetrapods, die als mikrometer-großes Gerüst fungieren. So können die Ag NCs von der wässrigen Syntheseumgebung getrennt werden.

Die optischen und strukturellen Eigenschaften der Hybridstrukturen wurden durch optische Spektroskopie und mikroskopischen Methoden untersucht. Photolumineszenzanalyse wurde genutzt, um Veränderungen der für Ag NCs charakteristischen Emission zu verfolgen. Bei tiefen Temperaturen wurden die optischen Zentren aufgeschlüsselt und die Wechselwirkung der Komponenten miteinander und die resultierenden elektronischen Strukturen charakterisiert. Die strukturelle Zusammensetzung wurde durch Elektronmikroskopie bestimmt und mittels optische Laser-scanning Mikroskopie wurde die Lumineszenz auf den Tetrapodstrukturen untersucht.

Die Si-Ag_{29} NCs Hybridstruktur bildet ein FRET System, indem die Si NCs als Donor und die Ag NCs als Akzeptor fungieren. Der Energietransfer hat eine maximale Effizienz von 63 %, die der Effizienz von anderen FRET-Systemen vergleichbar ist,

die aus Nanoclustern und organischen Farbmolekülen oder Quantum Dots aufgebaut sind. Die optische Charakterisierung zeigt eine Beschleunigung der internen Rekombinationsprozesse der Ag NCs. Dieses Verhalten konnte in gleichem Maße mit einem analogen System initiiert werden, indem das organische Farbmolekül Hoechst Blue als Donor gewählt wurde.
Für die AgNC@ZnO Tps Hybridstruktur wurden drei emittierende optische Zentren aufgelöst, die bei Raumtemperatur eine grüne und eine Near-Band-Edge Emission erzeugen. Die Anwesenheit von Ag NCs verstärken die Emission der ZnO Oberflächenzuständen und die Emission der Nanocluster verschiebt sich zu geringeren Energien, wenn das System mit einer Energie unterhalb der ZnO Bandlücke angeregt wurde. Bei Energien oberhalb der ZnO Bandlücke verschwindet die Emission der Nanocluster und die Rekombinationen im ZnO dominieren das finale Spektrum. Der beobachtete, graduelle Abfall der Emission mit der Zeit gibt einen Anknüpfungspunkt für eine anschließenden Forschung.

Diese Arbeit untersucht die Reaktion von Ag Nanocluster auf externe oder die Veränderung der Umgebung und die Veränderungen der optischen, rekombinatorischen Strukturen.

Contents

List of Abbreviations

$AgNO_3$	silver nitrate
Na_2BH_4	sodium borohydride
PPh_3	triphenylphosphine
AIE	aggregation induced emission
AIE	aggregation-induced emission
AIEE	aggregation induced emission enhancement
APTES	3-aminopropyl-triethoxysilane
BDT	1,3-benzene-dithiol
BSA	bovine serum albumin
Cascade Blue	[(3,6,8-trisulfo-1-pyrenyl)oxy]-,1-hydrazide trisodium salt
CLSM	confocal laser scanning microscopy
DHLA	dihydrolipoic acid
EDC	N-(3-dimethylaminopropyl)-N'-ethylcarbodiimide hydrochloride
EDTA	Ethylenediaminetetraacetic acid disodium salt dihydrate
EDX	energy dispersive x-ray
ESI MS	electrospray ionization mass spectrometry
FFT	fast Fourier transformation
FWHM	full width at half maximum

GL	green luminescence
GSH	glutathion
Hoechst 33342	2'-(4-Ethoxyphenyl)-5-(4-methyl-1-piperazinyl)-2,5'-bi-1H-benzimidazol trihydrochlorid
HRTEM	high-resolution transmission electron microscopy
LA	lipoic acid
LO	longitudinal optical
NBE	near band edge
NCs	nanoclusters
NHS	N-hydroxysuccinimide
PL	photoluminescence
PLE	photoluminescence excitation
PVB	polyvinyl butyral
RT	room temperature
SG	glutathion
TPP	triphenylphosphine
TPs	tetrapods
TRIS	Tris(hydroxymethyl)aminomethane
UV	ultraviolet
UV-Vis	UV-visible
XRD	x-ray diffraction
ZnO	zinc oxide

List of Figures

List of Tables

1 Introduction

1.1 Metal Nanocluster

In the recent years the research on atomically precise nanoclusters has gained visibility and attention. The development started with the idea of nanoclusters building a bridge between nanoparticles and molecules, allowing to expand the knowledge on chemical and physical properties. Methods like single crystal x-ray diffraction (XRD) and electrospray ionization mass spectrometry (ESI MS) have allowed to determine the compositions of the synthesized nanoclusters. A general structure of nanoclusters consists of an inner core/kernel surrounded by stabilizing ligands, which form an additional semi-ring at the interface influencing the properties. [5] Due to the very small size of nanoclusters, minimal changes on these three structural features change the properties up to full optical property extinction. The recent years brought great development on the understanding of the properties and the mechanisms.
The first factor to understanding the properties are the routes to synthesise nanoclusters. Being a smaller version of nanoparticles, the widely used Brust-Method has been adapted to synthesize thiol protected nanoclusters. During the process Au(III) precursor and thiol ligand forms an Au(I)-SR complex followed by a reduction to form the clusters. [6] Thiol ligands evolved to be the key factor to the formation of nanoclusters due to their strong attraction to the noble metals gold and silver. [7, 8]
The following methods use presynthesized nanoparticles or nanocluster, which are treated with an excess of ligands. Processes of size focusing, ligand exchange, chemical etching often lead to monodisperse nanoclusters. Introducing foreign metals via complexes or salts during the nanocluster formation process leads to doping with few foreign metal atoms up to alloy formation.
The investigated $Ag_{29}(DHLA)_{12}$ nanocluster are synthesized through a combination of a bottom-up and top-down process. [9] As the bottom-up segment, upon the reduction of the precursor $AgNO_3$ Ag nanoparticles with plasmonic properties form and grow to a size of a few hundred atoms. These large entities are etched into

the stable NCs by an excess of dithiolate ligands in the presence of oxygen as a top-down process. Size focusing towards a core with 29 Ag and 12 DHLA occurs via intermediates like $Ag_{28}(LA)_{11}^{2-}$, $Ag_{26}(LA)_{10}^{2-}$ and $Ag_{29}(LA)_{11}^{2-}$. [10] In the final synthesis solution, these intermediates have no longer been identified and transformed from polydisperse nanoparticles to a monodisperse nanocluster solution. [11]
The number of found stable silver nanoclusters has risen in the last years. One of the earliest and now determined in its crystal structure are the $Ag_{44}(SR)_{30}^{4-}$ NCs and $Ag_{25}(SR)_{18}^{-}$ NCs. [12–15] Found stable entities vary in core numbers from 21 up to 88 Ag atoms. [12] The main groups of molecules used as ligands are thiols, phosphates/phosphines or biological molecules functioning as templates. The following ligands are common examples of those groups: 1,3-benzene-dithiol (BDT), triphenylphosphine (TPP/PPh_3), dihydrolipoic acid (DHLA), DNA or bovine serum albumin (BSA). [5, 7, 10, 12, 16, 17] Besides the preferred metals silver and gold, stable nanoclusters have been developed from the elements like copper, platinum or palladium. [18–22] Another promising class of nanoclusters are the alloy nanocluster. This category spans from mono-metallic nanoclusters doped with single atoms to co-reduction of precursors of different metals. Due to the high sensitivity to structural and environmental factors, single atom doping allows to manipulate the nanoclusters properties. This results in enhancement of e.g. physicochemical performance, thermal stability or catalytical activity. [5, 23] Single atom doping can be achieved by combining presynthesized homo-metal nanoclusters with metal salts or complexes. [23] The templates often come with 'magic size' and maintain their molecular structure and closed shell configuration upon doping. For alloy nanoclusters with several heteroatoms, ligated metal complexes can be co-reduced and calculations are a useful tool to predict the most probable, stable nanoclusters and propose their properties. Calculations can also predict the structural composition. For many single atom doped nanoclusters with main metal Au, Ag or Cu, the foreign metal atom is located inside a cage of 13 atoms which is the surrounded by stabilizing ligands. In greater sized nanoclusters and upon incorporation of multiple hetero-atoms of different elements, the nanoclusters are build in shells, reaching enhanced stability, when these shells are closed. The foreign atoms are often located in the center, a possible 2nd shell and especially the vertex/semi-ring according to calculations. The vertex/semi-ring is a shell formed between metal entities and the ligand binding side,which is often a thiol group. These structural features allow to explain the origin of the fluorescence and other properties of the nanoclusters, which is discussed in the following section.

1.2 Fluorescence metal nanocluster

Fluorescence is one of the most prominent properties of nanoclusters, because it is often emitted in the visible range of the spectrum. Nevertheless, nanoclusters are known that emit in NIR, invisible for the human eye. [5] Key to understand the origin of the fluorescence of nanoclusters are their inner structure and connection between the core and the stabilizing ligands. As described in the previous section, the core, shell, vertex/semi-ring have been identified as the main structural units. Ligand exchange being one of the first and easiest to test the influence of modifications. Here, it has been found that the fluorescence originates from ligand to metal cluster core charge transfer (LMCCCT) through a Au/Ag – S bond in the vertex/semi-ring. Depending on the ligand nature, the electron donation ability of the ligand binding-group to the metal core supports the charge transfer. [5, 24–27]

Computational explorations are a preferred tool to explain experimental findings. Gold doping of $[Ag_{29}(BDT)_{12}(TPP)_4]^{3-}$ has been calculated to induce an enhancement of the fluorescence intensity by relativistic effects for greater numbers of induced Au atoms (x=3-5). Additionally the formation of heteronuclear bonds between Au and Ag can increase the stability of the nanocluster and modify the fluorescence intensity. [28] A similar effect was found in $[Ag_XAu_{25-X}(PPh_3)_{10}(SC_2H_4Ph)_5CL_2]^{2+}$ nanoclusters. Doping with upto 12 Ag atoms could raise the quantum yield from 0.1 % to 0.21 %. With a 13th Ag atoms added to the nanocluster, the emission became strong and red with a QY=40.1 %. Here, computational methods and crystal structure analysis allow to predict the positions of the Ag atoms and which orbitals are of importance to the strong increase of the QY. [27, 29, 30] From these learning's, ideas can be drawn to design syntheses routes to find new promising, stable nanoclusters.

Ligand engineering as the surface modification of nanocluster can enhance the photoluminescence as well as the stability of nanoclusters. The interaction with the core via electron donation is variable trough different functional groups like carbonates, phosphates or thiols. The ligands backbone structure brings different degrees of rigidity, which strongly influences the formation of the HOMO-LUMO configuration and therefore the nanoclusters properties. The rotational freedom of the ligands is furthermore influence by the surrounding media. A solvent change from dichloromethane to acetonitril could increase the QY of $Pt_1Ag_{24}(SR)_{18}$ from 0.2 % to 18.6 %. [31, 32]

A change of the solvent polarity can initiate the effects of aggregation induced emission (AIE) and aggregation induced emission enhancement (AIEE). The effect of

AIEE describes the development of PL in non-luminescent nanoclusters and AIE the enhancement of PL intensity. An example is the graduate addition of ethanol into water, where the change of the luminescence is influenced by the degree of added ethanol. These effect are possible because the stability of nanoclusters often depends on a constant ligand exchange with the excess ligand in the solution. A restriction of this exchange and change of the possible movement within the ligand structure impacts the formed energy band structure. [18, 31, 33]

The etching process has been found to influence the dispersity as well as the fluorescence colour. Cu nanoclusters have been created from nonluminescent, plasmonic copper nanoparticles by etching with glutathion (SG/GSH) at room temperature and 70 °C. While at room temperature $Cu_{34–32}(SG)_{16–13}$ nanoclusters with red emission emission form, at 70 °C monodisperse $Cu_{25}(SG)_{20}$ with blue emission develop. [18] Depending on the environmental temperature, nanocluster do not behave in a uniform way. Rise in temperature can either increase the intensity without a peak shift or decrease upon the increasing overlap of peaks, which decreases the intensity and broadens the emission feature. [27, 32]

2 Aim of work

Nanoclusters attract attention due to their optical and physicochemical properties formed by their unique, molecule-like structure. The size below 5 nm leads to a HOMO-LUMO energy level formation and this energy transition results in unique, strong photoluminescence. The choice falls onto silver as the core metal, as it is of stronger reactivity and oxidizable for zero-valent state silver.
$Ag_{29}DHLA_{12}$ nanoclusters are very stable, well characterized and can be synthesized with a reliable result.

The synthesis of $Ag_{29}DHLA_{12}$ nanocluster is performed in an aqueous solution and therefore the nanoclusters are naturally evenly distributed within. The constant diffusion of the particle in the medium restricts the investigation to the collective of particles in their environment. To gain inside to the individual properties and locate the origin of property changes, single nanoclusters need to be addressed.
One way to address individual nanoclusters is the direct linkage of a foreign moiety to the stabilizing ligands of the $Ag_{29}DHLA_{12}$ nanoclusters. In this work size-defined silicon-based nanoclusters have been chosen to be paired via zero-distance, direct coupling. The advantage of the zero-distance coupling are absent interfering moieties and a direct interaction between the nanoclusters is enforced. Although the surrounding environment is changed as minimal as possible to keep the global properties nearly same.
On the contrary, the nanoclusters are separated from the aqueous environment and deposited on a macroscopic scaffold. This reduces the movement of the nanoclusters and fixed in space a detailed investigation of property changes at distinct locations. Therefore, no exchange of clusters can occur like in solution. This narrows the influence occurring to the $Ag_{29}DHLA_{12}$ nanoclusters among each other and the scaffold. ZnO as a material is widely studied and a severe knowledge has gained for the micron sized tetrapods.
This work reaches to build knowledge on the behaviour of $Ag_{29}DHLA_{12}$ nanoclusters in direct interaction with foreign moieties and changes of the environmental factors.

3 Experimental section

3.1 Materials

All chemical components were commercially available and used without further purification.
Lipoic acid (LA), sodium borohydride (Na_2BH_4), silver nitrate ($AgNO_3$), Zinc oxide (ZnO) metal powder and polyvinyl butyral (PVB), glycerol, orange G, N-hydroxysuccinimide (NHS), sodium L-ascorbate, N-(3-dimethylaminopropyl)-N'-ethylcarbodiimide hydrochloride (EDC), Ethylenediaminetetraacetic acid disodium salt dihydrate (EDTA) were purchased from Sigma-Aldrich. 3-aminopropyl-triethoxy-silane (APTES) was purchased from Fluka. Cascade Blue ([(3,6,8-trisulfo-1-pyrenyl)-oxy]-,1-hydrazide trisodium salt) and Tris-(hydroxymethyl)-aminomethane (TRIS) were purchased from Invitrogen – Thermo Fischer Scientific. Boric acid was purchased from Roth. Agarose and Hoechst 33342 [2'-(4-Ethoxyphenyl)-5-(4-methyl-1-piperazinyl)-2,5'-bi-1H-benzimidazol trihydrochlorid] were provided within the chemical stock of the research group.

3.2 Material syntheses

3.2.1 Synthesis of $Ag_{29}(DHLA)_{12}$ nanoclusters

19 mg lipoic acid (92 µmol) and 7 mg $NaBH_4$ (0.019 mmol) were combined in 14 mL Milli-Q® water and constantly stirred until the full dissolving of LA. Afterwards the addition of 700 µL 25 mM $AgNO_3$ (17.5 µmol) led to a change of the solutions appearance from clear to a turbid bright yellow. The nanocluster formation is initiated by 10 mg $NaBH_4$ (0.26 mmol), which was freshly prepared. During 3-5h of constant stirring and under the exclusion of light the nanoclusters form. The final samples solutions were stored at 4 °C and protected from light.

3.2.2 Synthesis of silicon based nanoclusters

Silicon nanoclusters (Si NCs) were synthesized by adding 2 mL APTES into constantly stirred 4 mL Milli-Q® water. Prior to the addition, the water was warmed to 40 °C with the help of a water bath. 10 minutes after the addition of APTES 625 µL 0.1 M sodium L-ascorbate was added to initiate the nanocluster formation. Stirring was continued for 20 min and afterwards the final sample solution was stored at 4 °C.

3.2.3 Creation of Si-Ag_{29} NCs hybrid structure

The Si-Ag_{29} hybrid structure was formed by coupling the two nanocluster species in aqueous solution by EDC-NHS coupling. Therefore the individual solutions were combined at volume ratios from 1:0.25 to 1:2 ($V_{Si\ NCs}$:$V_{Ag_{29}}$). To maintain the same total volume for all samples Milli-Q® water was added. For the coupling process, 64 µL EDC (15 mM) and 32 µL NHS (30 mM) were added during constant stirring at 450 rpm for 24 hours at room temperature.

3.2.4 Synthesis of ZnO tetrapods

The synthesis of the ZnO tetrapods (TPs) was performed by collaborators from the Christian-Albrechts-Universität zu Kiel following the detailed descriptions of Y.K. Mishra, R. Adelung and co-workers. [4, 34–37]
The synthesis of the ZnO TPs was performed via flame transport synthesis. The Zn precursor material was composed of ZnO metal powder with a grain size of 5 µm and polyvinyl butyral powder (PVB) mixed at a weight ratio of 1:2. This material composition was then filled into a ceramic crucible, attached into a muffle furnace and heated to 900 °C for 30 minutes. The high temperature initiated a conversion of the Zn metal powder into atomic vapor. Native oxygen led to the growth of the tetrapodal structures inside the furnace. The controlled aspect ratio between ZnO precusor material and oxygen led to the development of one-dimensional arms of the tetrapods at nanometer scale. After a cool down duration of 30 minutes the tetrapod powder was harvested as a cotton-like, fluffy powder, ready to be further processed into Ag_{29}@ZnO tetrapod hybrid material.

3.2.5 Creation of Ag_{29}@ZnO tetrapod hybrid material

The hybrid material Ag_{29}@ZnO tetrapods was created by combining ZnO Tps in 500 µL concentrated Ag_{29} NCs solution for 5 hours under constant shaking. The concentration of the original Ag_{29} NCs solution was achieved as follows: 4 mL Ag_{29} NCs solution was pipetted into the filter section of a 3 kDa centrifugal filter and centrifuged repetitively for periods of 2:30 min at 9000 rpm until the total volume was reduced to 500 µL. In between the periods the solution were resolubilized to avoid Ag_{29} NCs precipitating on the filter walls through the radial forces during centrifugation.

3.3 Experimental Procedures

3.3.1 Hydrodynamic size and zeta-potential characterization

The determination of the hydrodynamic size and the ζ-potential were performed on a Malvern Zetasizer Nano-ZS and operated at 633 nm and 4 mW. All measurements were performed in milli-Q water.

3.3.2 Particle concentration

The centrifugation filtration was performed on a Hettich Universal 320R centrifuge with Amicon Ultra-4 3 kDA cut-off centrifugal filters with a PLBC Ultracel-PL membrane from Millipore.

3.3.3 Absorbance characterization

UV-Visible (UV-vis) absorbance characterization was performed on an Agilent 8453 UV-vis spectrometer at room temperature. A deuterium (UV) and a tungsten lamp (vis) allowed to examine samples between 200 nm and 900 nm in a 10 mm path length quartz cuvette.

3.3.4 Photoluminescence characterization

Images of UV irradiated samples were collected in a BioDocAnalyze Biometra from Whatmann.
Photoluminescence (PL) characterization was performed on a Horiba Fluorolog FL3-22 spectrofluometer with a Xenon 450 W light source covering an excitation range 240-600 nm. The radiation was collected under a 90° angle by an build-in R928P detector.
Excitation spectra were collected for an emission wavelength at 500 nm in the range of 260-480 nm and emission spectra were recorded at an excitation wavelength of 390 nm over the range 410-760 nm.
2D PL characterizations were performed with an excitation within the range of 300-520 nm at an increment of 10 nm and the emission was collected within 370-760 nm with an increment of 2 nm.

3.3.5 Lifetime characterization

Lifetime characterization was performed on a Fluotime 300 from PicoQuant with a supercontinuum lasers SuperK Fianium and Super K Compact with the spectral extension unit SuperK EXTEND-UB from NKT Photonics as a light source. The system was operated via the EasyTau2 software and the NKT Photonics CONTROL Software. The excitation wavelength was selected through the monochormator LLFT Contrast by NKT Photonics and operated at a 2.7 nm bandwith by the software PhySpec from Photon etc. . The system is completed by a PMA Hybrid 07 detector from PicoQuant with a time resolution of 50 ps.

3.3.6 Gel electrophoresis

Gel electrophoresis was performed in 0.5x (TBE) buffer on an agarose gel for 30 min at 110 mV and at RT. The Tris-Borate-EDTA (TBE) buffer was prepared from Tris(hydroxymethyl)aminomethane, boric acid, and Ethylenediaminetetraacetic acid disodium salt dihydrate (EDTA). As marker orange G was combined with glycerol at a 1:8 ratio and mixed with the respective sample in a rate of 1:5 prior electrophoresis.

3.3.7 Confocal laser scanning microscopy

Confocal laser scanning microscopy was performed on a Zeiss LSM 510 Meta. Within a diode generated excitation light at 405 nm, which passes a primary dichroic beam splitter 405/488, secondary dichroic beam splitter 545 and a long pass filter 615.

3.3.8 Transmission electron microscopy

The structure of the Si-Ag_{29} hybrid material was investigated through high-resolution transmission electron microscopy (HRTEM) on a JOEL JEM 2200 FS at 200 kV. Samples were casted on carbon film-coated 400-mesh copper grids. For elemental analysis an Oxford Silicon-Drift-Detector Modell X-Max 100 was used. Beforehand samples with added additional volume of 3x initial volume were purified through centrifugal filtration with an Amicon Ultra-4 centrifugal filter (Ultracel-3 regenerated cellulose membrane, 3 kDa) from Millipore.

Ag_{29}@ZnO tetrapod samples were casted on copper TEM grids from Plano GmbH covered with a lacy carbon film and investigated on a Tecnai F30 STwin G^2 with 300 kV acceleration voltage. In high-angle annular dark-field (HAADF)-STEM mode the atomic-number-dependent Z-contrast of the samples were investigated. Energy dispersive x-ray (EDX) characterization was performed with a Si/Li detector (EDX System).

4 FRET exhibiting Ag nanocluster hybrid structure

4.1 Aim of work

The Förster resonance energy transfer (FRET) is an intensively studied energy transfer, who's origin is the photosynthesis study of Theodor Förster. [38] He found that the absorbed number of photons exceeds the reaction centers of the exposed area. From this find developed a research investigating the energy transfer between two chromophores in close proximity. This effect is strongly driven by the distance between the chromophores, turning it into a sensitive, specific fluorescence based tool to measure across distances of several nanometers. Within macromolecules like proteins, nucleic acids and lipids, the efficiency of the FRET allows to follow conformational changes or determine positions of specific sides.
The interaction between the chromophores can be sketched as follows:

$$\mathrm{D}^* + \mathrm{A} \longrightarrow \mathrm{D} + \mathrm{A}^*$$

One chromophore, the donor, becomes excited and upon internal conversion and vibrational relaxations the energy transfer excites the second chromophore. The so called acceptor experiences internal as well and the final relaxation results in a visible emission. In contrast, the donor relaxes to the ground state in a non-radiative process.
The rates of these processes allow to determine the efficiency of the process E, which is the quantum yield of the energy transfer process.

$$E = \frac{k_{ET}}{k_f + k_{ET} + \sum k_i} \tag{4.1}$$

k_{ET} is the rate of the FRET, k_f is the rate of the radiative processes and the non-radiative relaxations are described by k_i. As FRET is a dipole-dipole interaction,

calculation of the distance r between the chromophores is based on the distance R_0 of 50% transfer efficiency. The distances are included in the efficiency equation with a power of six, showing the strong dependency and sensitivity of the FRET process on the distance.

$$E = \frac{1}{1 + \left(\frac{r}{R_0}\right)^6} \tag{4.2}$$

From the sensitivity to the distance between the chromophoric pair derived a great range of research opportunities, which are exemplified in the following:
Ekaterina Sobakinskaya et al combined quantum chemical, electrostatic and molecular dynamics calculations to simulate the FRET process as a ruler to determine distance within a polyprolin helices labeled with Alexa Flour 488 and Alexa Flour 594. [39] The calculated distances quantitatively matches the data of the experimental study done by Benjamin Schuler et al. [40] Organic dyes like Rhodamin derivates, Hoechst 33342 or Alexa488 are often utilized to be bound to proteins or DNA. In combination with nanoclusters or quantum dots, the FRET process allows to follow conformational changes upon exposure with ions like Ag^+ [41, 42] or Hg^+. [43] Gold (Au) and silver (Ag) nanoclusters are a favored chormophore in sensing studies. Au NCs capped with BSA and L-proline have been matched with a WS_2 nanosheet to form a dual-colour sensor for aptamers. [44] Koushik Mondal et al have created a hybrid material from solvent-stabilized (N,N-dimethylformamide) Au NCs and nitrogen-doped graphene quantum dots to generate white light emission. [45] A different support has been a liposomal membrane with incorporated BSA-capped Ag NCs, which interact via FRET with a coumarin dye (C6) upon external stimuli like temperature or UV radiation. [46]
Often research focuses on the application of the FRET pair with one chromophore being a nanocluster. The creation of a connected two-nanocluster system from silicon nanoclusters, a size defined nanocluster, and Ag_{29} NCs, a molecular nanocluster, aimed to gain inside to the internal processes of nanoclusters. Their unique photophysical properties and the high photostability are an advantage for the study of FRET process by the optical characteristics and the changes in the photoluminescence behaviour.

4.2 Results and Discussion[1]

To create a hybrid system from two nanoclusters, a silicon nanocluster synthesis was developed based on the syntheses from Ma et al. and Dou et al.. [2, 3] The synthesis solution appears in a clear, peachy colour and a blue, green fluorescence under UV light (fig. 4.1Aii). The determined hydrodynamic radius of the Si NCs is approximately 2 nm (fig. 7.1C). The absorbance spectrum of the Si NCs shows a shoulder from 300-450 nm and a small step around 550 nm. Excitation at 390 nm results in an emission with a maximum at 500 nm and the excitation spectrum peaks at 410 nm for the emission wavelength of 500 nm. Ag_{29} NCs were synthesized according to the description of Marte van der Linden and coworkers. [48] The synthesis solution appears in an orange colour and has a strong red fluorescence (fig. 4.1Bii). The absorbance spectrum of the Ag_{29} NCs shows three distinct peaks at 330 nm, 430 nm and 500 nm, which is a sign of the molecular structure of the NCs and which are matching the synthesis reference (fig. 7.3). The emission of the Ag_{29} NCs peaks at 660 nm with a second peak at 650 nm. The according excitation spectrum for the emission maximum shows a broad spectrum with three peaks at the same wavelengths as found as peaks in the absorbance spectrum(fig.4.1).
The incorporation of nanoclusters in a hybrid system is usually performed by chemically bonding the nanocluster via its ligands to the second moiety. The chemically linkage is usually of very short distance, which allows herein discussed hybrid system to assume a transfer process between the two nanoclusters. For a transfer process like the Förster resonance energy transfer (FRET) an overlap of the emission of a donor species with the excitation spectrum of an acceptor species. The spectra in figure 4.1C show the overlap of the excitation spectrum of the Ag_{29} NCs and the emission of the Si NCs. By this overlap a Stokes shift of the photoluminescence maximum from 490 nm to 660 nm is possible after excitation with an wavelength exciting Si NCs. An additional 2D PL characterization (fig. 7.2) shows the PL peaks of the two nanoclusters are clearly separated. This separation shows promise that PL is a good indicator for interaction between the nanoclusters.

[1]The data of this work has been submitted. [47]

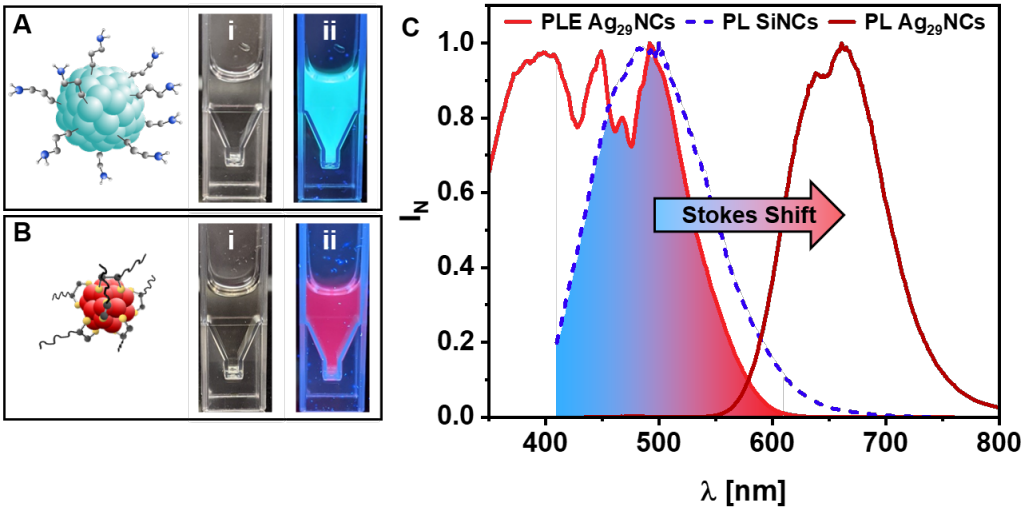

Figure 4.1: Schematic of SiNCs (A) and Ag29 NCs (B) and pictures of the synthesis solutions under white light (i) and UV light (ii). Photoluminescence emission spectra of SiNCs (blue, dashed) and Ag29 NCs (dark red, solid) and the excitation spectrum of Ag29 NCs (red, solid) with indicated overlap (filled area) of Ag29 NCs excitation and SiNCs emission spectra with indicated Stokes shift of emission maxima (C). In manuscript.

In a hybrid system Si NCs can be assigned to the role of the donor species and Ag_{29} NCs to the role of the acceptor species. A transfer process like FRET calls for a specific spacing between the donor and the acceptor, which determines the transfer rate and therefore the success of the stokes shift. The nanoclusters are connected via EDC coupling, which is a zero-length-linkage. As a result the distance between the interacting particles is determined by the stabilising ligands of the NCs, because no additional molecular section is integrated. Si NCs are surrounded by aminopropyl and Ag_{29} NCs is stabilized by lipoic acid. These stabilizing agents result in a zeta potential of 0 mV for the Si NCs, thus the amine group is protonated (7.1). Lipoic acid stabilizes the silver core through the thiol group and the carboxylic group aligned outwards results in a negative zeta potential. The opposite charge attracts the nanoclusters towards each other and can form a charge-attracted hybrid system between the nanoclusters (Si+Ag_{29} NCs). This allows to study the interaction between the nanoclusters on basis of the charge attraction to compare it with the chemically-bound system.

The EDC coupled hybrid system Si-Ag_{29} NCs characterized by absorbance and photoluminescence characterization shows a combination of the single features of the nanocluster species. The absorbance spectrum of the hybrid system shows the three

characteristic peaks of Ag_{29} NCs at similar positions. The progress at low wavelengths is lifted in absorbance value, which can be ascribed to the shoulder in the Si NCs absorbance spectrum. Figure 7.3 also shows the spectrum of the charge-attracted Si+Ag_{29} NCs system and it shows a similar progress as the covalent-bound Si-Ag_{29} NCs of lower absorbance value. This reduced values can be attributed to the greater distance and therefore weaker interaction between the nanoclusters. A Jacobian correction of the absorbance spectra of Si NCs, Ag_{29} NCs and Si-Ag_{29} NCs in figure 4.2B depicts the resulting spectrum for the hybrid system as a direct combination of the spectra from the single nanocluster species. The peaks of Ag_{29} NCs are positioned at 2.48 eV, 2.89 eV, and 3.72 eV and appear lifted by the absorbance value of the Si NCs. The PL of the Si-Ag_{29} NCs in a 2D map shows a clear appearance of the maxima of the single nanocluster species clearly separated (fig. 4.2C). A comparison of the 2D-Pl spectra of Si NCs and Ag_{29} NCs (fig. 7.2) with the one of the Si-Ag_{29} NCs displays an reduction of the Si NCs PL intensity especially between $\lambda_{ex} = 300 - 350\ nm$. This reduction indicates the key part of the FRET process as energy is transferred to the Ag_{29} NCs, which should result in an enhanced PL intensity of the acceptor at $\lambda_{ex} = 300 - 350\ nm$.

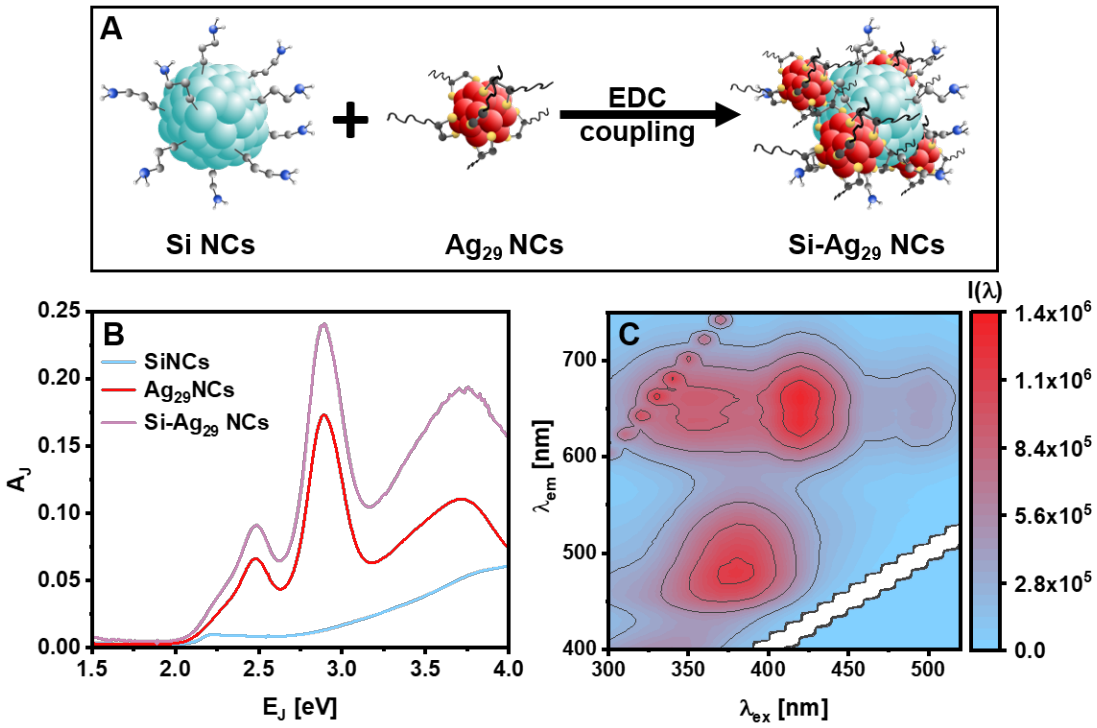

Figure 4.2: Hybrid nanocluster system Si-Ag_{29} NCs formation via EDC coupling as schematic (A). Absorbance of Si NCs, Ag_{29} NCs, and Si-Ag_{29} (B) and 2D photoluminescence spectra of Si-Ag_{29} NCs (C). In manuscript.

With this experiments the first evidence for a FRET process within an EDC-coupled Si-Ag_{29} NCs hybrid system was found. Further inside about the assumed, internal structure of the hybrid system was studied via gel electrophoresis, TEM and FTIR. The clear charge opposites of the Si NCs and Ag_{29} NCs was a reason to determine the zeta potential for the Si-Ag_{29} NC hybrid system, which is located close to zero. A scheme with positions for Si NCs, Ag_{29} NCs and Si-Ag_{29} NCs predicted from their zeta potential is shown in figure 7.4 A. Si NCs appear closer to the cathode, which does not match the prognosis, but a zeta potential close of about zero means the amine group has the ability to adapt to its environment and the NCs charge can easily change. Taking the positions of Si NCs and Ag_{29} NCs into account, the final position of the Si-Ag_{29} NCs in the gel in figure 7.4 B is following the direction of the Si NCs, but the charges balance each other and the hybrid system moves only a minimal distance into the gel. However the highlight of the gel electrophoresis experiment is the appearance of the red PL characteristic for Ag_{29} NCs close to the insertion well, because it is a first evidence for the successful linkage of the NCs via EDC coupling.

TEM and HRTEM investigation of Si-Ag_{29} NCs was performed in combination with an element dispersive x-ray (EDX) mapping analysis. Due to the nature of Si NCs to become a sticky solution upon concentration, the Si-Ag_{29} NCs therefore formed great sphere during the investigation process. The pictures in figure 4.3 show the formed, great spheres in A and under high resolution spheres within those can be assigned to Si NCs by the size. The EDX mapping analysis shows Si as a prominent element spread over the investigated great spheres. Hence the detected spheres are the Si NCs and the determination of the elements Ag and S, which only can be assigned to lipoic acid within the Ag_{29} NCs, allow the statement that Ag_{29} NCs are evenly distributed between the Si NCs. Sulphur is located in the same region as Ag meaning that Ag_{29} NCs stayed intact and as neither Ag nor S are found in the free space next to the great spheres the coupling formed the aimed for connection between the nanoclusters.

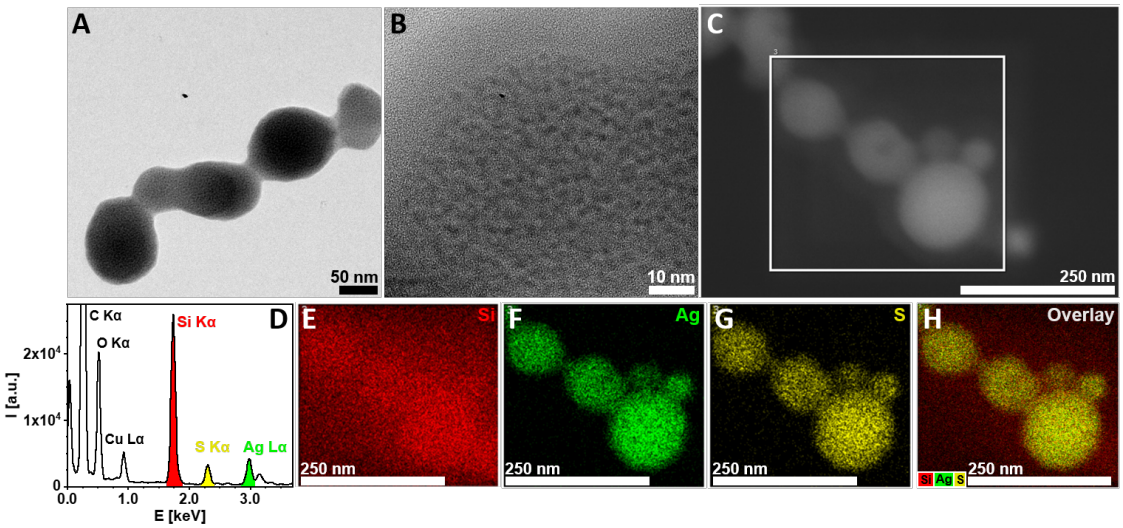

Figure 4.3: TEM (A) and high-resolution TEM (B) picture of Si-Ag_{29} NCs. Element dispersive x-ray mapping analysis (C & D) of Si-Ag_{29} NCs with the elements Si (E), Ag (F), and S (G) and their overlay (H). In manuscript.

FTIR characterization was performed to support the assumption of the successful coupling. The FTIR transmission spectra of Si-Ag_{29} NCs and Ag_{29} NCs is shown in figure 7.6 and Table 7.1 lists the main peaks. Both samples show peaks of carbon stretches of $-CH_2$ and $>CH_2$ scissor resulting from the carbon backbone of the ligands. Stretches like -NH, -COOH or Si-O can be directed to Ag_{29} NCs or Si NCs. EDC coupling results in amide bonds, which are unique to the Si-Ag_{29} NC hybrid system, but compared to the total number of free ligand groups are of small number. The amide-related peaks at 1631 cm^{-1} and 1488 cm^{-1} have a low intensity, but is a proof for the successful formation of the hybrid system.

With the inner structure of the hybrid system identified, the properties of the energy transfer process between the nanoclusters were studied through sets of coupled and uncoupled hybrid systems with a varied ratio from 0.25 to 2 between the two nanocluster species and the fraction of Si NCs is kept constant. Under UV light the set of the coupled Si-Ag_{29} NCs shows a colour change from blue to red photoluminescence, which is depicted in figure 4.4. The set of the only charge-attracted Si+Ag_{29} NCs hybrid system shows also a colour change from blue to red but of lower intensity. This difference of relative intensity can be linked to the different connections between the two nanoclusters. The Si-Ag_{29} NCs hybrid system is based on a chemical bond between the ligands, which keeps the nanoclusters at a constant distance that is favourable for FRET. The Si+Ag_{29} NCs possess a greater distance due to the charge

attracted connection within an aqueous solution. The distance is crucial for FRET and with greater distance the energy transfer efficiency is reduced, which results in the seen reduced PL intensity.
Upon the discovered colour change within the sets of the hybrid systems, the PL characterization was utilized to gain inside into the PL peak change from ratio sample to sample. Figure 4.4 depicts the ratiometric development of Si-Ag_{29} NCs PL with the peak characteristic for Si NCs located at 500 nm decreasing and at 660 nm for the Ag_{29} NCs increasing with the rise of the ratio value. Such a ratiometric change serves as a strong support of the energy transfer theory. As the transfer process results in an reduced number of excited states in the Si NCs LUMO and an increased number within the Ag_{29} NCs LUMO, a PL intensity shift has to be found for both characteristic PL peaks. Hence, the PL intensity of the Si NCs fraction would stay constant if an ET would not reduce the number of the excited states. The graph of the ratiometric change holds up another inside to be drawn from the stagnation of the Si NCs PL intensity decrease at high ratio values. Spacial coordination of the two nanoclusters in the hybrid system becomes limited factors like available space and/or charge effects. Therefore the coordination space around the Si NC donors become occupied at high ration, resulting in a plateau for the total energy possible to be transferred.
To compare the coupled and charge-attracted hybrid system in figure 7.10 with each other as well as to FRET capable hybrid systems incorporating other nanoclusters, the transfer efficiency was determined. Therefore every spectrum became processed using a ratiometric method. [49] The combined spectrum became fitted with Gaussian functions for each of the two peaks and corrected by the leakage of one emission into the other. The spectra for the ratio 0.75 with the calculated fits are shown in figure 7.9. This correction is necessary to fully separate the spectra from each other, because the instrumental setup was not capable to deconvolute the spectra in the measurement process. The total intensities of the donor I_D and the acceptor I_A emission, where afterwards used in equation 4.3 to determine the efficiency E.

$$E = \frac{I_A}{I_D + I_A} \tag{4.3}$$

The efficiencies for all ratio values for the coupled and charge-attracted hybrid system are plotted in figure 7.10 and listed in table 7.2 with schemes of the hybrid systems indicating the coupling nature. Si-Ag_{29} NCs reaches a maximum efficiency of 63 %, which exceeds the maximum of the Si+Ag_{29} NCs by 14 %. For better comparability the data points were fitted by a non linear curve fit under use of Levenberg Marquardt

iteration algorithm.

$$y = A_1 \cdot exp\left(-\frac{x}{t_1}\right) + y_0 \tag{4.4}$$

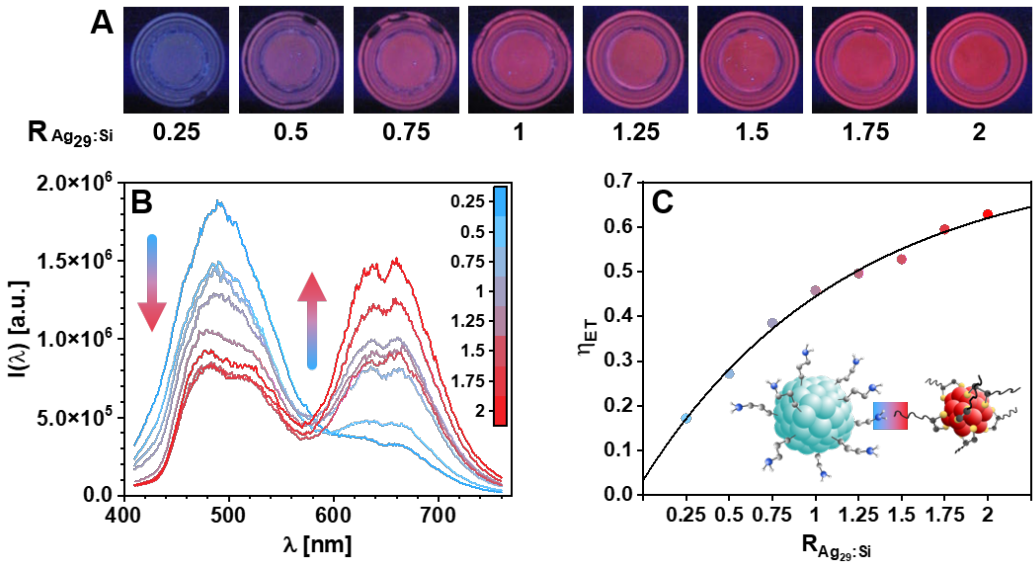

Figure 4.4: Pictures of the Si-Ag_{29} NCs hybrids system under UV light at ratios $R_{Ag_{29}:Si}$ 0.25-2 (A). In manuscript.

To tackle the complexity of the dynamics within the Si-Ag_{29} NCs hybrid system during the FRET process, the lifetime (LT) of the coupled Si-Ag_{29} NCs system was measured under an excitation of 405 nm for emission wavelengths of 450 nm characteristic to Si NCs and 650 nm for Ag_{29} NCs. The decay curves were exponentially fitted with three components and based on this fitting the intensity weighted average was determined. The decay curves and the lifetime values completed with the according PL and Abs spectra are shown in the Appendix Figures 7.11-7.24. For Si NCs a short lifetime of 10.3 ns has been found and the lifetime of Ag_{29} NCs was calculated to be 67.1 ns, but did not fully decay within the maximal reasonable time span. The rise of the ratio value causes a decrease of the LT for the Si NCs to 6.9 ns. The LT of the Ag_{29} NCs upon excitation of 405 nm at 650 nm has a value of 9.8 ns at a ratio of 0.25. The high number of donors influences the decay process resulting in the LT close to pure Si NCs. As the number of acceptors increases, non-emissive processes within the Si NCs become the dominant, which results in the lower LT for the Si NCs component. Additionally the influence on the Ag_{29} NCs LT is reduced, but does not vanish completely. This is recognisable by lower LT for the Ag_{29} NCs component than the pure Ag_{29} NCs and reaching a saturation as previously seen in the PL characterization. The energy transfer influences the processes within the

LUMO in the Ag_{29} NCs, which shortens the time until the relaxation and the PL emission appear. Therefore the shorter LT at high ratios can be measured for PL at 660 nm.

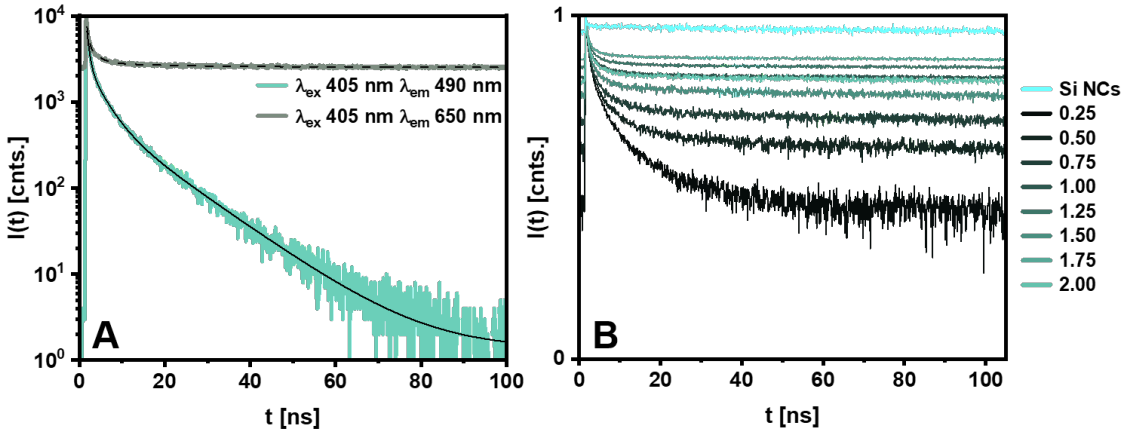

Figure 4.5: Fluorescence decay of a Si-Ag_{29} NCs hybrid at ratio 1.25 under excitation at 405 nm and the emission detected at 490 nm and 650 nm (A). Lifetime decays of the Si-Ag_{29} NCs hybrid system at ratios $R_{Ag_{29}:Si}$ 0-2 excited at 405 nm and detected at 650 nm (B). In manuscript.

The Si-Ag_{29} NCs hybrid structure and the occurring FRET process have been studied with various methods. A combination of Hoechst Blue (HB) and Ag_{29} NCs was used as a complementary system to investigate if the found parameters for Ag_{29} NCs as the acceptor moiety persist. HB is a positively charged molecule with a zeta potential of 15 mV (fig. 7.25) and will replace Si NCs as the donor species. HB and Ag_{29} NCs form a FRET pair based on the attraction of their opposite charges. The final zeta potential of the HB + Ag_{29} NCs is clearly dominated by the negative potential of the NCs. Figure 7.27 shows the absorbance and PL spectra of the two compartments and the FRET pair. The absorbance spectrum of the FRET pair shows the three characteristic peaks of the Ag_{29} NCs with an enhancement of absorbance value due to the overlay from HB and Ag_{29} NCs between 300 and 400 nm. Together with the PL spectra showing that the PL maxima are separatable, it can be stated that the Ag_{29} NCs stay intact. However the PL of HB in the spectrum of the FRET pair is mostly vanished and only a small hump bevor 400 nm and the shoulder at 580 nm indicate HB is intact. This behaviour supports the predicted FRET occurring between HB and Ag_{29} NCs.

The recording of 2D PL spectra of HB and HB + Ag_{29} NCs in Figure 7.28 shows the HB maxima located at 500 nm for excitation from below 300 nm to 400 nm

(7.28B) and in combination with Ag_{29} NCs (7.28C) becoming very faint but the ET lets emission around 650 nm appear, which can be assigned to Ag_{29} NCs.
This strong contrast between the PL spectra called for LT characterization to get an idea on the impact of the FRET on HB and to be able to compare the behaviour of the Ag_{29} NCs in the two FRET systems. Figure 7.28 shows the short LTs of HB compared to LTs of Ag_{29} NCs reaching LT upto 2 µs upon excitation at 340 nm. Comparing the LTs of HB and HB in combination with Ag_{29} NCs relaxation processes faster that 2.5 ns remain emissive. Otherwise the energy is transferred to the NCs accelerating the processes within the NCs and lowering the LT to 1390 ns. Through the extreme difference between the two LT duration the evaluation of the results becomes complex. Similar to the case of the Si-Ag_{29} NCs the lifetime of the Ag_{29} NCs did not decay completely and a second excitation influences the measurement. The short LT of HB are influenced by the limit of detection as well as the noise.
Variation of the concentration of HB from 10 mM to 100 mM combined with a fixed fraction of Ag_{29} NCs has been studied for the ratiometric behaviour parallel to Si-Ag_{29} NCs. The absorbance spectra of HB and HB + Ag_{29} NCs in Figure 7.29 C&A shows the peak at 350 nm rising as the concentration of HB increase and shifting to 340 nm in combination with Ag_{29} NCs as their prominent peak is located at 330 nm. The peaks at 430 nm and 500 nm characteristic for Ag_{29} NCs hardly change in value and position, stating that the nanoclusters stay intact upon the increasing number of HB. The PL characterisation show on the one hand the ratiometric behavior of the FRET pair and on the other the self-quenching behaviour for HB, when studied alone. The presence of the negatively charged Ag_{29} NCs reduces the effect of self-quenching within the studied concentration range. The coordination of the opposite charged moieties separates the HB molecules and FRET enhances the PL intensity of the NCs PL. Nevertheless the expected increase of the HB PL at 500 nm stagnates for the highest concentrations, point towards an rising impact of the self-quenching again. The quenching process interrupts the ET process, which decreases the PL intensity at 660 nm. The free HB molecules now dominate in the PL emission process and the distance to the Ag_{29} NCs prohibits an ET.
Finally the competitive behaviour between the two donors Si NCs and HB in the presence of Ag_{29} NCs was studied for the chemically bound and only charge attracted hybrid system of Si NCs and Ag_{29} NCs. For this experiment the ratio of 1 between Si NCs and Ag_{29} NCs was chosen and the PL spectra collected with an excitation of 390 nm are shown in figure 7.30. The donors differ in the total charge of the molecule/nanocluster as well as in the overall size. Although both attracted to the

Ag_{29} NCs, a repulsion between the two donors has to be expected, but HB will take advantage of its small size and could push Si NCs aside. The PL spectra present a clear difference of the interaction of HB with the hybrid system depending on the link nature. The chemical bond between the two nanoclusters hinders the penetration of HB into the structure and the PL of the Si-Ag_{29} NCs system shows a similar spectrum as previously measured. Only the peak around 500 nm changed in shape and the PL of HB overlaps with the Si NCs PL, which broadens the peak towards lower wavelength. A significant difference appears for the uncoupled Si + Ag_{29} NCs system in a strong increase of the Ag_{29} NCs PL. HB can differ into the nanocluster system and replace the Si NCs. Therefore HB gets into range for FRET and becomes the prominent donor with change in transfer efficiency. The shape of the peak at 500 nm shows only a shoulder towards 450 nm, meaning less emission is send out from HB and therefore is transferred as energy. In this spectrum the emission of Si NCs is leading for the peaks maximum through the reduced ET. The coupled Si-Ag_{29} NCs can withstand the intervention even of such a small, more positively charged donor like HB.

5 Ag_{29} NCs on Zinc Oxide Tetrapods

5.1 Zinc Oxid

Zinc oxide (ZnO) is a widely known II-VI semiconductor with a direct bandgap of 3.4 eV in the near UV region. This large bandgap results in a clear and colourless material. ZnO crystallizes in either cubic zinc blende (ZB), hexagonal wurtzite (WZ) or rocksalt structure. Anions are each surrounded by four cations and vice versa forming a tetrahedron as the unit cell with an emerging ionic bond component. The ratio of the elementary translation vectors c/a has a value of 1.60. The ionic feature of the bond is the reason for the formation of LUMO by the 4s levels of Zn^{2+} and the HOMO from the 2p levels of O^{2-}. The wurtzite structure is the thermodynamicly stable phase and cubic structures are necessary for growth of ZnO in the zinc blende structure and the rocksalt structure forms under high pressures. This variety of stable crystal structures lets ZnO exhibits polytypism. Tetrapods are composed of a zinc blend core of which four hexagonal wurtzite arms branch out. The change between the crystal structures is favoured due to the same facet structure of the $(000\bar{1})$ wurzite facit and the (111) zinc blend facet. [50] Although the internal morphology is identified, the growth process is not agreed on and several models are proposed. [51] Shijiri and Kaito [52] state a rapid WZ growth of the four arms from a below 20 nm, ZB nucleus perpendicular to the (111) facet. Another model proposes, that the core and arms are in wurzite structure, growing in an octa-twin model, which separates due to cracking of the twin boundaries into tetrapod structures. [53–55]

5.2 ZnO nanostructures and their optical properties upon hybrid material formation

The optical properties originate from the surface morphology and the induced defects like vacancies, interstitial or doping with elements like nitrogen. The typical spectrum

of ZnO structures has two main attributes. One peak arises around the bandgap energy and the second peak is located in the green region of the spectrum. The green luminescence (GL) is a composition of photoluminescence from defects. Hybridisation modulates the surface morphology resulting in a main peak modification and arise of additional peaks, allowing tracking of changes by PL changes. [56] David Mora-Fonz et. al. used the Monte Carlo procedure to modulate the surface atom patterns found by STM. Triangular and striped morphologies appear to be polar surfaces and hexagonal patterns additionally are found to be oxigen terminated. The polarity and morphology is key to surface modification with nanoparticles. [57] From 2007/2008 adsorption of long-chain molecules like oleyl chains or dodecanes with functional carboxylate, phosphate or thiol groups onto ZnO nanostructures like tetrapods were studied. Through covalent linkage a uniform coverage is reached. From there solubility in non polar solvents has been achieved [58] or coating the Zn-terminated surface with sulphur. [59] Attached Au nanoparticles on ZnO nanorods were able to enhance the photocatalytic oxidative properties of the ZnO. [60] Through their unique, four-legged structure, tetrapods self-orient mostly in the same way on a substrate surface, creating a hybrid structure with great, easy accessible surface to build sensing devices. Such composites were created from ZnO tetrapods functionalized with various metal oxides and alloys like TiO, Fe_2O_3, Bi_2O_3 or CuO. These modifications improved limits of detection or allowed sensing close to room temperature instead of 250-300 °C. [61–68]

5.3 Aim of work

Dictated by the fabrication process, Ag_{29} nanoclusters exist as a aqueous, colloidal solution. They have been characterized in solution with various methods and their unique photoluminescence features arising from their molecule-like properties have found their way in several current research projects. To investigate their optical behaviour in a different environment comes with the need of a supporting structure, to which the Ag_{29} NCs could be connected. To follow the changes occurring to the nanoclusters and their optical properties, a well-studied material is needed. Here ZnO tetrapods have been chosen as a backbone. Zinc oxide as a material is studied since decades and lately also structures like wires or tetrapods have been characterized as well as paired with various materials. Therefore, changes in the optical properties of both compartments can be identified and conclusions for the properties of a hybrid material can be drawn. This would allow to get creative and find use for such a

material in the fields of sensing, photocatalysis and anti-microbial applications.

5.4 Results and Discussion[2]

ZnO tetrapods in their pure form after flame transport synthesis appear as white powder. When illuminated with UV light, a green/blue emission can be noted. The Ag_{29} NC synthesis solution shows an orange colour and a strong red emission under excitation. The newly formed material shows an orange colour and glows in a yellow colour as the result of the incorporation of Ag_{29} NCs into the ZnO tetrapods as presented in the scheme of figure 5.1 A and the insets.
The structure of the AgNC@ZnO Tps hybrid material was characterized by TEM and STEM as shown in figure 5.1 B and C. The high resolution inspection shows a homogeneous distribution of Ag nanoparticles covering the surface of ZnO Tps. The found particles show a greater size as found for Ag_{29} NCs in Figure 7.1. The investigation with high energy electron beams induce an degradation process happening simultaneously to the characterization. The degradation is a result of decomposition of the stabilizing ligand and agglomeration of the individual nanoclusters. Both processes result in the formation of Ag nanoparticles.
Confocal laser scanning microscopy (CLSM) has the ability to investigate the structure ZnO tetrapods and collect the strong red emission of the excited Ag_{29} NCs. The red luminescence can be found around the center core of the ZnO tetrapod structure and along the arms as seen in figure 5.1 D. The fading luminescence on the tetrapodal arms occurs due to decreasing ZnO surface area were a lower number of Ag_{29} NCs can be deposited. When concentrated to a small space, the effect of aggregation-induced emission (AIE) applies for Ag_{29} NCs. This leads to an emission enhancement at the center of the tetrapod structures.
The elemental analysis by HAADF-STEM EDX mapping in figure 5.1 E shows the Zn of the tetrapod surface. In circular patches Ag can be detected distinctively and also sulfur is present in the areas. The source of sulfur is the lipoic acid capping the Ag_{29} core. The spreading of sulfur on Ag-free areas results from the degradation process.
At high resolutions the Ag NPs show a crystalline Ag core and the fast Fourier transformation (FFT) presents intensities, which can be dedicated to metallic silver ($Fm\overline{3}m$ space group and lattice parameter $a = 4.09$) and Ag_2S ($Im\overline{3}m$ space group and lattice parameter $a = 4.89$Å).

[2]The data of this work has been published in [4].

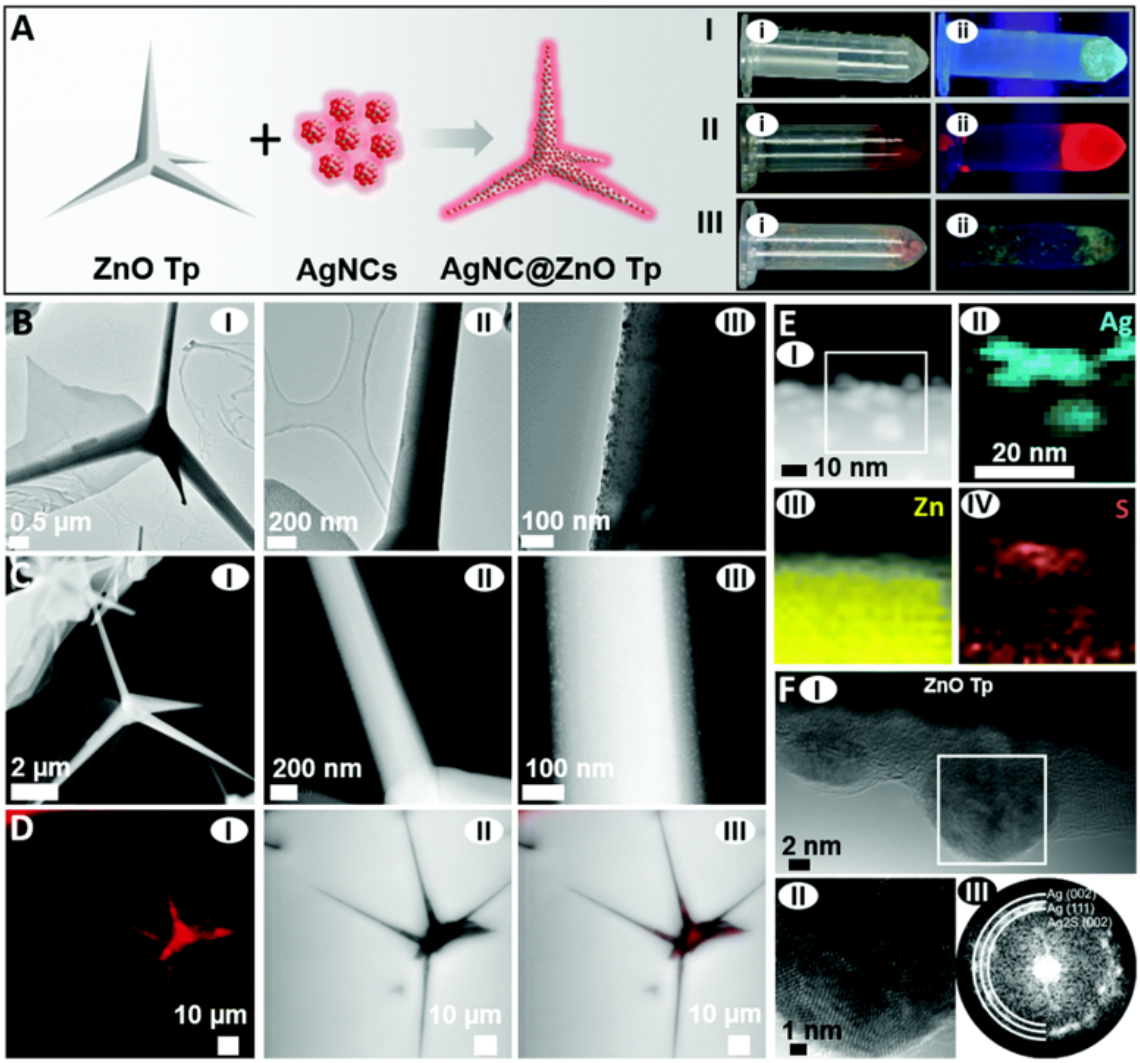

Figure 5.1: (A) Scheme of the AgNC@ZnO Tp synthesis. The insets show the ZnO Tp (in water) (I), AgNC (synthesis solution) (II), and AgNC@ZnO Tp hybrid (dry) (III) under visible light (i) and UV light excitation (ii). (B) TEM and (C) high-angle annular dark-field (HAADF)-STEM images of the AgNC@ZnO Tp hybrid at different magnifications (I-III). (D) Confocal laser scanning microscopy (CLSM) images of the AgNC@ZnO Tp excited at 3.06 eV/405 nm; (I) showing a PL below/above 2.0 eV/615 nm, (II) bright-field image, and (III) the overlay of bright-field and PL intensity images. (E) HAADF-STEM image (I) with EDX elemental mapping for the elements (II) Ag, (III) Zn, and (IV) S. (F) HRTEM micrograph (I), a magnified HRTEM micrograph of an AgNC(II), and the respective FFT (III) are shown. Prepublished in [4]

In the structure of the hybrid material Ag_{29} NCs are located on the surface of the ZnO tetrapods. The effect of the strong absorption of the NCs at the interface were expected to influence the vibrational modes of the ZnO lattice. Figure 5.2 shows

the ZnO modes detected for separate spots on the sample. For the characterization the samples were excited at 2.8 eV/442 nm, which is an excitation wavelength of significantly strong absorption for Ag_{29} NCs (7.3). The hexagonal wurtzite structure is raman-active showing modes A_1, E_1, E_2, the overtones and the combinations. These can be connected to second-order Raman scattering processes with overlain longitudinal optical (LO) phonon modes at frequencies 1000-1200 cm^{-1}. The difference between the ZnO Tp modes can arise from polarization effects originating from the orientation of the tetrapods and the incident wavevector of the incoming laser beam. The same investigation was performed for the AgNC@ZnO Tp structure. The prominent modes $E_2{}^{high}$ and 'LO overtones + combinations involving LO modes' were reduced in their relative intensities as the Ag_{29} NCs absorb and scatter the incoming light. In particular the region of high wavenumber is affected with an increase of the LO overtones. The lipoic acid ligands of the NCs also contribute to the modification of the LO overtones. The ratio between $E_2{}^{high}$ and LO overtones is lower than in ZnO tetrapods also but consistent within one sample. The variation of the excitation density with a neutral density filter does not change the spectra in frequencies or leads to peak broadening as shown in figure 5.3. The consistency of the overall shape indicates an efficient diffusion of the local heating and maintenance of the high surface stability.

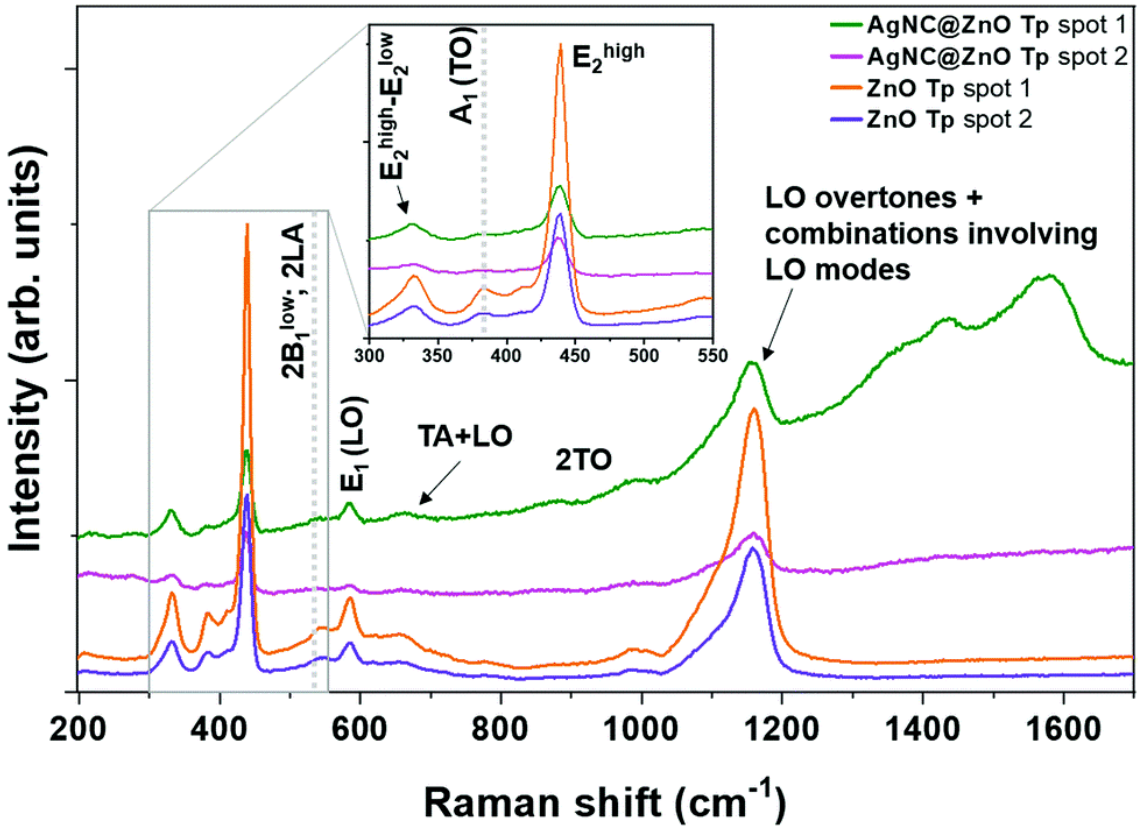

Figure 5.2: RT Raman spectra obtained with 2.8 eV/442 nm laser excitation (using a 0.3 neutral density filter (ND0.3)) for both ZnO Tp and AgNC@ZnO Tp hybrid, probing different points of the samples. Vibrational mode indexation is according to ref. 47. The spectra were shifted vertically for clarity. Inset: Enlarged view of the E_{high} 2 mode spectral region. Prepublished in [4]

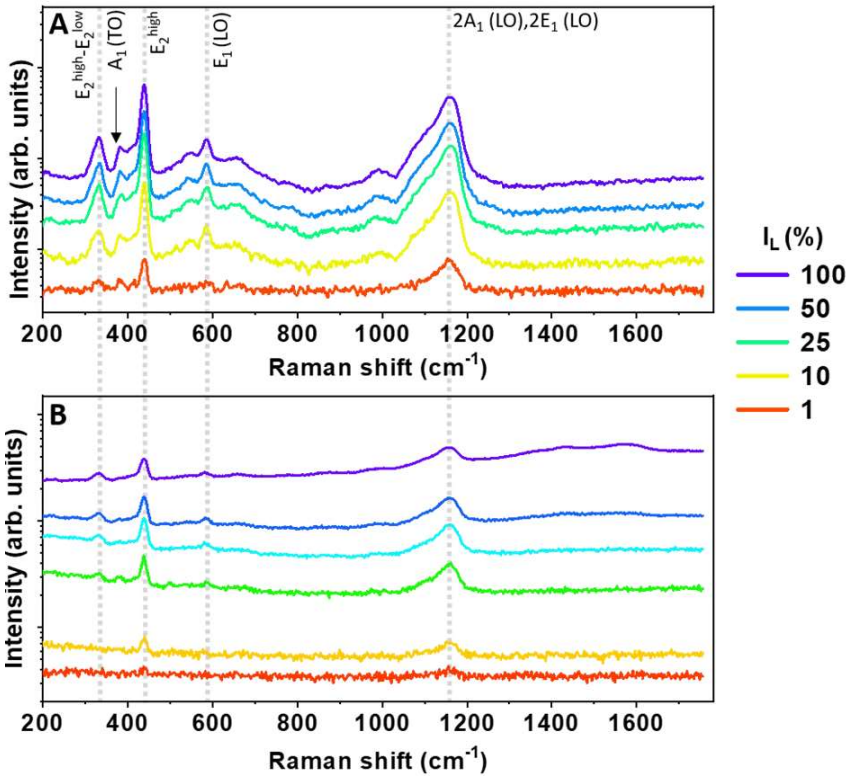

Figure 5.3: Excitation density dependence Raman spectroscopy study carried out with 2.8 eV/442 nm excitation for the (A) ZnO Tp and (B) AgNC@ZnO Tp samples. The spectra were shifted vertically for clarity. Prepublished in [4]

ZnO tetrapods and Ag_{29} NCs respond to excitation with UV light as shown in figure 5.1 AI & II. This properties can be utilized to characterize changes of ZnO emitting defects, charge transfer processes and other interactions with the Ag_{29} NCs. Photoluminescence spectroscopy at different temperatures, densities and over time enables to study these attributes. figure 5.4 shows normalized PL and PL excitation (PLE) spectra collected at room temperature (RT) of Ag_{29} NCs in aqueous solution (5.4 A), ZnO Tps (5.4 B) and Ag_{29}@ZnO TPs (5.4 C). The molecule-like nature of Ag_{29} NCs results in distinct, characteristic absorbance bands at 335 nm/3.70 eV, 435 nm/2.85 eV and 500 nm/2.48 eV, when studied in aqueous solution (7.3). The PLE spectra in figure 5.4 A at 620 nm and 705 nm reaches from 620-335 nm/∼2.0-3.7 eV and shows peaks at these values. Upon excitation close to the absorbance bands, a strong, red emission with the maximum at 652 nm/1.9 eV and a full width at half maximum (FWHM) of 250 meV is detectable. This emission is presented in figure 5.4 A. The optical features of ZnO are shaped by the bandgap. The emission spectrum is dominated by the green luminescence (GL), which is a result

of excitation at lower energies. Next to this deep level recombination, shallow level recombination generates a UV NBE emission. The domination of the GL is driven by the temperature at experiment performance. A temperature dependent PL study will be discussed in a later passage. The mutual influence of the ZnO tetrapods and Ag_{29} NCs in the hybrid structure results in the PL spectra presented in figure 5.4 C. Excitation at UV light generates an unchanged ZnO emission and also the PLE for GL emission shows the steep edge due to the ZnO band edge. Excitation characterization was performed with photons of energy exceeding the bandgap energy. At this high energy a shift in the Ag_{29} NCs emission towards lower energies 1.73 eV/717 nm occurs. The PLE for a wavelength ascribed to the new maximum shows the significant change noticeable by a decrease of the relative intensity of the band and the absence of high energy features. A prominent change is noticeable by the increase of the excitation bands as well as a decrease of the relative intensities with the absence of high energy electronic excitation. Here an increase of the FWHM from 250 meV for NCs in solution to 360 meV in the hybrid system. The unique red emission is connected to excitation at lower energies in the blue/green region 2.8 eV/442 nm and 2.44 eV/508 nm. The particle-particle interplay in the hybrid structure affects the arrangement of the electric bands in their separation. This interplay is a first indication of inter band charge transfer between the ZnO tetrapods and Ag_{29} NCs. To enlarge the inside PL characterization were performed under variation of excitation density, temperature and overtime.

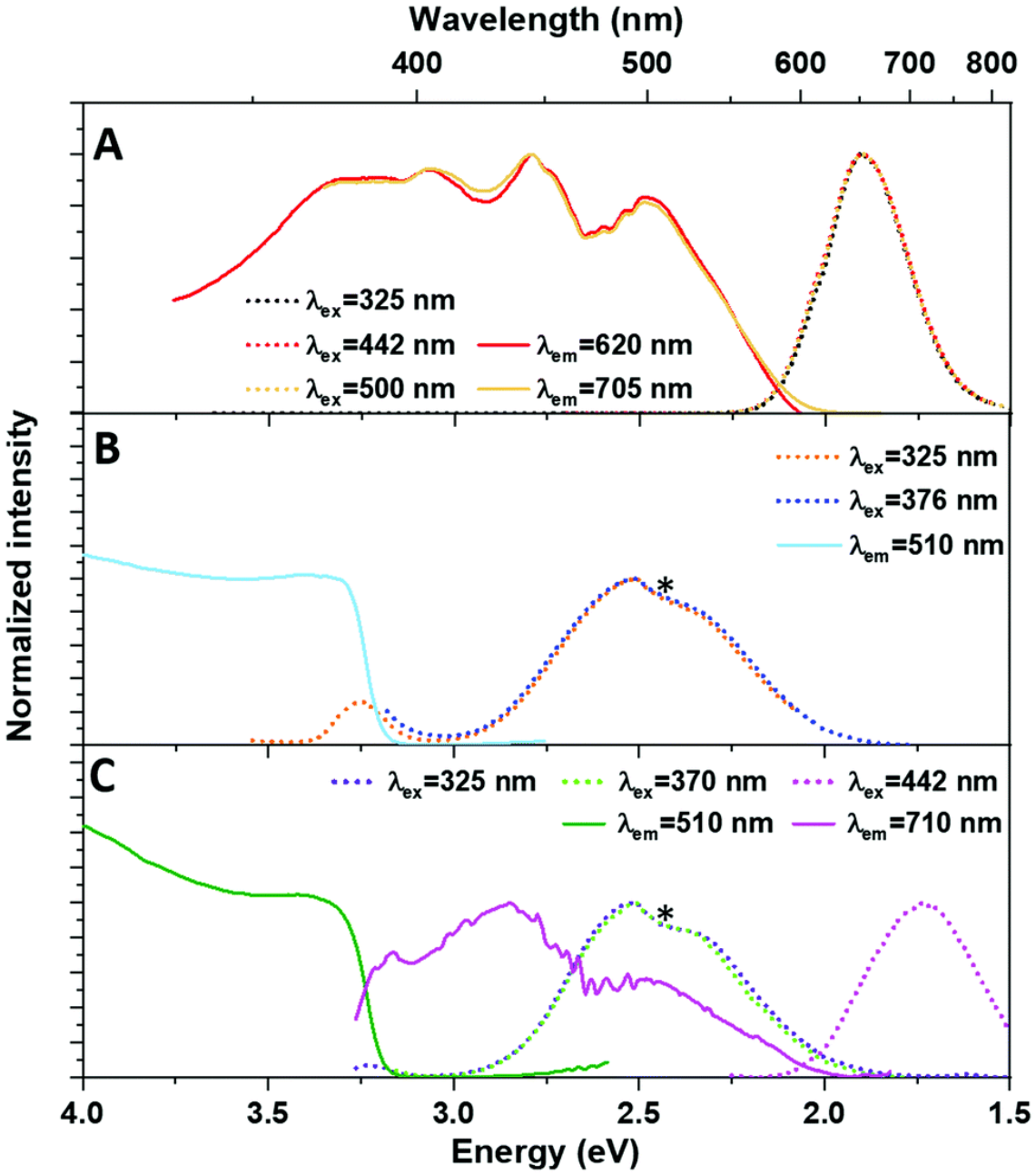

Figure 5.4: Normalized RT PL/PLE spectra obtained for AgNC in aqueous solution (A), ZnO Tp (B), and AgNC@ZnO Tp hybrid (C). The asterisk denotes an artefact of the system. Solid lines correspond to the PLE spectra, while dashed lines denote the PL spectra. Prepublished in [4]

The first evidence of an excitation-density dependency is found, when comparing the PL spectra recorded under excitation with a Xe lamp or a He-Cd laser. figure 5.5 A shows the data by Xe lamp excitation in blue lines and by He-Cd laser excitation in green lines. Both samples were excited at 3.8 eV/325 nm. After normalization of the intensities, it is observable that the GL is shifted to lower energies for the laser

excited probes. This effect is more present for the hybrid material. The difference under laser excitation initiated the follow up experiment of varying the excitation density of the He-Cd laser to identify the components contributing towards the GL spectra of ZnO Tps and AgNC@ZnO Tp hybrid. The difference in shape and peak positions vanishes when the excitation density is lowered via a neutral density filter to 1%. Like graphed in figure 5.5 B the graphs become coincident. The peak maximum stays located at lower energies compared to Xe lamp excited spectra due to the lower excitation power of the lamp (∼2.36 eV/525 nm vs. ∼2.46 eV/504 nm). This findings indicate that high-energy components of the GL are dominant at low excitation density and an increase of the excitation density allows recombinations of low energy components become prominent in the spectra. Such a shift in dominance of different energy components occurs in both samples, which show a coincident for low excitation densities. Therefore, the samples were probed at different excitation densities and the spectra were deconvoluted into Gaussian component representing the expected recombination channels.

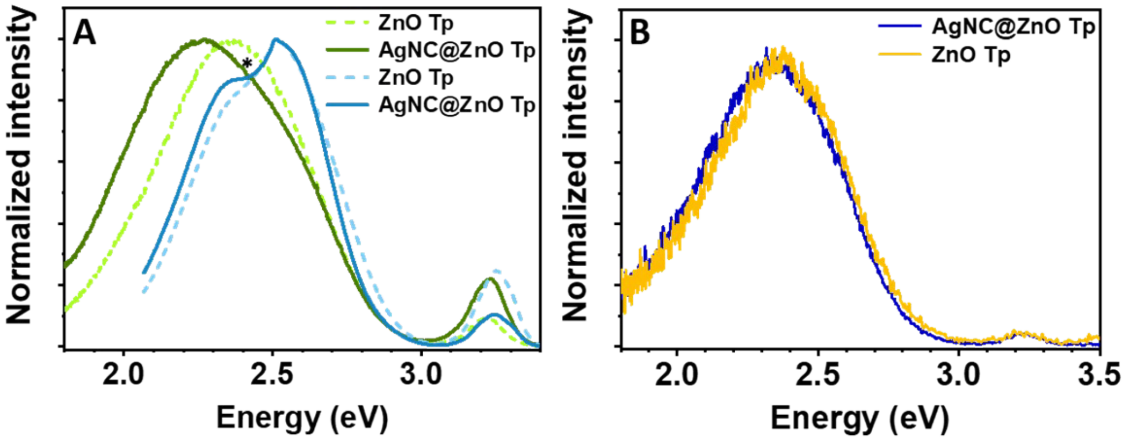

Figure 5.5: (A) Comparison of the normalized RT PL spectra obtained under 3.8 eV/325 nm excitation, exciting with either the Xe lamp (blue lines) or the He-Cd laser (green lines), for ZnO Tp (dashed) and AgNC@ZnO Tp (solid) samples. The asterisk denotes an artefact of the measurement system. The spectra were also obtained in two different measurement equipment, according to the type of excitation source. (B) Comparison between the normalized spectra obtained with the same excitation energy and acquired with 1 % of the nominal laser power for the ZnO Tp and AgNC@ZnO Tp samples. Prepublished in [4]

Varying the excitation density between 1 % and 100 % shows a steady intensity increase for both samples likewise (fig. 5.6). For the AgNC@ZnO Tp hybrid,

the peak position of the GL shifts towards lower energies following the increased excitation intensity. This asymmetry indicates a changing intensity of more than one recombination channels. At low excitation densities the relation of the recombination channels within both samples approximate towards each other. For the endpoint cases of 1 % and 100 %, the convolution using three Gaussian with peaks at ∼2.6 eV/477 nm, ∼2.4 eV/517 nm, and ∼2.2 eV/564 nm is plotted in figure 7.31. The approximation between both samples becomes visible for 1 % excitation density. This progress of the intensities of the Gaussian allows the explanation of the GL shift for the hybrid material. In particular the Gaussian with the peak at ∼2.4 eV/517 nm becomes prominent for both samples and leads to the similarity in the GL spectra which matches the spectrum under excitation with the Xe lamp. The development of the integrated intensity of the three Gaussian plotted against the excitation density is shown in figure 5.6 C&D. The slope of the linear approximation allows to draw conclusion on the type of radiative transition. A slope m smaller 1 points to donor-acceptor pairs (DAPs) and free-to-bound carrier recombination and a slope between $1 < m < 2$ is an indication for an exciton-like transition. Given that here the slope is close to 1, all three recombination natures have to be considered. The steady decrease following the excitation without a peak shift minimizes the possibilities to free-to-bound recombination and exciton-like type. Additionally an investigation over the first millisecond after the excitation at ∼3.81 eV/325 nm was performed with a time window of 10 ms. For both samples the visible band disappears within 0.2 ms, pointing to a lifetime in the microsecond range. Comparing the spectra with each other the shape and position does not change similar to the excitation density study. This is a second evidence that the same recombination channels contribute to the GL spectrum.

Defects within ZnO structures are reported to give rise to the luminescence in the green region. [69,70] Known defects in zinc oxide are oxygen/zinc vacancies (V_O/V_{Zn}), zinc antisites (Zn_O), interstitial Zn atoms, transitions from Zn_i to Zn_V and extrinsic impurities like Cu. Previous studies have reported that defects on the surface give rise to luminescence, which becomes significant for structures like tetrapods with a great surface area.

Complexity is added to the situation because multiple defects contribute to the resulting luminescence, where as the contribution of the single defects differs from sample to sample. Next to the green luminescence, signals in the spectral regions blue, yellow and orange/red are reported in literature, but the green luminescence is the most described and discussed. Although the chemical nature is still under discussion, the combination of several types of defects is established for the green

luminescence but not for the other luminescence.

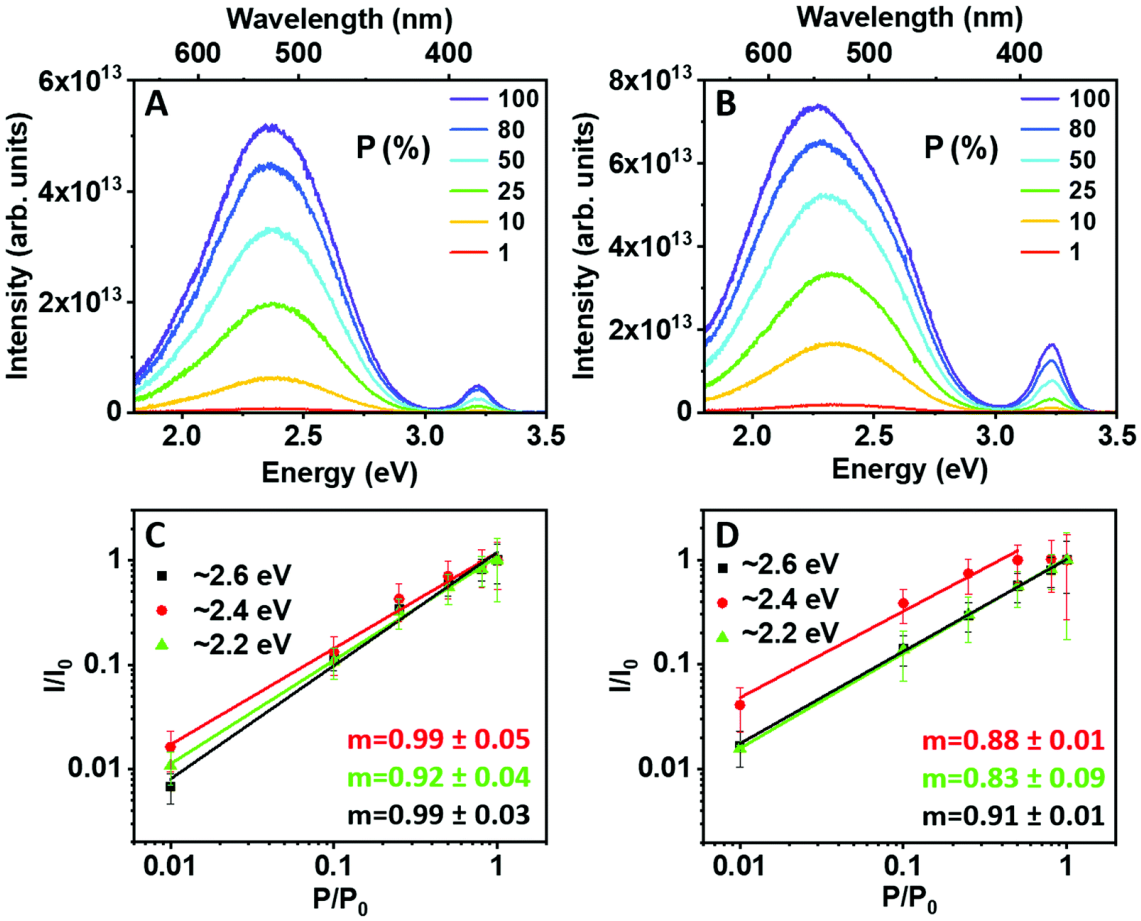

Figure 5.6: Density excitation-dependent PL spectra acquired at RT for ZnO Tp (A) and the AgNC@ZnO Tp hybrid (B) under 3.81 eV/325 nm excitation. Graphical representation of the increase of the normalized intensity as a function of the excitation density for PL bands peaked at ∼2.6 eV, ∼2.4 eV and ∼2.2 eV for ZnO Tp (C) and AgNC@ZnO Tp hybrid (D). Prepublished in [4]

Cooled down to 11 K, the samples reveal further details of the emission inducing mechanisms. At 11 K the near band edge (NBE) region from 3.2 to 3.4 eV dominates the spectra over the GL for both samples. For ZnO Tp the NBE region is by one magnitude greater than the GL. The hybridisation of ZnO Tp with Ag NCs modulates the intensities for the GL and the NBE region to similar intensities, but the NBE region shows 3 prominent peaks. The peak of the GL shifts from the NCs from ∼2.43 eV/510 nm for the ZnO to ∼2.39 eV/519 nm caused by the defects originating from different recombination channels.

The at 11 K emerged peaks allows an identification of the presence of free excitons

(FX), donor bound excitons (D^0X) and 3.31 eV-lines including the longitudinal optical (LO) phonon replicas with an separation energy of ∼70 meV. The enlargement of the previously described NBE region from 5.7 A in 5.7 B allows to assign the recombination channels. The ZnO Tps spectrum is dominated by the FX and D^0X peaks which is about one magnitude higher than the 3.31 eV line. For the AgNC@ZnO Tp structure the peaks of these recombination channels and the LO replica are of same magnitude and can be distinct from each other.
Although the chemical nature of the defects can not be explicitly named, the different trends of the spectra indicate a modification of the electric potentials at the metal/semiconductor interface by the Ag NCs on the ZnO surface. The modification appears in a band bending of the energy bands. This allows an enhancement of the tetrapods photoluminescence through increase of the population in the surface-emitting states. In figure 5.8 (a) a scheme of the band structure of AgNCs in solution is depicted. The energy levels for the NCs are based on the findings in the optical extinction (fig. 5.3) and the PL/PLE (fig. 5.4). Following the recent findings the scheme of fig. 5.8 A is modified for the hybrid structure. The upper LUMO of the AgNCs is located parallel to the conduction band (CB) of the ZnO tetrapods and therefore an electron transfer towards the tetrapods becomes possible. The proposed electron transfer is supported by the results of the 11 K PL characterisation as the contribution of the surface related defects are enhanced. Upon excitation with an energy of 3.81 eV electrons from the HOMO of the Ag NCs are excited into the AgNCs LUMO parallel to the CB followed by an electron transfer, which results in an emission dominated by ZnO features. An electron transfer allows a population of other energy levels within the hybrid structure than upon direct band-to-band excitation in ZnO, which can affect the position of the GL peak. Is an excitation applied with an energy lower than to reach the ZnO CB, recombination in the Ag NCs occurs from lower LUMOs, which prevents energy transfer and the significant red emission (∼1.73 eV) of the AgNCs can be observed. Temperature-dependent PL characterization shows the development from a deconvoluted state of the recombination channels at low temperature to an overlap, when temperatures rise up to RT. The deconvolution of the GL region is shown in figure 7.33 and 7.34 and the NBE region in figure 5.7. The dissociation of the D^0X due to the increase of temperature is accompanied by a decrease of the PL intensity because of nonradiative relaxation processes and the bandgap shrinkage causes a red shift. At RT the FX recombination dominates the NBE region at ∼3.28 eV/325 nm, which overlaps with the 3.31 eV line and the replicas that are associated to surface-related states. The temperature rise affects the peak position of the GL region shifting it to

lower energies, because the bandgap reduces in distance and the relative intensities of the recombination centers.

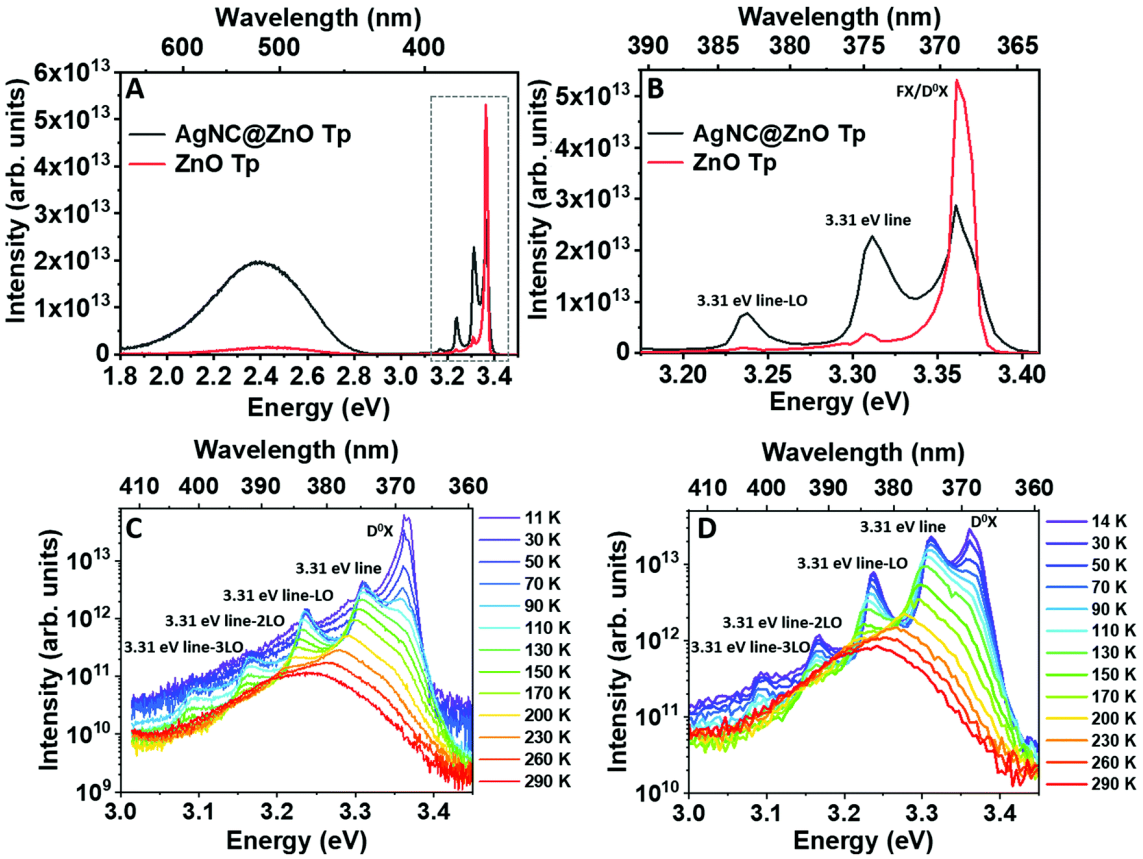

Figure 5.7: (A) 11 K PL spectra of ZnO Tp and AgNC@ZnO Tp hybrid under the same alignment conditions. (B) Enlargement of the area marked with a grey dashed line in (A). Temperature-dependent PL study performed with high-resolution steps in the NBE region for ZnO Tp (C) and AgNC@ZnO Tp (D). All spectra were collected with ∼3.81 eV/325 nm excitation. Prepublished in [4]

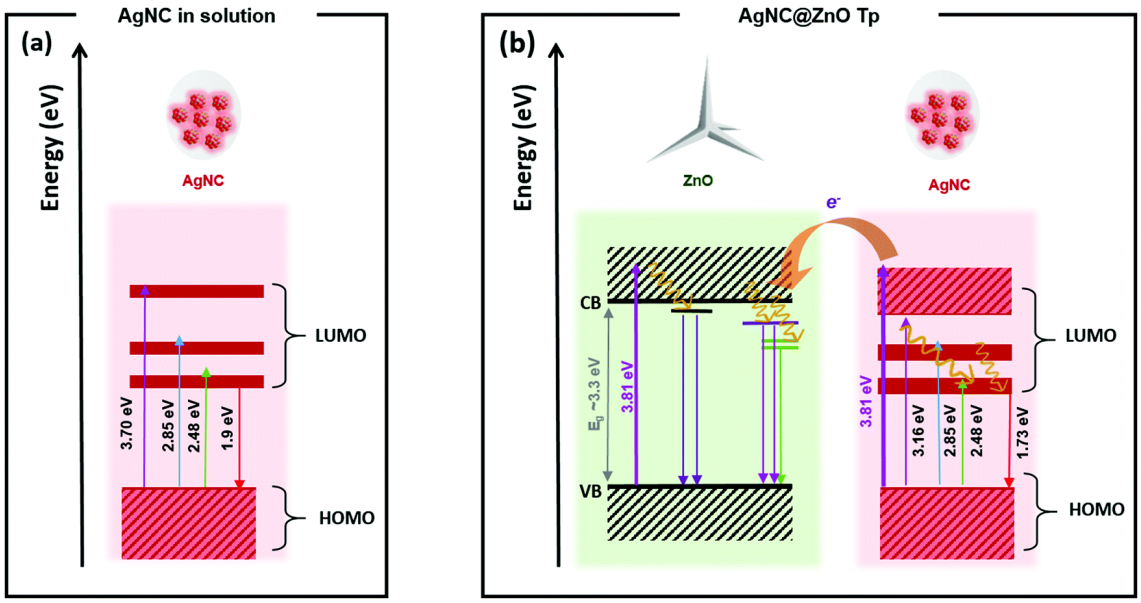

Figure 5.8: Schematic representation of the (a) energy level diagram of electronic excitation and emission transitions in the AgNC and (b) charge transfer processes that may occur between the ZnO Tp and AgNC upon the hybrid formation. Note that the spacing of the levels is not at scale. CB stands for conduction band, while VB denotes the valence band. Prepublished in [4]

After the determination of the PL characteristics of the AgNCs@ZnO Tp hybrid material, the structural constitution and the PL stability were studied over a period of 7 days. The PL spectra were measured under 2.8 eV/442 nm excitation and the CLSM images were collected under 3.06 eV/405 nm excitation. Both excitation energies are based on the discrete levels found in the PLE study (fig. 5.4). The intensity profiles shown in figure 5.9 B are recorded one, four and ten days after sample preparation under the same conditions along one tetrapod arm of the same sample pointed out by a red arrow. During this time a constant decrease of the PL intensity has been recorded. The PL characterization shows a similar decrease in intensity overtime. Noticeable is that the spectral shape is retained and does not shift, which allows the assumption that the structure of the AgNCs changes overtime. ZnO structures are known for the ability to connect moieties via dithiol linker to the surface. Lipoic acid as the stabilizing agent is a dithiol and a diffusion process to the ZnO surface can cause a degradation and therefore PL loss of the Ag NCs.

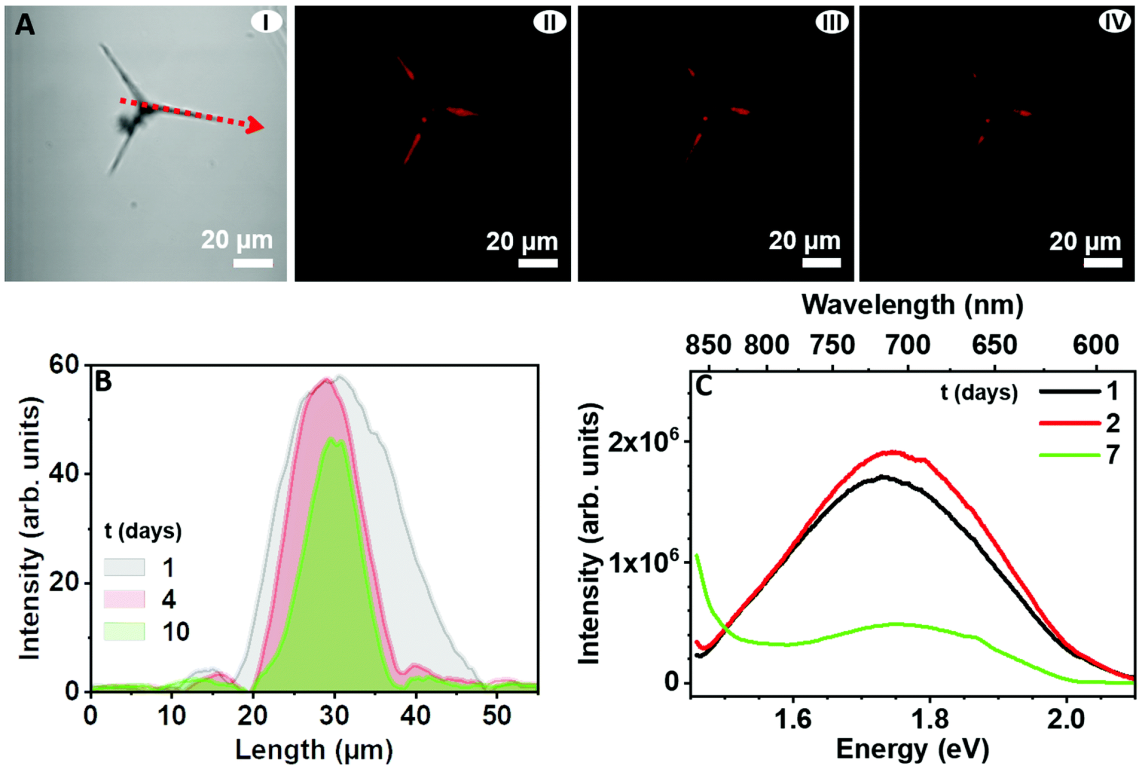

Figure 5.9: (A) Intensity change of the AgNC's PL on a ZnO Tp detected in CLSM ((I) bright-field image) from day 1 (II) to day 4 (III), to day 10 (IV). (B) Graphical representation of the PL intensity change over time. The arrow in (A) shows the axis along which the intensity change was collected.(C) RT PL spectra acquired at 2.8 eV/442 nm excitation for the AgNC@ZnO Tp hybrid 1, 2 and 7 days after the sample's preparation. Prepublished in [4]

6 Conclusion & Outlook

The present work is targeted on the investigation of the photoluminescence behaviour of $Ag_{29}DHLA_{12}$ nanoclusters via direct influence by another nanocluster species and changes of the environmental factors.

With the help of EDC coupling, the molecule-like Ag_{29} nanoclusters and size-defined silicon-based nanoclusters were directly linked with each other without length-addition. Optical characterization and electron microscopy showed that the nanoclusters keep their structure upon the ligand coupling in the hybrid structure. The interaction between the two nanoclusters was studied in a ratiometric set up, which allowed to follow the development of the properties. In the hybrid structure, the Förster resonance energy transfer was found to occur with the silicon nanocluster performing as a donor and the Ag_{29} NCs as the acceptor. The transfer of energy accelerates the internal processes. Only the short lifetime processes remain emissive in the donor and the emissive recombination in the Ag_{29} nanoclusters become more in number resulting in an enhanced photoluminescence. The efficiency of the hybrid nanocluster system of 63 % is comparable with organic dye-based hybrid systems. As an analogue system Ag_{29} nanoclusters were paired with the organic dye Hoechst Blue. The FRET process appears in similar manner with a comparable behaviour of the relaxation processes and lifetimes.
As a dual-cluster system Si-Ag_{29} NCs, the combination of two photoluminescence bares a great potential in sensing application. Next to the change of luminescence through the sensed species, the energy transfer will be affected and allow a more detailed and comparable result. Nanoclusters by themselves show a greater stability and repeatability of excitation in comparison to organic dyes. Additionally they often come with a greater biocompatibility because of the used materials and the small size allows a release from most biological organisms.

With the help of a scaffold Ag_{29} nanoclusters were separated from the surrounding environment including the aqueous medium and excess ligands. The macron-sized scaffold of zinc oxide tetrapods have been intensively studied and their behaviour

allows to understand processes occurring within the Ag_{29} nanocluster upon excitation. The contact between the nanoclusters and the ZnO surface is a circumstance not to be denied, but previous studies of the ZnO tetrapods allowed to appoint factors assigned to the tetrapod.

After confirmation of the Ag_{29} nanoclusters properties, the hybrid material Ag_{29}@ZnO Tps was excited with photons with energies greater than the ZnO bandgap (width: ∼3.4 eV at low temp.). ZnO tetrapods present the near band edge (NBE) emission in the UV region and a broad visible band in the green region. A found effect assigned to the presence of the Ag_{29} NCs are peak shifts to lower energies with an energy dependency. It has been found that several recombination channels contributing to the green band emission, become populated by additional electrons migrating from the nanoclusters in charge transfer processes. Deconvolution showed the involved surface-related 3.31 eV emission line and its increase indicating the processes to be free and bound exciton recombinations. The emission of the nanoclusters in the hybrid system shifts to lower energies and excitation with photons with energies greater than ∼3.27 eV/379 nm does not result in visible emission. The contact with the ZnO tetrapods dislocates the energy levels of the Ag_{29} nanoclusters. Consecutive investigation of Ag_{29}@ZnO Tps hybrids samples revealed a degradation process up to full vanishing of the red emission of the nanoclusters after one week. Here a combination of nanocluster aggregation, Ag oxidation and sulfidation supported through surface defects of ZnO led to the structural change in the nanoclusters.

The subsequent research for the Ag_{29}@ZnO Tps hybrid system is to aim for greater stability of the structure. Especially the factor of degradation needs to be tackled, which could be achieved via separation of the two species or redirecting the chemical potential for an other benefit of the hybrid structure. The greater picture for the Ag_{29}@ZnO Tps hybrid system is an application in the fields of sensing, anti-microbial and photocatalysis materials.

References

[1] B. Adhikari and A. Banerjee, "Facile Synthesis of Water-Soluble Fluorescent Silver Nanoclusters and HgII Sensing," *Chemistry of Materials*, vol. 22, no. 15, pp. 4364–4371, **2010**. doi:10.1021/cm1001253

[2] S.-D. Ma, Y.-L. Chen, J. Feng, J.-J. Liu, X.-W. Zuo *et al.*, "One-Step Synthesis of Water-Dispersible and Biocompatible Silicon Nanoparticles for Selective Heparin Sensing and Cell Imaging," *Analytical Chemistry*, vol. 88, no. 21, pp. 10 474–10 481, **2016**. doi:10.1021/acs.analchem.6b02448

[3] Y.-K. Dou, Y. Chen, X.-W. He, W.-Y. Li, Y.-H. Li *et al.*, "Synthesis of Water-Dispersible Mn2+ Functionalized Silicon Nanoparticles under Room Temperature and Atmospheric Pressure for Fluorescence and Magnetic Resonance Dual-Modality Imaging," *Analytical Chemistry*, vol. 89, no. 21, pp. 11 286–11 292, **2017**. doi:10.1021/acs.analchem.7b01644

[4] J. Rodrigues, C. Becker, N. Ben Sedrine, M. Kamp, L. Kienle *et al.*, "Luminescent silver nanoclusters decorated on ZnO tetrapods: a detailed understanding of their role in photoluminescence features," *J. Mater. Chem. C*, vol. 9, pp. 7014–7026, **2021**. doi:10.1039/D1TC00099C

[5] I. Chakraborty and T. Pradeep, "Atomically Precise Clusters of Noble Metals: Emerging Link between Atoms and Nanoparticles," *Chemical Reviews*, vol. 117, no. 12, pp. 8208–8271, **2017**. doi:10.1021/acs.chemrev.6b00769

[6] Y. Du, H. Sheng, D. Astruc, and M. Zhu, "Atomically Precise Noble Metal Nanoclusters as Efficient Catalysts: A Bridge between Structure and Properties," *Chemical Reviews*, vol. 120, no. 2, pp. 526–622, **2020**. doi:10.1021/acs.chemrev.8b00726

[7] Y. Zeng, S. Havenridge, M. Gharib, A. Baksi, K. L. D. M. Weerawardene *et al.*, "Impact of Ligands on Structural and Optical Properties of Ag29 Nanoclusters," *Journal of the American Chemical Society*, vol. 143, no. 25, pp. 9405–9414, **2021**. doi:10.1021/jacs.1c01799

[8] Y. Wang and T. Bürgi, "Ligand exchange reactions on thiolate-protected gold nanoclusters," *Nanoscale Adv.*, vol. 3, pp. 2710–2727, **2021**. [Online]. Available: http://dx.doi.org/10.1039/D1NA00178G. doi:10.1039/D1NA00178G

[9] L. Zhu, M. Gharib, C. Becker, Y. Zeng, A. R. Ziefuß *et al.*, "Synthesis of Fluorescent Silver Nanoclusters: Introducing Bottom-Up and Top-Down Approaches to Nanochemistry in a Single Laboratory Class," *Journal of Chemical Education*, vol. 97, no. 1, pp. 239–243, **2020**. doi:10.1021/acs.jchemed.9b00342

[10] C. Xu, Q. Yuan, X. Wei, H. Li, H. Shen *et al.*, "Surface environment complication makes Ag29 nanoclusters more robust and leads to their unique packing in the supracrystal lattice," *Chem. Sci.*, vol. 13, pp. 1382–1389, **2022**. doi:10.1039/D1SC06002C

[11] M. van der Linden, A. J. van Bunningen, M. U. Delgado-Jaime, B. Detlefs, P. Glatzel *et al.*, "Insights into the Synthesis Mechanism of Ag29 Nanoclusters," *The Journal of Physical Chemistry C*, vol. 122, no. 49, pp. 28 351–28 361, **2018**. doi:10.1021/acs.jpcc.8b09360

[12] J. Yang and R. Jin, "New Advances in Atomically Precise Silver Nanoclusters," *ACS Materials Letters*, vol. 1, no. 4, pp. 482–489, **2019**. doi:10.1021/acsmaterialslett.9b00246

[13] A. Desireddy, B. E. Conn, J. Guo, B. Yoon, R. N. Barnett *et al.*, "Ultrastable silver nanoparticles," *Nature*, vol. 501, no. 7467, pp. 399–402, **2013**. doi:10.1038/nature12523

[14] H. Yang, Y. Wang, H. Huang, L. Gell, L. Lehtovaara *et al.*, "All-thiol-stabilized Ag44 and Au12Ag32 nanoparticles with single-crystal structures," *Nature Comunications*, vol. 4, no. 2422, pp. 1–8, **2013**. doi:10.1038/ncomms3422

[15] C. P. Joshi, M. S. Bootharaju, M. J. Alhilaly, and O. M. Bakr, "Ag25(SR)18 : The "Golden" Silver Nanoparticle," *Journal of the American Chemical Society*, vol. 137, no. 36, pp. 11 578–11 581, **2015**. doi:10.1021/jacs.5b07088

[16] W. Ishii, Y. Okayasu, Y. Kobayashi, R. Tanaka, S. Katao *et al.*, "Excited State Engineering in Ag29 Nanocluster through Peripheral Modification with Silver(I) Complexes for Bright Near-Infrared Photoluminescence," *Journal of the American Chemical Society*, vol. 145, no. 20, pp. 11 236–11 244, **2023**. doi:10.1021/jacs.3c01259

[17] G.-G. Luo, Q.-L. Guo, Z. Wang, C.-F. Sun, J.-Q. Lin *et al.*, "New protective

ligands for atomically precise silver nanoclusters," *Dalton Trans.*, vol. 49, pp. 5406–5415, **2020**. doi:10.1039/D0DT00477D

[18] S. Maity, D. Bain, and A. Patra, "Engineering atomically precise copper nanoclusters with aggregation induced emission," *The Journal of Physical Chemistry C*, vol. 123, no. 4, pp. 2506–2515, **2019**. doi:10.1021/acs.jpcc.8b09467

[19] Y. Zhang, Z. Lu, A. Feng, J. W. Y. Lam, Z. Wang *et al.*, "Green-Emissive Copper Nanocluster with Aggregation-Enhanced Emission for Selective Detection of Al3+," *Chemistry – A European Journal*, vol. 29, no. 13, p. e202203554, **2023**. doi:https://doi.org/10.1002/chem.202203554

[20] C.-J. Yu, T.-H. Chen, J.-Y. Jiang, and W.-L. Tseng, "Lysozyme-directed synthesis of platinum nanoclusters as a mimic oxidase," *Nanoscale*, vol. 6, pp. 9618–9624, **2014**. doi:10.1039/C3NR06896J

[21] Le Guével, Xavier and Trouillet, Vanessa and Spies, Christian and Jung, Gregor and Schneider, Marc, "Synthesis of yellow-emitting platinum nanoclusters by ligand etching," *The Journal of Physical Chemistry C*, vol. 116, no. 10, pp. 6047–6051, **2012**. doi:10.1021/jp211672t

[22] S. K. Eswaramoorthy and A. Dass, "Atomically precise palladium nanoclusters with 21 and 38 pd atoms protected by phenylethanethiol," *The Journal of Physical Chemistry C*, vol. 126, no. 1, pp. 444–450, **2022**. doi:10.1021/acs.jpcc.1c09453

[23] X. Kang, Y. Li, M. Zhu, and R. Jin, "Atomically precise alloy nanoclusters: syntheses, structures, and properties," *Chem. Soc. Rev.*, vol. 49, pp. 6443–6514, **2020**. doi:10.1039/C9CS00633H

[24] Z. Wu and R. Jin, "On the ligand's role in the fluorescence of gold nanoclusters," *Nano letters*, vol. 10, pp. 2568–2573, **2010**. doi:10.1021/nl101225f

[25] E. S. Shibu, M. A. H. Muhammed, T. Tsukuda, and T. Pradeep, "Ligand Exchange of Au25SG18 Leading to Functionalized Gold Clusters: Spectroscopy, Kinetics, and Luminescence," *The Journal of Physical Chemistry C*, vol. 112, no. 32, pp. 12 168–12 176, **2008**. doi:10.1021/jp800508d

[26] E. S. Shibu and T. Pradeep, "Photoluminescence and Temperature-Dependent Emission Studies of Au25 Clusters In the Solid State," *International Journal of Nanoscience*, vol. 08, no. 01n02, pp. 223–226, **2009**. doi:10.1142/S0219581X09005669

[27] S. Wang, X. Zhu, T. Cao, and M. Zhu, "A simple model for understanding the

fluorescence behavior of Au25 nanoclusters," *Nanoscale*, vol. 6, pp. 5777–5781, **2014**. doi:10.1039/C3NR06722J

[28] X.-Y. Xie, P. Xiao, X. Cao, W.-H. Fang, G. Cui *et al.*, "The origin of the photoluminescence enhancement of gold-doped silver nanoclusters: The importance of relativistic effects and heteronuclear gold–silver bonds," *Angewandte Chemie International Edition*, vol. 57, no. 31, pp. 9965–9969, **2018**. doi:https://doi.org/10.1002/anie.201803683

[29] S. Yang and M. Zhu, "Insight of the photoluminescence of atomically precise bimetallic nanoclusters with free electrons," *Journal of the Chinese Chemical Society*, vol. 67, no. 12, pp. 2171–2181, **2020**. doi:https://doi.org/10.1002/jccs.202000090

[30] Y. Shichibu, Y. Negishi, T. Watanabe, N. K. Chaki, H. Kawaguchi *et al.*, "Biicosahedral Gold Clusters [Au25(PPh3)10(SCnH2n+1)5Cl2]2+ (n = 218): A Stepping Stone to Cluster-Assembled Materials," *The Journal of Physical Chemistry C*, vol. 111, no. 22, pp. 7845–7847, **2007**. doi:10.1021/jp073101t

[31] X. Kang and M. Zhu, "Tailoring the photoluminescence of atomically precise nanoclusters," *Chem. Soc. Rev.*, vol. 48, pp. 2422–2457, **2019**. doi:10.1039/C8CS00800K

[32] J. T. van Wijngaarden, O. Toikkanen, P. Liljeroth, B. M. Quinn, and A. Meijerink, "Temperature-Dependent Emission of Monolayer-Protected Au38 Clusters," *The Journal of Physical Chemistry C*, vol. 114, no. 38, pp. 16 025–16 028, **2010**. doi:10.1021/jp1018372

[33] J. Yang and R. Jin, "Advances in Enhancing Luminescence of Atomically Precise Ag Nanoclusters," *The Journal of Physical Chemistry C*, vol. 125, no. 4, pp. 2619–2625, **2021**. doi:10.1021/acs.jpcc.0c08693

[34] Y. Mishra, S. Kaps, A. Schuchardt, I. Paulowicz, X. Jin *et al.*, "Fabrication of Macroscopically Flexible and Highly Porous 3D Semiconductor Networks from Interpenetrating Nanostructures by a Simple Flame Transport Approach," *Particle & Particle Systems Characterization*, vol. 30, no. 9, pp. 775–783, **2013**. doi:https://doi.org/10.1002/ppsc.201300197

[35] I. Paulowicz, V. Postica, O. Lupan, N. Wolff, S. Shree *et al.*, "Zinc oxide nanotetrapods with four different arm morphologies for versatile nanosensors," *Sensors and Actuators B: Chemical*, vol. 262, pp. 425–435, **2018**. doi:https://doi.org/10.1016/j.snb.2018.01.206

[36] J. Rodrigues, D. Smazna, N. Ben Sedrine, E. Nogales, R. Adelung *et al.*, "Probing surface states in C60 decorated ZnO microwires: detailed photoluminescence and cathodoluminescence investigations," *Nanoscale Adv.*, vol. 1, pp. 1516–1526, **2019**. doi:10.1039/C8NA00296G

[37] D. Smazna, J. Rodrigues, S. Shree, V. Postica, G. Neubüser *et al.*, "Buckminsterfullerene hybridized zinc oxide tetrapods: defects and charge transfer induced optical and electrical response," *Nanoscale*, vol. 10, pp. 10 050–10 062, **2018**. doi:10.1039/C8NR01504J

[38] R. M. Clegg, "Chapter 1 Förster resonance energy transfer — FRET what is it, why do it, and how it's done, Laboratory Techniques in Biochemistry and Molecular Biology," *Laboratory Techniques in Biochemistry and Molecular Biology*, vol. 33, pp. 1–57, **2009**. doi:10.1016/S0075-7535(08)00001-6

[39] E. Sobakinskaya, M. Schmidt am Busch, and T. Renger, "Theory of FRET "Spectroscopic Ruler" for Short Distances: Application to Polyproline," *The Journal of Physical Chemistry B*, vol. 122, no. 1, pp. 54–67, **2018**. doi:10.1021/acs.jpcb.7b09535

[40] B. Schuler, E. Lipmann, P. Steinbach, and W. Eaton, "Polyproline and the "spectroscopic ruler" revisited with single-molecule fluorescence," *PNAS*, vol. 102, pp. 2754–2759, **2005**. doi:10.1073/pnas.0408164102

[41] B. Valeur and M. Berberan-Santos, Eds., *Molecular Fluorescence.* Wiley-VCH, 2012.

[42] D. Bain, B. Paramanik, and A. Patra, "Silver(I)-Induced Conformation Change of DNA Gold Nanocluster as a Spectroscopic Probe," *The Journal of Physical Chemistry C*, vol. 121, pp. 4608–4617, **2017**. doi:10.1021/acs.jpcc.6b10560

[43] S. Hamd-Ghadareh and Salimi, "DNA-functionalized dye-loaded carbon dots ultrabright FRET platform for ratiometric detection of Hg(II) in serum samples and cell microenvironment," *Ionics*, vol. 25, pp. 4469–4479, **2019**. doi:10.1007/s11581-019-02999-2

[44] I. M. Khan, S. Niazi, Y. Yu, A. Mohsin, B. S. Mushtaq *et al.*, "Aptamer Induced Multicolored AuNCs-WS2 "Turn on" FRET Nano Platform for Dual-Color Simultaneous Detection of AflatoxinB1 and Zearalenone," *Analytical Chemistry*, vol. 91, no. 21, pp. 14 085–14 092, **2019**. doi:10.1021/acs.analchem.9b03880

[45] K. Mondal, A. Pramanik, T. Mondal, S. S. Panja, R. Sarkar *et al.*, "Self-

Assembly of Solvent-Stabilized Au Nanocluster as Efficient Förster Resonance Energy-Transfer Initiator for White Light Generation," *The Journal of Physical Chemistry Letters*, vol. 13, no. 13, pp. 3079–3088, **2022**. doi:10.1021/acs.jpclett.1c04228

[46] A. Chatterjee, A. K. Sharma, S. Pramanick, O. S. Jaykishan, and P. Purkayastha, "Dual Stimuli-Responsive BSA-Protected Silver Nanocluster-Driven "FRET On–Off" within the Niosomal Membrane: An Amalgamation of Restoration of Aggregation-Induced Quenched Fluorescence and Energy Transfer," *The Journal of Physical Chemistry C*, vol. 127, no. 1, pp. 797–806, **2023**. doi:10.1021/acs.jpcc.2c07525

[47] C. Becker, S. Graf, A. Mews, W. J. Parak, and I. Chakraborty, "Effect of hybridization on the photoluminescence properties of atomically precise silver nanocluster," **2023**, submitted.

[48] M. van der Linden, A. Barendregt, A. J. van Bunningen, P. T. K. Chin, D. Thies-Weesie *et al.*, "Characterisation, degradation and regeneration of luminescent Ag29 clusters in solution," *Nanoscale*, vol. 8, pp. 19 901–19 909, **2016**. doi:10.1039/C6NR04958C

[49] Søren Preus, "Calculate Resonance Energy Transfer (FRET) Efficiencies," **2019**, www.fluortools.com/software/ae/documentation/tools/FRET, last accessed Feb 16, 2019.

[50] L. Manna, D. J. Milliron, A. Meisel, E. C. Scher, and A. P. Alivisatos, "Controlled growth of tetrapod-branched inorganic nanocrystals," *Nature Materials*, vol. 2, no. 6, pp. 382–385, **2003**. doi:10.1038/nmat902

[51] G. Modi, "Zinc oxide tetrapod: a morphology with multifunctional applications," *Advances in Natural Sciences: Nanoscience and Nanotechnology*, vol. 6, no. 3, p. 033002, apr **2015**. doi:10.1088/2043-6262/6/3/033002

[52] M. Shiojiri and C. Kaito, "Structure and growth of ZnO smoke particles prepared by gas evaporation technique," *Journal of Crystal Growth*, vol. 52, pp. 170–177, **1981**.

[53] Y. Dai, Y. Zhang, and Z. L. Wang, "The octa-twin tetraleg ZnO nanostructures," *Solid State Communications*, vol. 126, pp. 629–633, **2003**.

[54] M. Fujii, H. Iwanaga, and M. S. Ichihara Takeuch, "Structure of tetrapod-like ZnO crystals," *Journal of Crystal Growth*, vol. 128, pp. 1095–1098, **1993**.

[55] H. Iwanaga and M. S. Fujii Takeuch, "Structure of tetrapod-like ZnO crystals," *Journal of Crystal Growth*, vol. 134, pp. 275–280, **1993**.

[56] Y. K. Mishra and R. Adelung, "ZnO tetrapod materials for functional applications," *Materials Today*, vol. 21, no. 6, pp. 631–651, **2018**. doi:https://doi.org/10.1016/j.mattod.2017.11.003

[57] D. Mora-Fonz, T. Lazauskas, M. R. Farrow, C. R. A. Catlow, S. M. Woodley *et al.*, "Why Are Polar Surfaces of ZnO Stable?" *Chemistry of Materials*, vol. 29, no. 12, pp. 5306–5320, **2017**. doi:10.1021/acs.chemmater.7b01487

[58] D. Liu, W. Wu, Y. Qiu, S. Yang, S. Xiao *et al.*, "Surface Functionalization of ZnO Nanotetrapods with Photoactive and Electroactive Organic Monolayers," *Langmuir*, vol. 24, no. 9, pp. 5052–5059, **2008**. doi:10.1021/la800074f

[59] P. W. Sadik, S. J. Pearton, D. P. Norton, E. Lambers, and F. Ren, "Functionalizing Zn- and O-terminated ZnO with thiols," *Journal of Applied Physics*, vol. 101, no. 10, 05 **2007**. doi:10.1063/1.2736893

[60] J. E. Whitten, "Surface Chemistry of Metal Oxide Nanoparticles and Attachement of Metal Nanoclusters Sensor, Optoelectronic and Photocatalytic Applications," *TechConnect Briefs*, **2015**.

[61] T. Santhaveesuk, D. Wongratanaphisan, and S. Choopun, "Enhancement of sensor response by TiO2 mixing and Au coating on ZnO tetrapod sensor," *Sensors and Actuators B: Chemical*, vol. 147, no. 2, pp. 502–507, **2010**. [Online]. Available: https://www.sciencedirect.com/science/article/pii/S0925400510003072. doi:https://doi.org/10.1016/j.snb.2010.03.081

[62] J. Gröttrup, V. Postica, N. Ababii, O. Lupan, C. Zamponi *et al.*, "Size-dependent UV and gas sensing response of individual Fe2O3-ZnO:Fe micro- and nanowire based devices," *Journal of Alloys and Compounds*, vol. 701, pp. 920–925, **2017**. doi:https://doi.org/10.1016/j.jallcom.2016.12.346

[63] O. Lupan, V. Postica, J. Gröttrup, A. K. Mishra, N. H. de Leeuw *et al.*, "Hybridization of Zinc Oxide Tetrapods for Selective Gas Sensing Applications," *ACS Applied Materials & Interfaces*, vol. 9, no. 4, pp. 4084–4099, **2017**, pMID: 28111948. doi:10.1021/acsami.6b11337

[64] V. Postica, J. Gröttrup, R. Adelung, O. Lupan, A. K. Mishra *et al.*, "Multifunctional Materials: A Case Study of the Effects of Metal Doping on ZnO Tetrapods with Bismuth and Tin Oxides," *Advanced Functional Materials*, vol. 27, no. 6,

p. 1604676, **2017**. doi:https://doi.org/10.1002/adfm.201604676

[65] Y. Song, X. Zhang, X. Yan, Q. Liao, Z. Wang *et al.*, "An enzymatic biosensor based on three-dimensional ZnO nanotetrapods spatial net modified AlGaAs/GaAs high electron mobility transistors," *Applied Physics Letters*, vol. 105, no. 21, 11 **2014**. doi:10.1063/1.4902944

[66] M. Kaur, K. Ganapathi, V. Mukund, C. Jain, N. S. Ramgir *et al.*, "Selective H2S detection by CuO functionalized ZnO nanotetrapods at room temperature," *Materials Chemistry and Physics*, vol. 143, no. 3, pp. 1319–1324, **2014**. doi:https://doi.org/10.1016/j.matchemphys.2013.11.041

[67] C. De Zorzi, G. Rossetto, D. Calestani, M. Z. Zha, A. Zappettini *et al.*, "Pd/PdO functionalization of SnO2 nanowires and ZnO nanotetrapods," *Crystal Research and Technology*, vol. 46, no. 8, pp. 847–851, **2011**. doi:https://doi.org/10.1002/crat.201000650

[68] X. Zhou, R. Peng, C. Ren, L. Sun, J. Hu *et al.*, "Fabrication and field emission properties of ZnO/Al2O3 nanocomposite tetrapods," *Journal of Alloys and Compounds*, vol. 695, pp. 1863–1869, **2017**. doi:https://doi.org/10.1016/j.jallcom.2016.11.020

[69] M. Y. Guo, A. M. C. Ng, F. Liu, A. B. Djurišić, W. K. Chan *et al.*, "Effect of Native Defects on Photocatalytic Properties of ZnO," *The Journal of Physical Chemistry C*, vol. 115, no. 22, pp. 11 095–11 101, **2011**. doi:10.1021/jp200926u

[70] W. M. Kwok, A. B. Djurišić, Y. H. Leung, W. K. Chan, and D. L. Phillips, "Time-resolved photoluminescence from ZnO nanostructures," *Applied Physics Letters*, vol. 87, no. 22, p. 223111, 11 **2005**. doi:10.1063/1.2137456

7 Appendix

7.1 FRET exhibiting Ag nanocluster hybrid structure

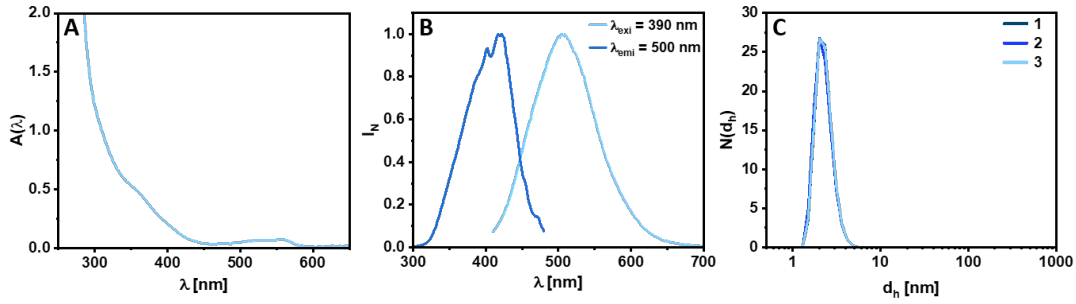

Figure 7.1: UV-vis absorption spectrum (A), photoluminescence emission and excitation spectra measured for λ_{ex}=390 nm and λ_{em}=500 nm respectively and hydrodynamic diameter in terms of number distribution N(d_h) (C). Publication submitted.

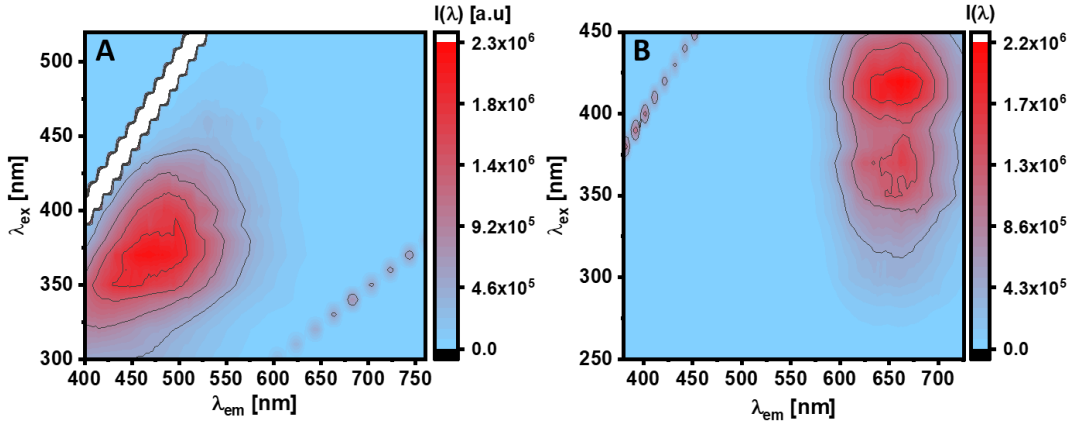

Figure 7.2: 2D PL spectra for Si NCs (A) and Ag_{29} NCs (B). Publication submitted.

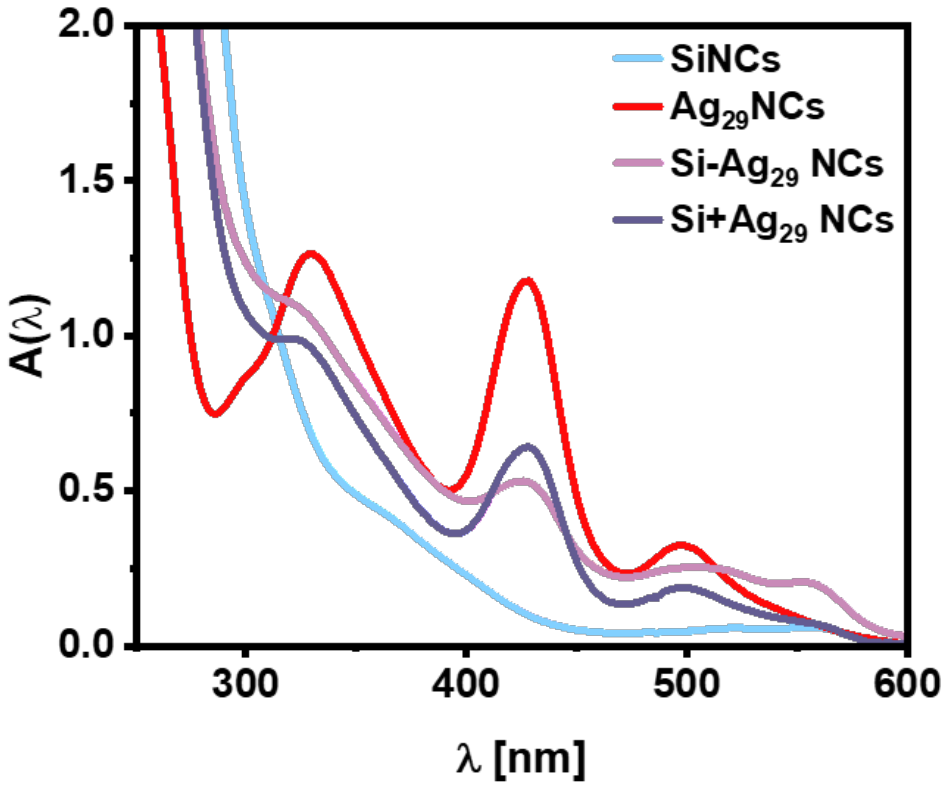

Figure 7.3: Absorbance spectra of Si NCs (bright blue), Ag_{29} NCs (red), Si-Ag_{29} NCs (light purple), and Si NCs + Ag_{29} NCs (dark purple). Publication submitted.

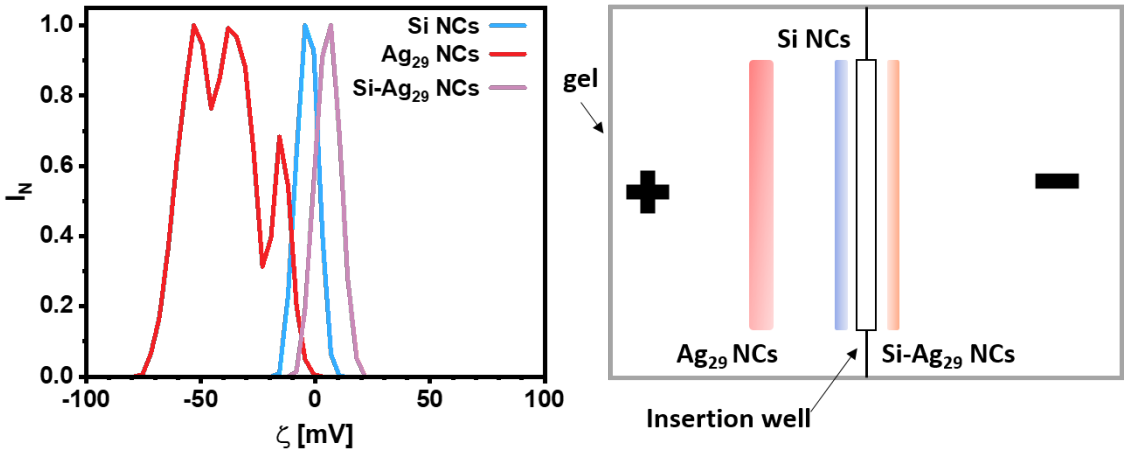

Figure 7.4: Zeta potential ζ of Si NCs (bright blue), Ag_{29} NCs (red), and Si-Ag_{29} NCs (left) and the schematic prediction for their appearance in an agarose gel after gel electrophoresis based on the zeta potential results (right). Publication submitted.

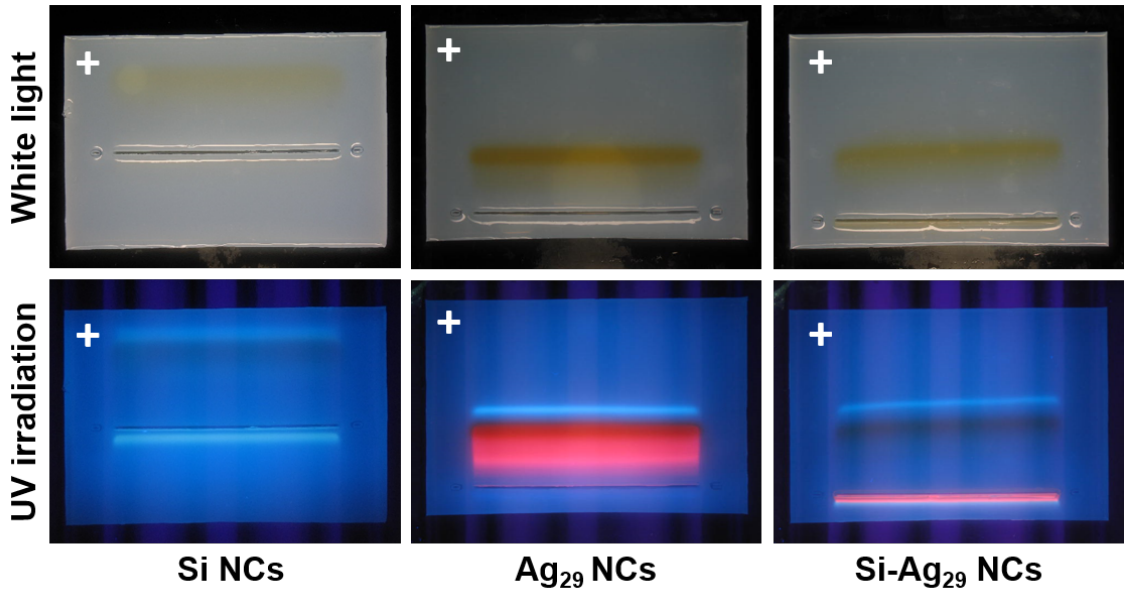

Figure 7.5: Pictures of agarose gels under white and UV light for the samples Si NCs, Ag_{29} NCs, and Si-Ag_{29} NCs after gel electrophoresis (left to right). Plus indicates the side of the anode. Publication submitted.

Table 7.1: FTIR wavenumber values in cm-1 from FTIR spectra of Si-Ag_{29} NCs and Ag_{29} NCs assigned to their characteristic vibrations and bends. Publication submitted.

	$\nu_{N-H\ stretch}$	$\nu_{Bonded\ >NH\ stretch\ (Amide)}$	$\nu_{-CH2\ stretch}$	$\nu_{Amide\ II\ bond}$	
	3352	3283	2930 2875	1631	
Si-Ag_{29} NCs	$\nu_{-N-H\ bend\ (Amine)}$	$\nu_{-N-H\ bend\ (Amide)}$	$\nu_{>CH2\ scissor}$	$\nu_{Si-O\ stretch}$	
	1571	1488	1333	1110 1026	
	$\nu_{O-H\ stretch}$	$\nu_{-CH2\ stretch}$	$\nu_{COOH\ stretch}$	$\nu_{>CH2\ scissor}$	$\nu_{C-H\ bend}$
Ag_{29} NCs	3385	2934	1649 1565	1406 1347	972

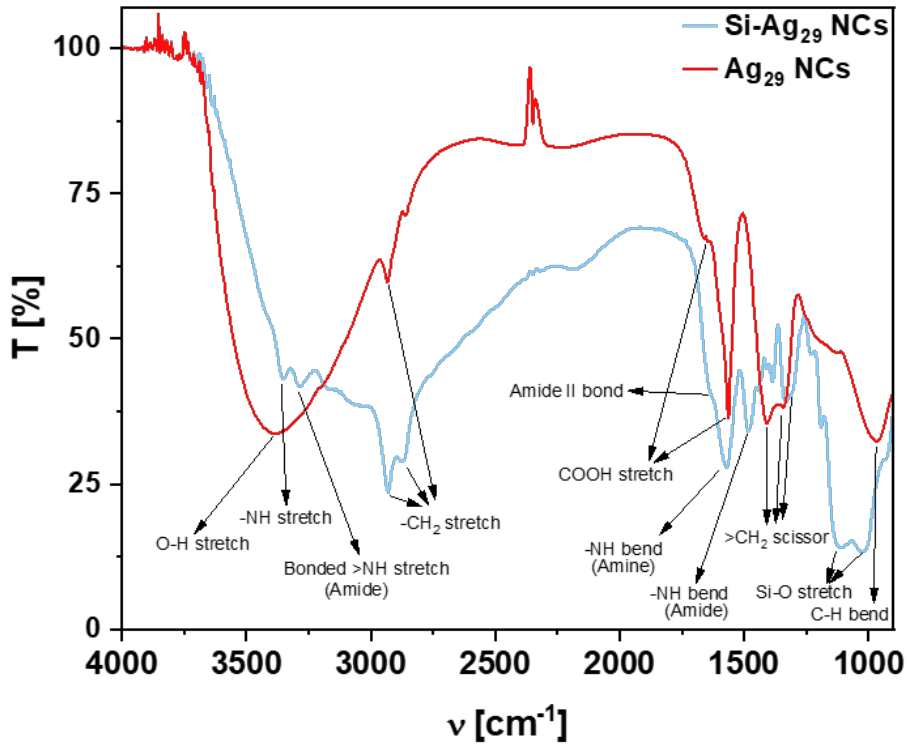

Figure 7.6: FTIR transmission spectra of Si-Ag_{29} NCs and Ag_{29} NCs with indicated characteristic group vibrations and bends. Publication submitted.

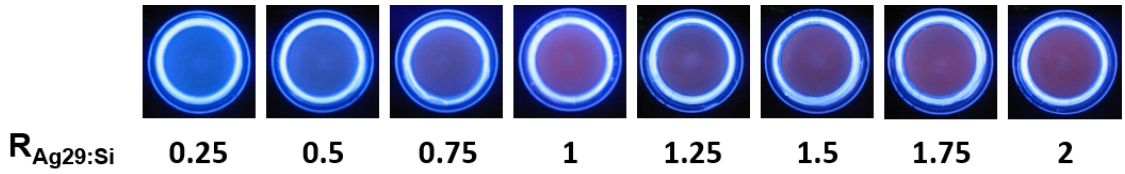

Figure 7.7: Photographs of Si NCs and Ag_{29} NCs in combination at ratios 0.25-2 similarly to Si-Ag_{29} NCs under UV irradiation. Publication submitted.

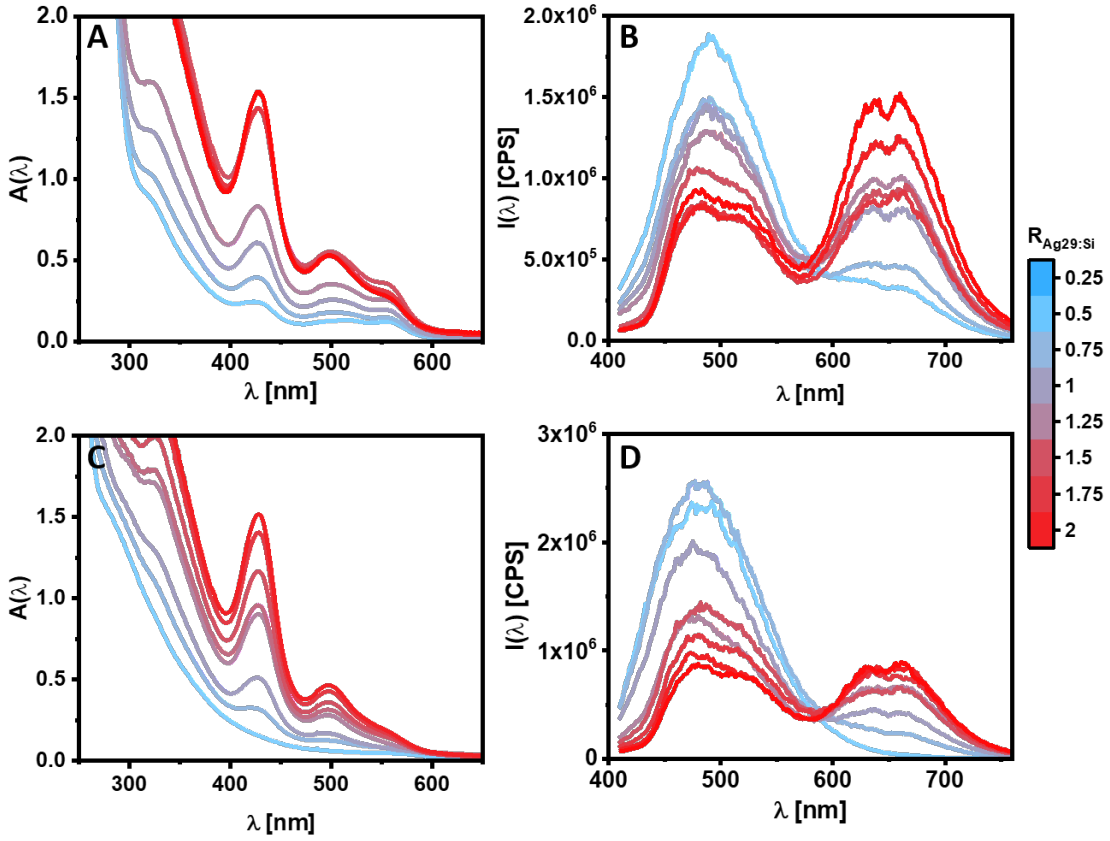

Figure 7.8: Absorbance and photoluminescence of the hybrid system Si-Ag_{29} NCs (A+B) and the uncoupled combination of Si NCs and Ag_{29} NCs (C+B) at ratios 0.25-2. Publication submitted.

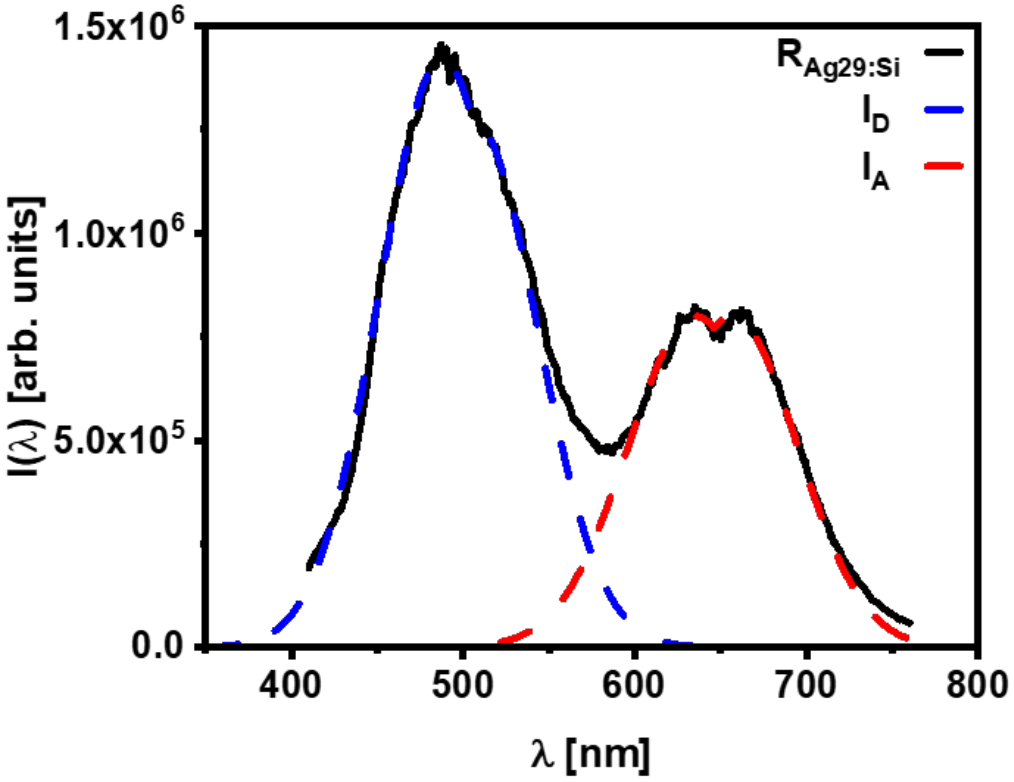

Figure 7.9: Example of fitting the characteristic peaks of the donor (D) Si NCs and the acceptor (A) Ag_{29} NCs in the hybrid system (left) and the uncoupled mixture (right). Here shown on the graphs at a ratio of 0.75 before isolation and leakage correction. Publication submitted.

Table 7.2: FRET efficiency values (η_{ET}) for the hybrid structure Si-Ag_{29} NCs and the uncoupled combination of Si NCs and Ag_{29} NCs for ratios $R_{Ag_{29}:Si} = 0.25-2$ complemented with the AUC values for the donor ID and the acceptor IA Publication submitted.

		Si-Ag_{29} NCs			Si+Ag_{29} NCs		
Sample	**$R_{Ag29:Si}$**	**I_D**	**I_A**	**$E_{rel.}$**	**I_D**	**I_A**	**$E_{rel.}$**
1	**0.25**	1.97 10^8	4.08 10^8	*0.17*	2.69 10^8	2.83 10^6	*0.01*
2	**0.5**	1.50 10^8	5.61 10^7	*0.27*	2.88 10^8	2.00 10^7	*0.06*
3	**0.75**	1.43 10^8	8.95 10^7	*0.38*	2.08 10^8	4.68 10^7	*0.18*
4	**1**	1.28 10^8	1.08 10^8	*0.46*	1.34 10^8	7.42 10^7	*0.36*
5	**1.25**	1.03 10^8	1.02 10^8	*0.50*	1.47 10^8	6.89 10^7	*0.32*
6	**1.5**	8.59 10^7	9.60 10^7	*0.53*	1.19 10^8	8.42 10^7	*0.41*
7	**1.75**	8.63 10^7	1.27 10^8	*0.59*	9.72 10^7	8.82 10^7	*0.48*
8	**2**	9.23 10^7	1.56 10^8	*0.63*	9.14 10^7	8.69 10^7	*0.49*

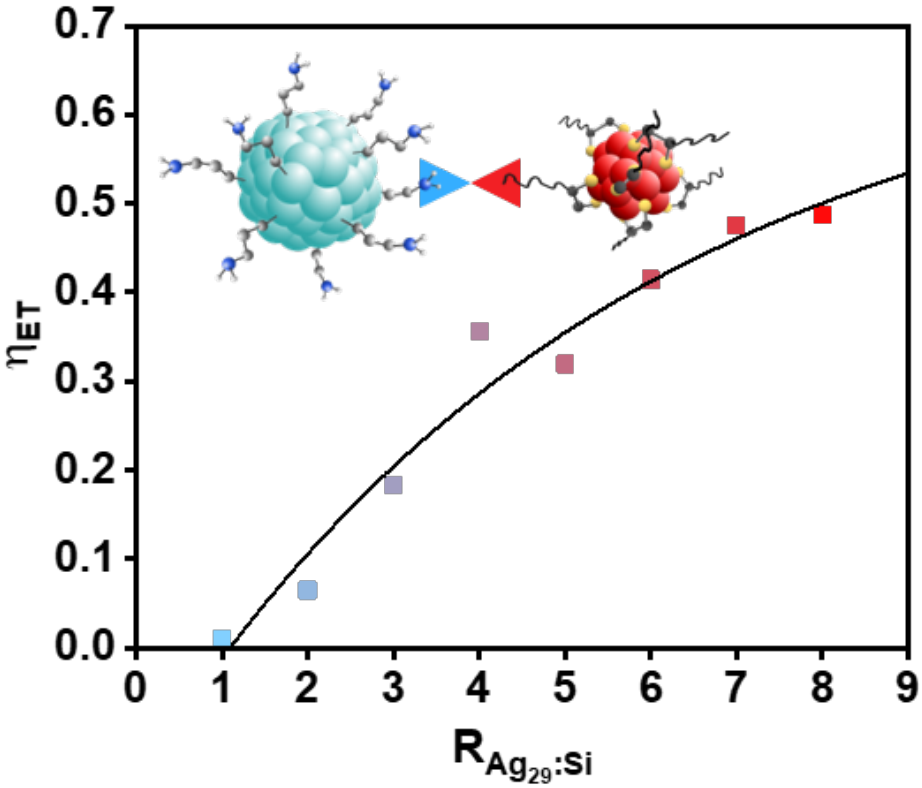

Figure 7.10: Fitted FRET efficiency values (η_{ET}) with scheme of the assembly form of the hybrid system in charge attracted only state. Publication submitted.

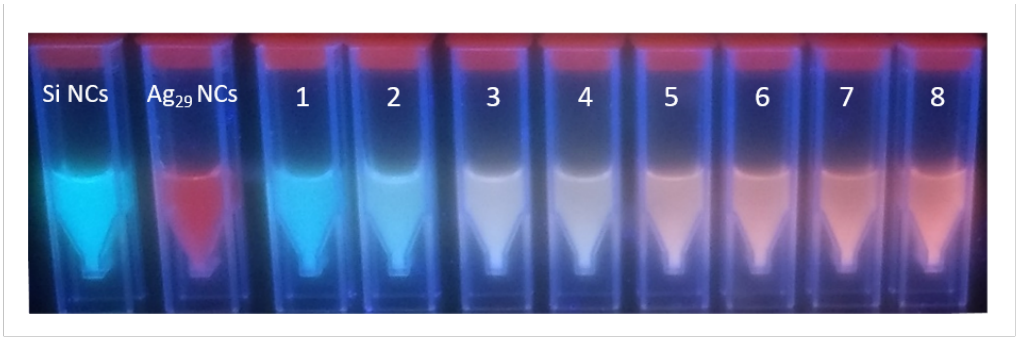

Sample	Si NCs	Ag_{29} NCs	1	2	3	4	5	6	7	8
$R_{Ag29:Si}$	0	1	0.25	0.5	0.75	1	1.25	1.5	1.75	2

Figure 7.11: Pictures of the samples of Si NCs, Ag_{29} NCs and Si-Ag_{29} NCs at ratios $R_{Ag_{29}:Si}$= $0.25 - 2$ for LT characterization under UV light. Publication submitted.

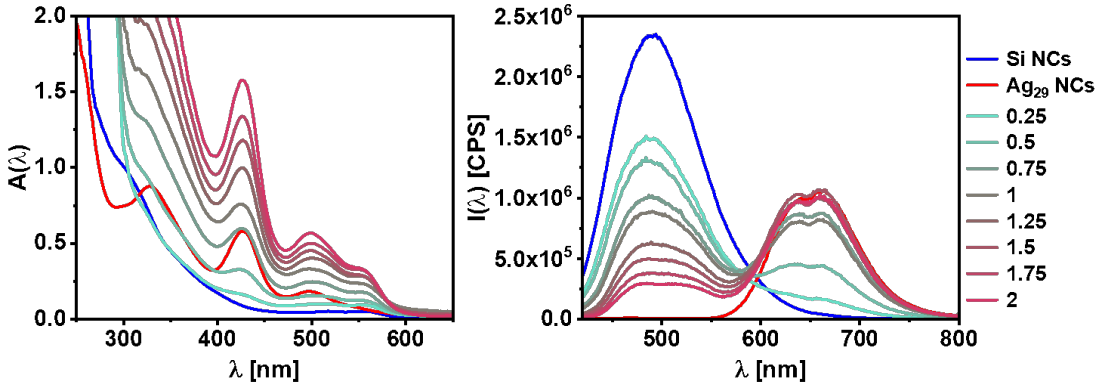

Figure 7.12: Absorbance and Photoluminescence spectra of samples Si NCs, Ag_{29} NCs and Si-Ag_{29} NCs at ratios $R_{Ag_{29}:Si} = 0.25 - 2$ for LT characterization. Publication submitted.

Table 7.3: LT values τ_{Ave} in ns of samples Si NCs and Si-Ag_{29} NCs at ratios $R_{Ag_{29}:Si} = 0.25 - 2$ for the excitation/emission wavelength combinations 405/490 and 405/650 Publication submitted.

	$R_{Ag_{29}:Si}$								
$\lambda_{exi}/\lambda_{emi}$	**0**	**0.25**	**0.5**	**0.75**	**1**	**1.25**	**1.5**	**1.75**	**2**
405/490	10.34 ± 0.03	8.90 ± 0.05	8.62 ± 0.03	8.24 ± 0.06	8.05 ± 0.06	7.63 ± 0.05	7.48 ± 0.05	6.87 ± 0.05	6.90 ± 0.1
405/650	6.93 ± 0.05	6.52 ± 0.14	9.84 ± 0.97	15.8 ± 5.4	18.6 ± 8.9	16.3 ± 3.3	34.3 ± 8.2	50 ± 68	53 ± 11

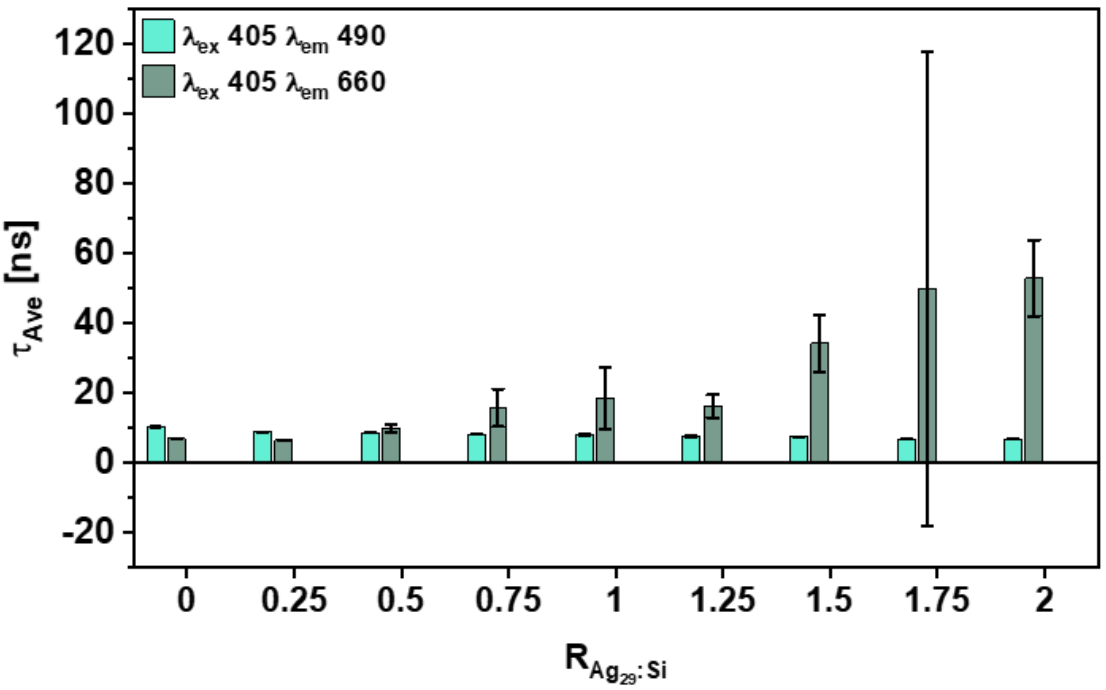

Figure 7.13: Graphic display of LT values τ_{Ave} of the Si-Ag_{29} NCs hybrid system at ratios $R_{Ag_{29}:Si} = 0 - 2$ under excitation at 405 nm and the emission detected at 490 nm and 650 nm. Publication submitted.

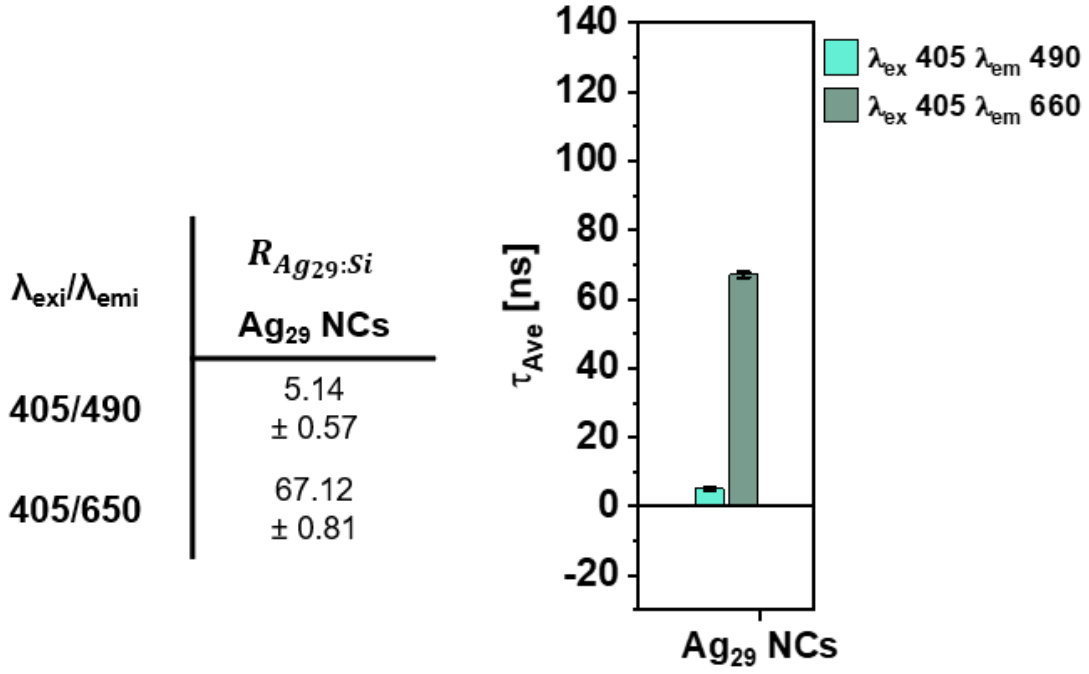

Figure 7.14: LT values τAve in ns of Ag_{29} NCs for the excitation/emission wavelength combinations 405/490 and 405/650 in nm and their graphical display. Publication submitted.

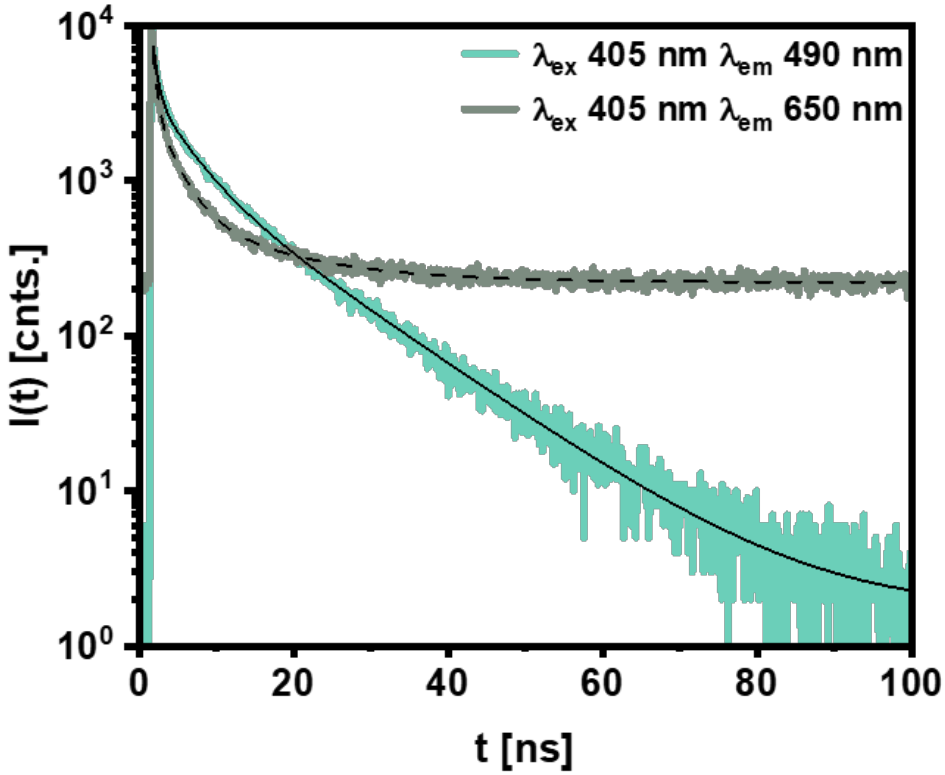

Figure 7.15: Fluorescence LT decay curves of Si-Ag_{29} NCs at ratio $R_{Ag_{29}:Si}$= 0.25 for the excitation/emission wavelength combinations 405/490 and 405/650. Publication submitted.

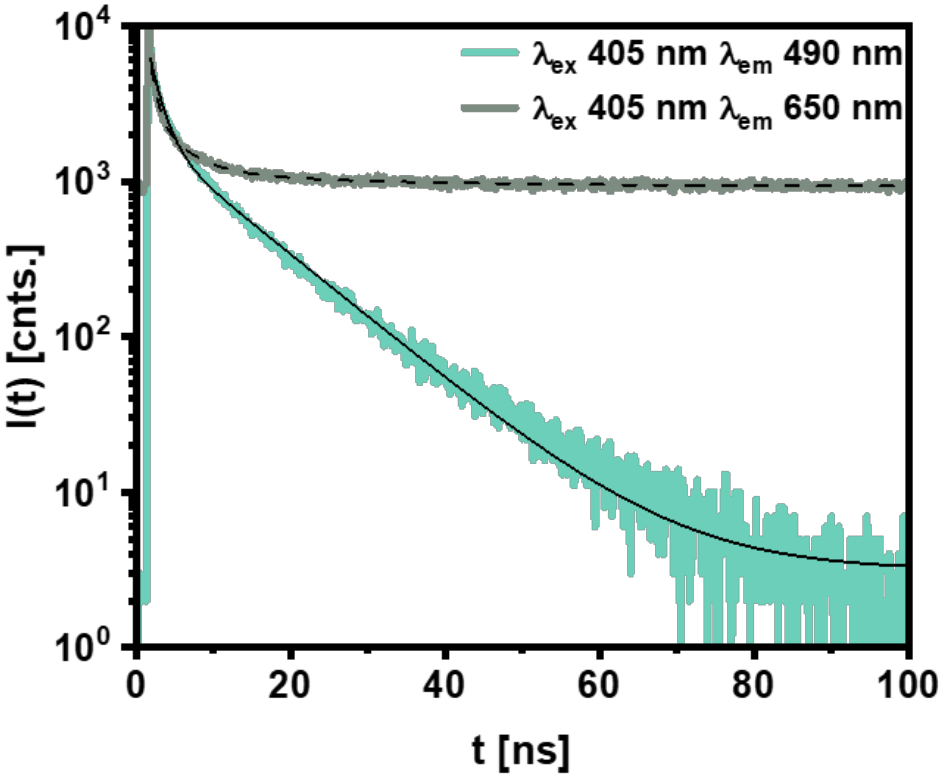

Figure 7.16: Fluorescence LT decay curves of Si-Ag_{29} NCs at ratio $R_{Ag_{29}:Si}$= 0.5 for the excitation/emission wavelength combinations 405/490 and 405/650. Publication submitted.

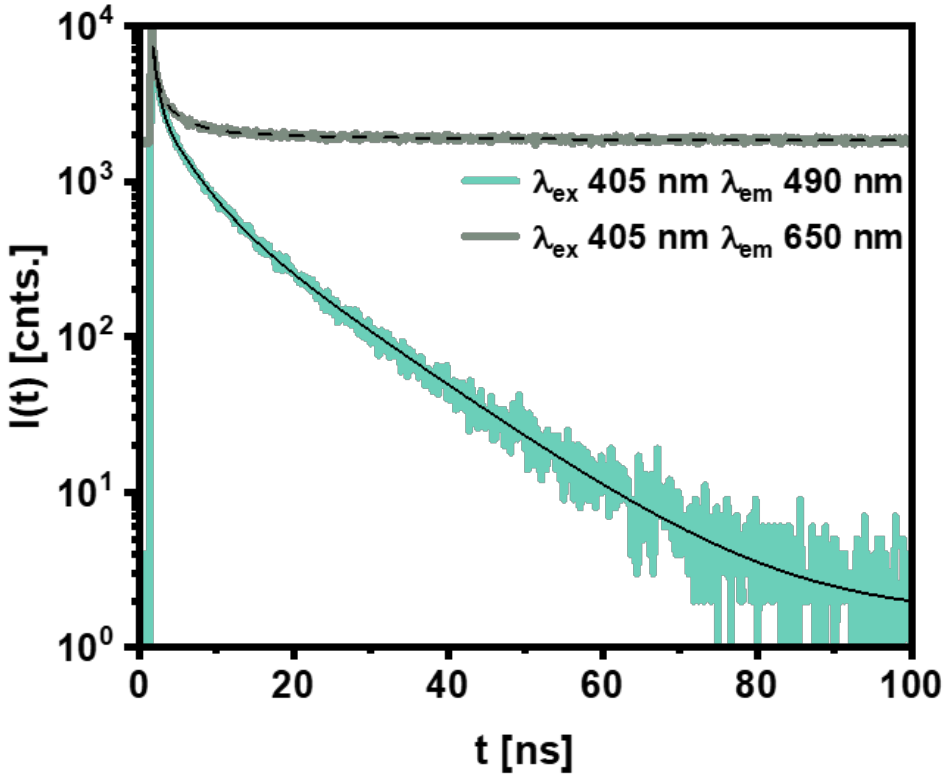

Figure 7.17: Fluorescence LT decay curves of Si-Ag_{29} NCs at ratio $R_{Ag_{29}:Si}$= 0.75 for the excitation/emission wavelength combinations 405/490 and 405/650. Publication submitted.

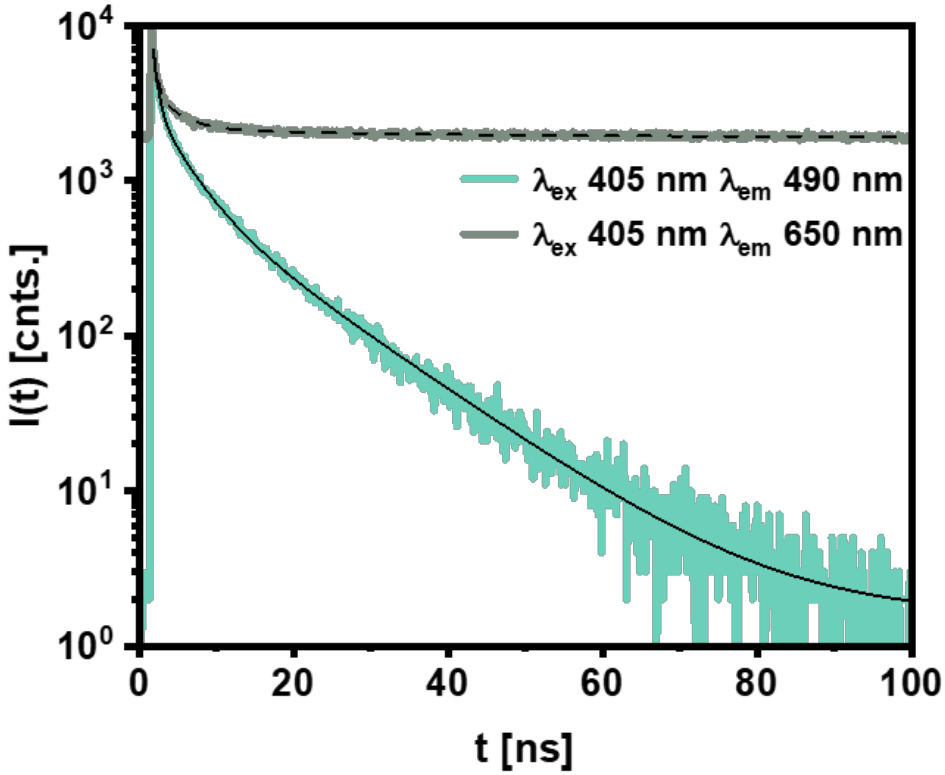

Figure 7.18: Fluorescence LT decay curves of Si-Ag_{29} NCs at ratio $R_{Ag_{29}:Si}$= 1 for the excitation/emission wavelength combinations 405/490 and 405/650. Publication submitted.

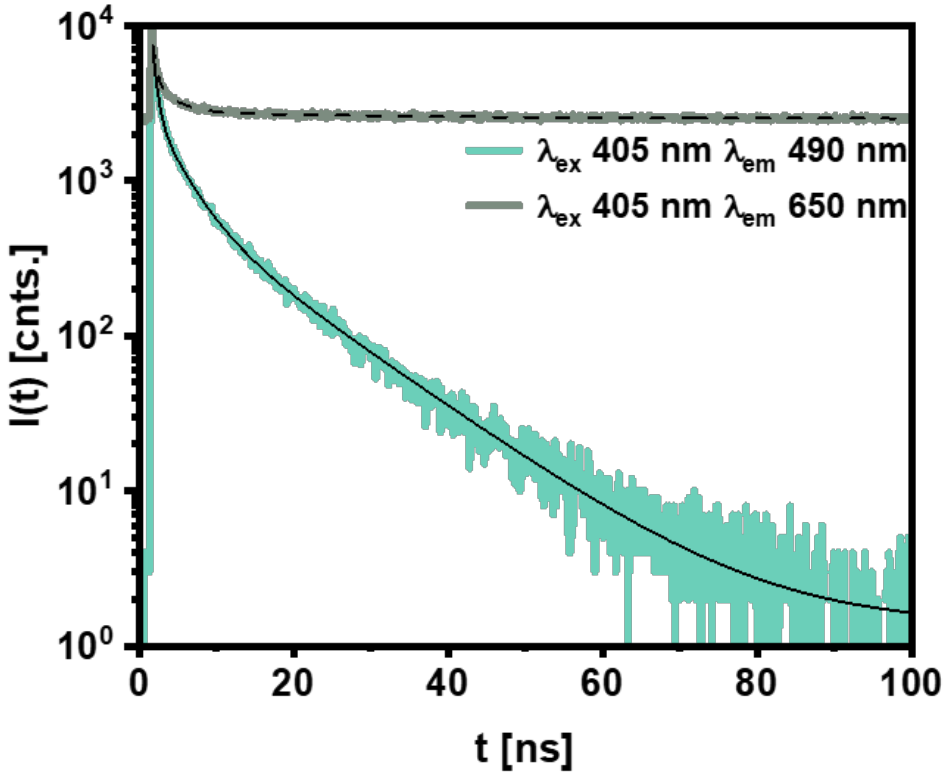

Figure 7.19: Fluorescence LT decay curves of Si-Ag_{29} NCs at ratio $R_{Ag_{29}:Si}$= 1.25 for the excitation/emission wavelength combinations 405/490 and 405/650. Publication submitted.

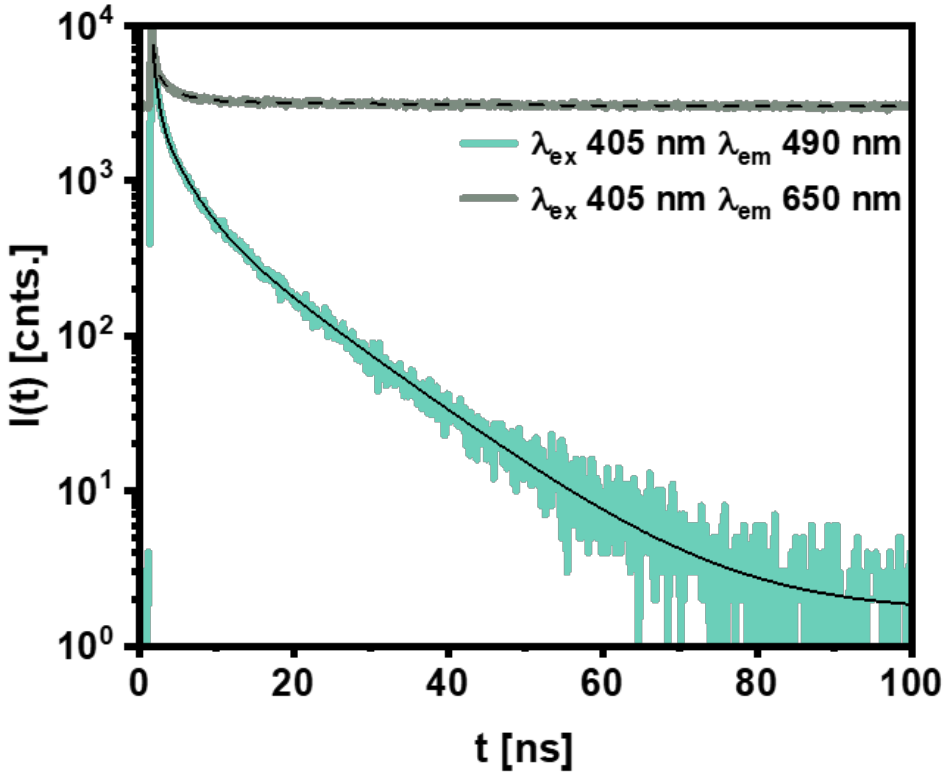

Figure 7.20: Fluorescence LT decay curves of Si-Ag_{29} NCs at ratio $R_{Ag_{29}:Si}$= 1.5 for the excitation/emission wavelength combinations 405/490 and 405/650. Publication submitted.

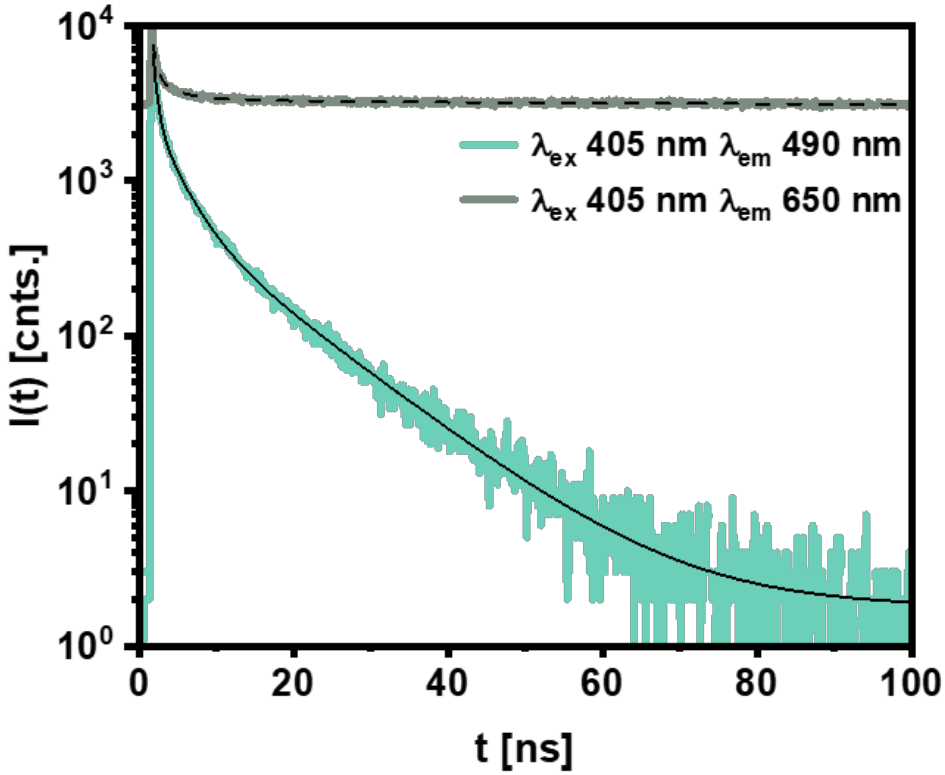

Figure 7.21: Fluorescence LT decay curves of Si-Ag_{29} NCs at ratio $R_{Ag_{29}:Si}$= 1.75 for the excitation/emission wavelength combinations 405/490 and 405/650. Publication submitted.

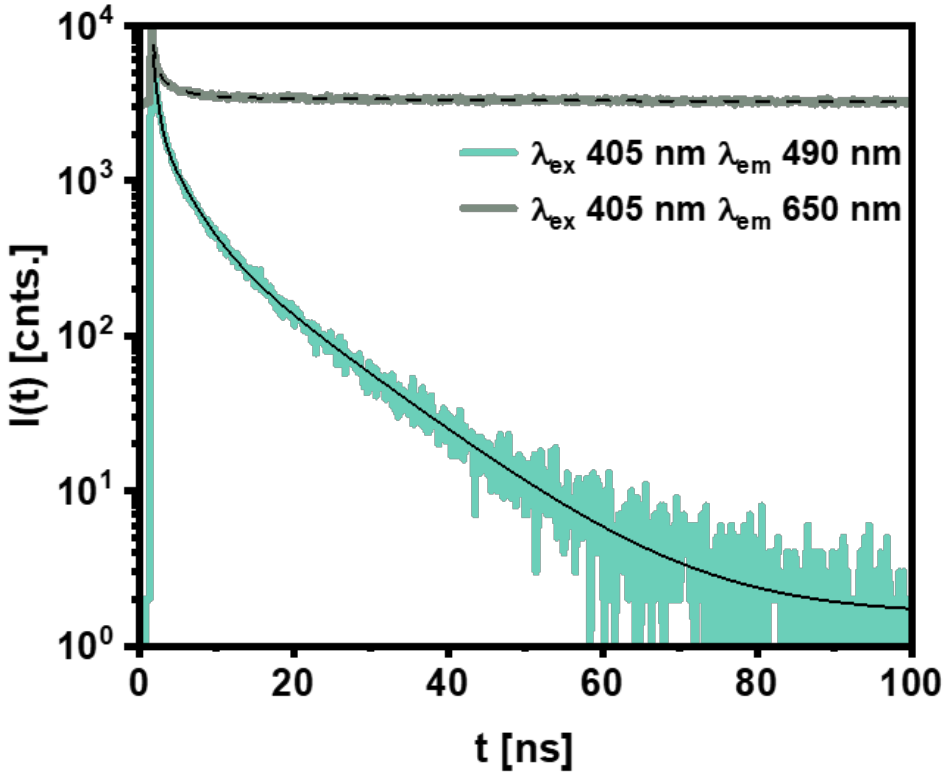

Figure 7.22: Fluorescence LT decay curves of Si-Ag_{29} NCs at ratio $R_{Ag_{29}:Si}$= 2 for the excitation/emission wavelength combinations 405/490 and 405/650. Publication submitted.

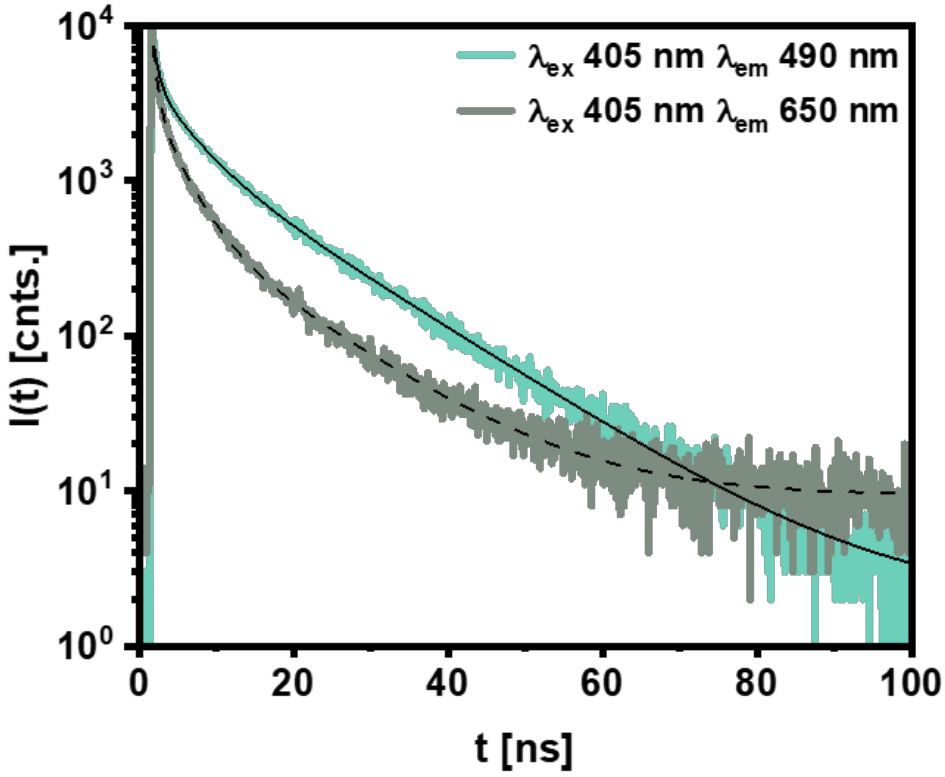

Figure 7.23: Fluorescence LT decay curves of Si NCs at ratio $R_{Ag_{29}:Si}$= 0 for the excitation/emission wavelength combinations 405/490 and 405/650. Publication submitted.

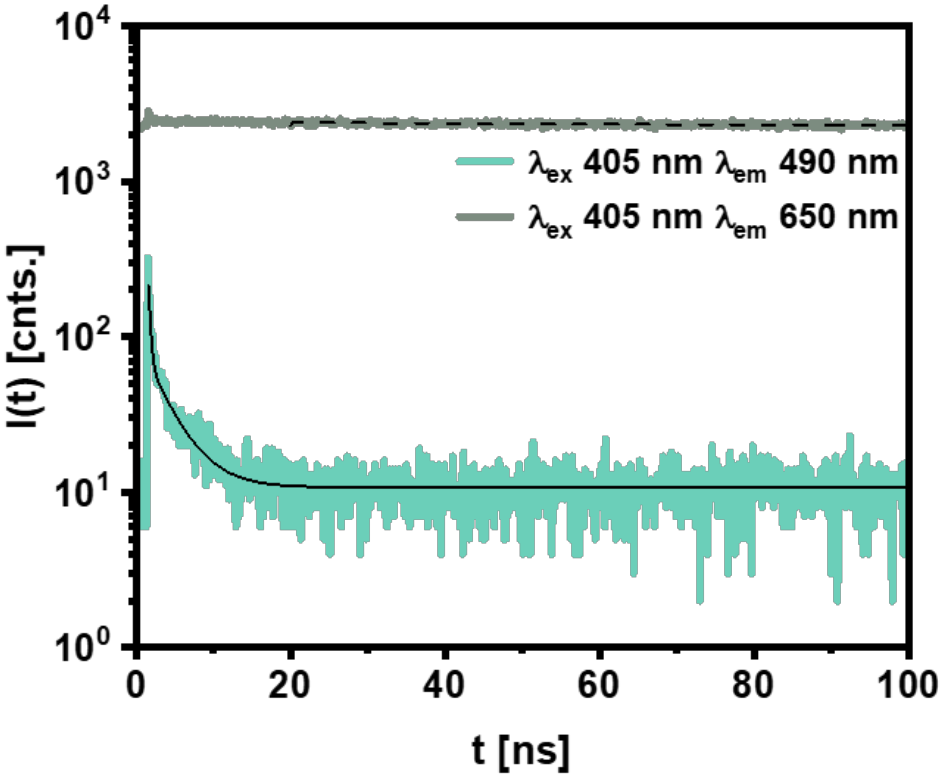

Figure 7.24: Fluorescence LT decay curves of Ag_{29} NCs at ratio $R_{Ag_{29}:Si}$= 1 for the excitation/emission wavelength combinations 405/490 and 405/650. Publication submitted.

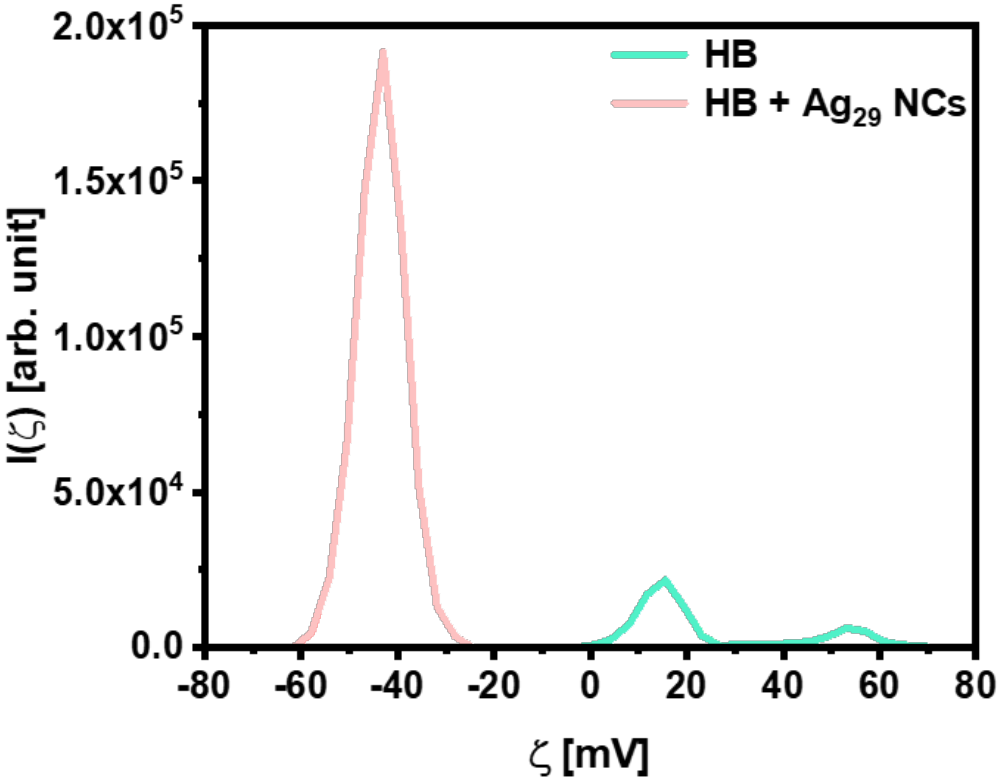

Figure 7.25: Zeta potential ζ of Hoechst Blue (HB), Ag_{29} NCs and their combination. Publication submitted.

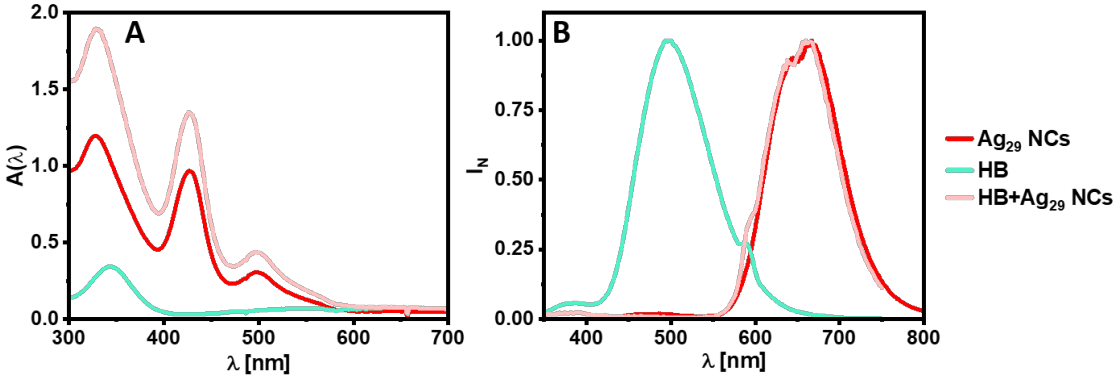

Figure 7.26: Absorbance and PL (normalized) of Hoechst Blue (HB), Ag_{29} NCs and their combination. Publication submitted.

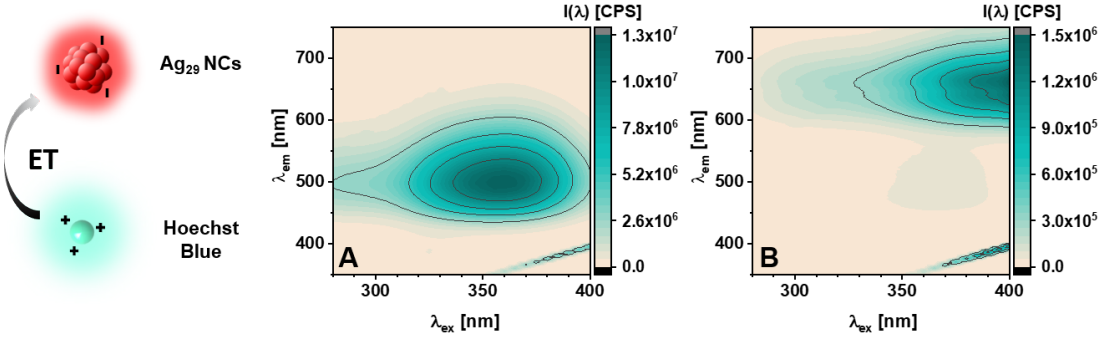

Figure 7.27: 2D-Photoluminescence spectra of HB (A) and HB + Ag_{29} NCs (B) in a charge attracted state depicted by the scheme of the left indicating an energy transfer (ET). Publication submitted.

Table 7.4: LT values τ_{Ave} in ns of Ag_{29} NCs for the excitation/emission wavelength combinations 340/450 and 340/650. Publication submitted.

Sample	HB		Ag_{29} NCs		HB + Ag_{29} NCs	
$\lambda_{exi}/\lambda_{emi}$	τ_{Ave}	±	τ_{Ave}	±	τ_{Ave}	±
340/450	3.388	0.044	2.007	0.047	2.464	0.022
340/660	2.636	0.096	1930	120	1390	140

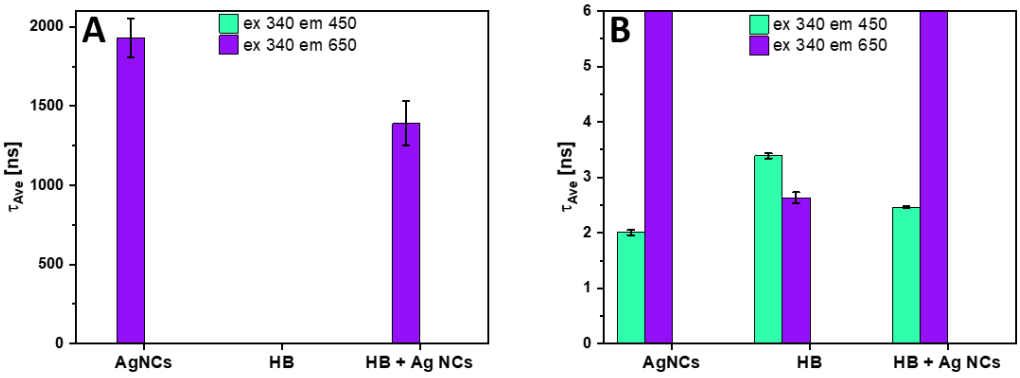

Figure 7.28: LT values of HB, Ag_{29} NCs and HB + Ag_{29} NCs with a HB concentration of 10 mM for the excitation/emission wavelength combinations 340/450, 340/650 in nm. (B) is an enlargement of (A) focusing on small values for the ex/em pair 340/450. Publication submitted.

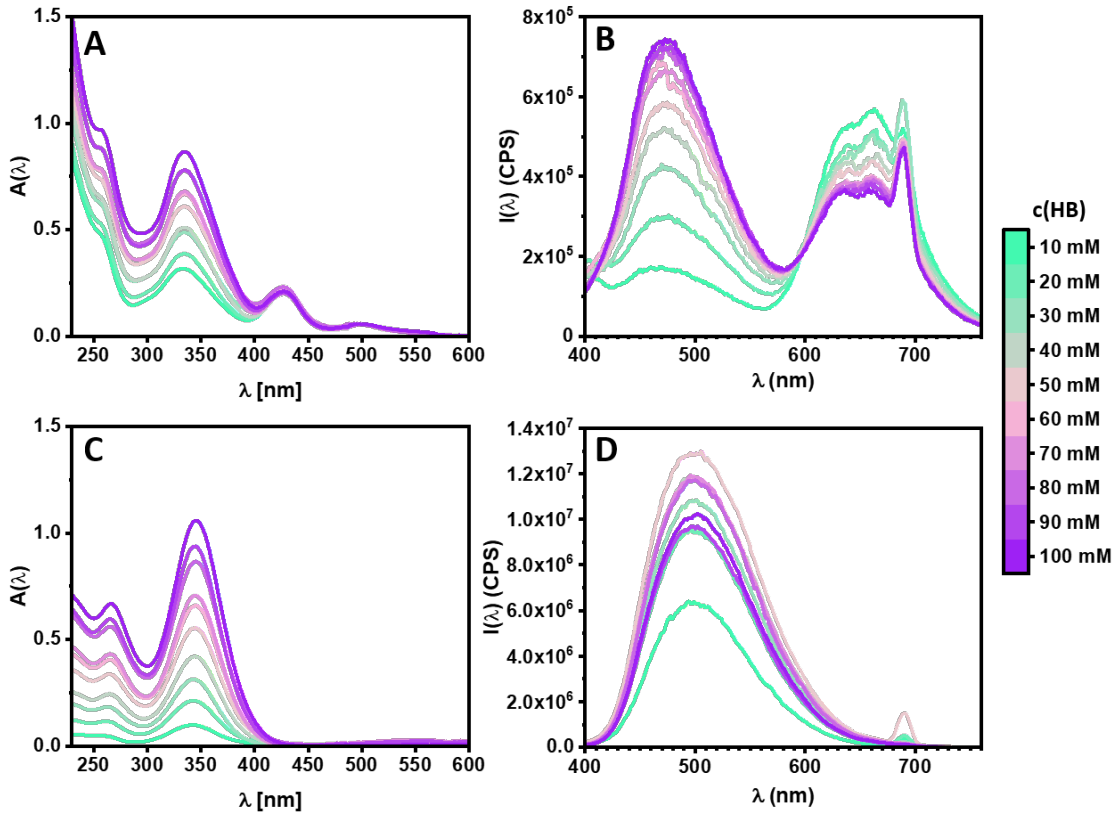

Figure 7.29: Absorbance and photoluminescence of HB + Ag_{29} NCs (A+B) and HB (C+D) with concentrations of HB from 10 mM to 100 mM. Publication submitted.

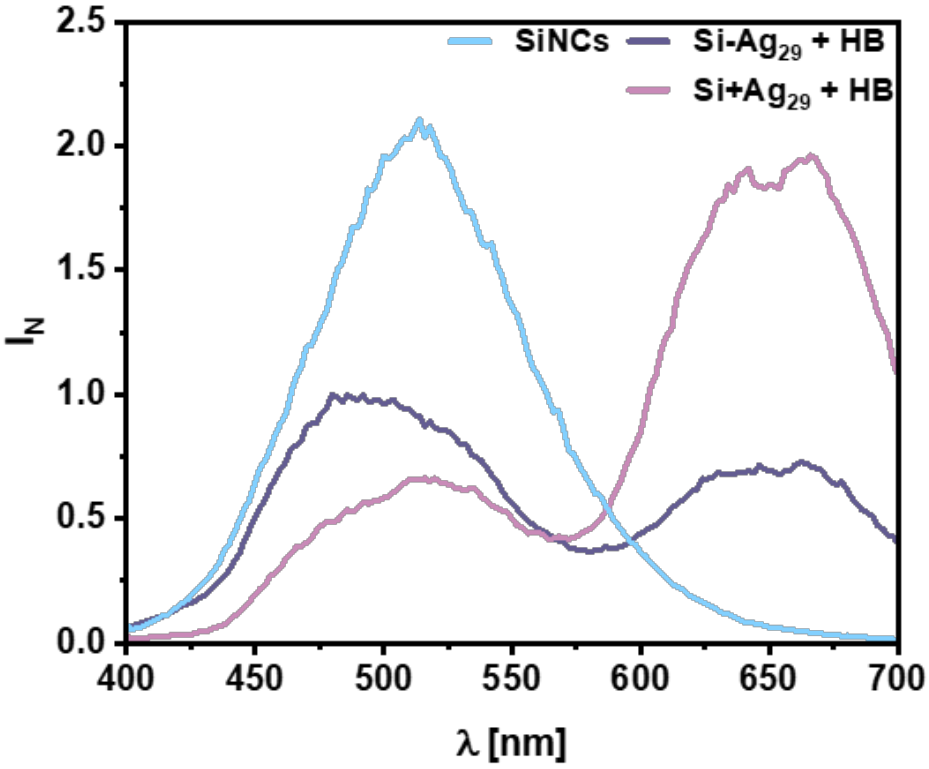

Figure 7.30: Normalized intensity (λ_{ex}=390 nm) of the hybrid system and Si NCs and Ag_{29} NCs in uncoupled state in combination with Hoechst Blue (HB). For comparison, the intensity of Si NCs was added. Publication submitted.

7.2 Ag_{29} NCs on Zinc Oxide Tetrapods

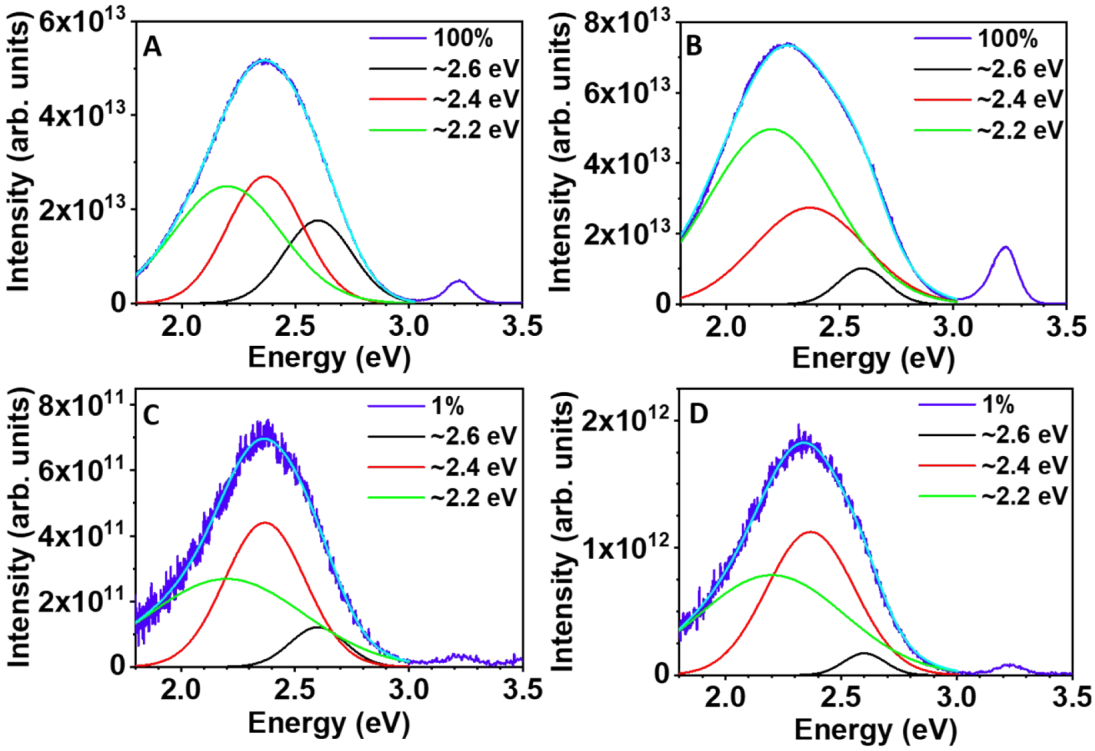

Figure 7.31: PL spectra acquired at RT for ZnO Tp (A) and AgNC@ZnO Tp (B) under 3.81 eV/325 nm laser excitation at 100 % density.(C) and (D): the same as in (A) and (B) for 1 % laser density. The fitting curve (light blue~ resulted from the convolution of 3 Gaussian functions peaked at ~2.6 eV (black), ~2.4 eV (red), and ~2.2 eV (green), for both samples. Prepublished in [4]

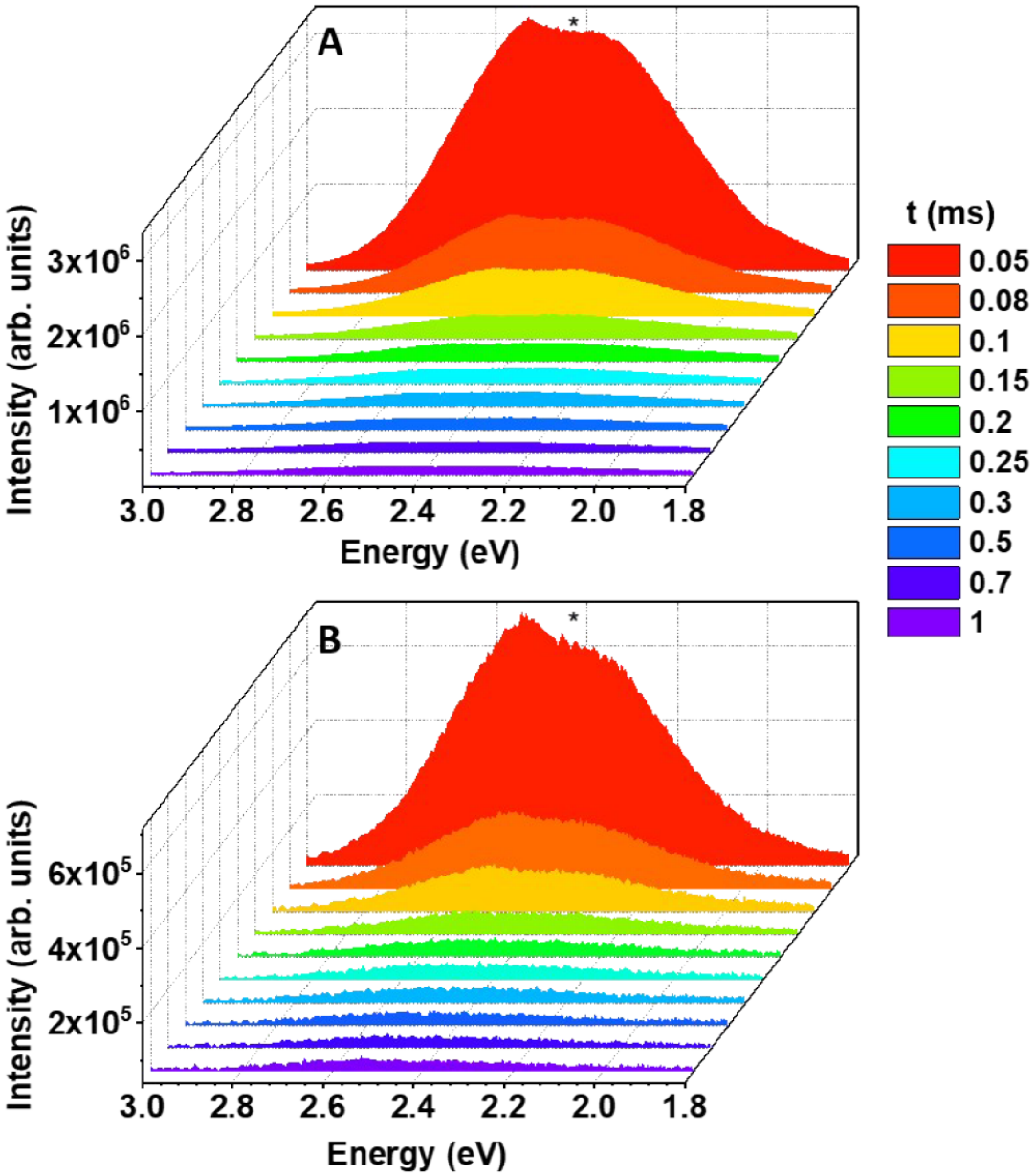

Figure 7.32: RT TRPL spectra with increasing delay times under 3.81 eV/325 nm excitation for ZnO Tp (A) and AgNC@ZnO Tp (B). The asterisk denotes an artefact of the measurement system. Prepublished in [4]

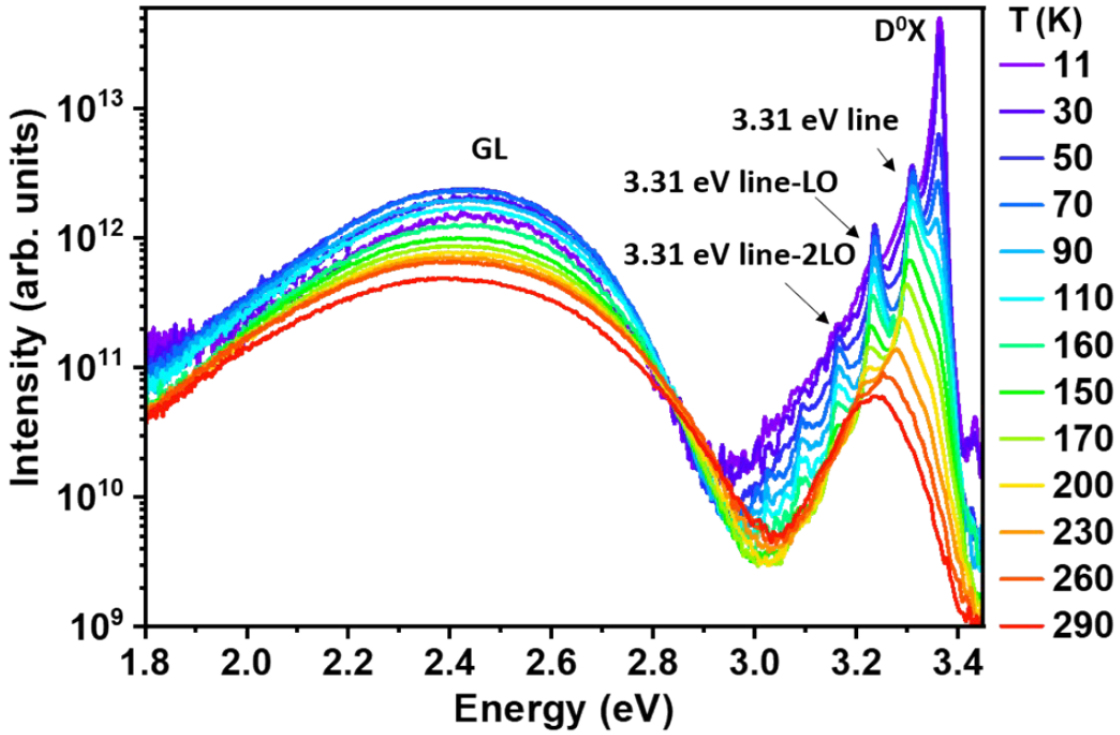

Figure 7.33: UV-Vis temperature-dependent PL study performed on the ZnO Tp sample excited with 3.81 eV/325 nm. Prepublished in [4]

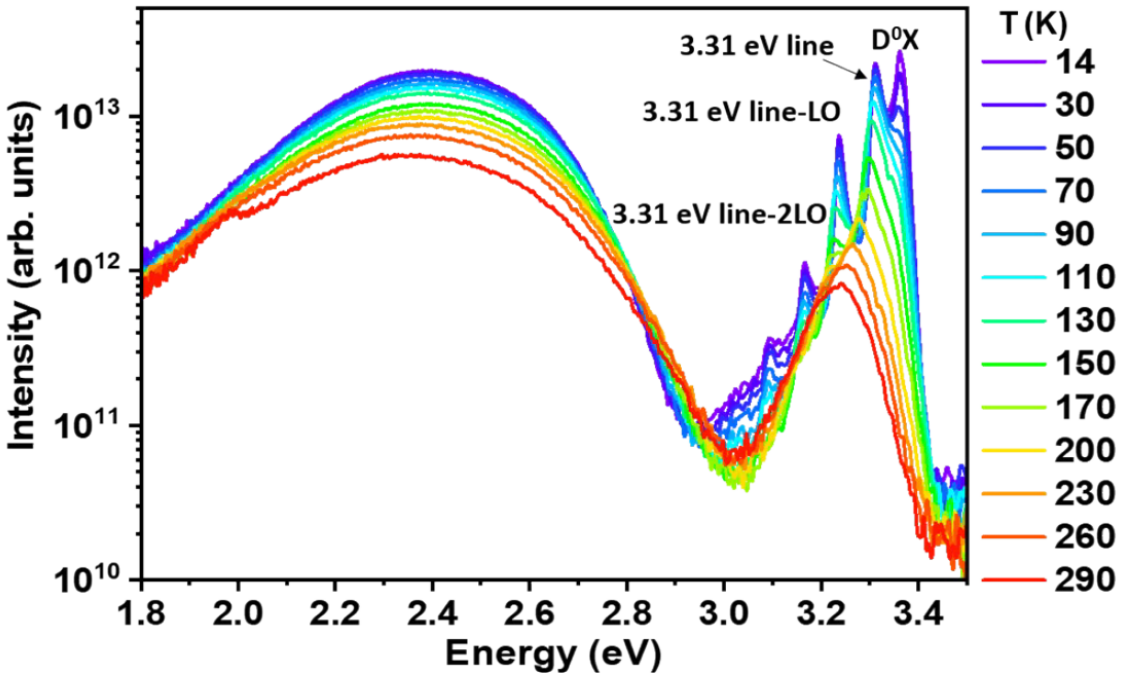

Figure 7.34: UV-Vis temperature-dependent PL study performed on the AgNC@ZnO Tp sample excited with 3.81 eV/325 nm. Prepublished in [4]

Eidesstattliche Versicherung

Hiermit versichere ich an Eides statt, die vorliegende Dissertationsschrift selbst verfasst und keine anderen als die angegebenen Hilfsmittel und Quellen benutzt zu haben.

Ort, Datum	Name